Volume 13, Issue 12 2010

Journal of
POROUS MEDIA

KAMBIZ VAFAI
EDITOR-IN-CHIEF

begell house, inc.
publishers

AIMS AND SCOPE

The *Journal of Porous Media* publishes original full-length research articles (and technical notes) in a wide variety of areas related to porous media studies, such as mathematical modeling, numerical and experimental techniques, industrial and environmental heat and mass transfer, conduction, convection, radiation, particle transport and capillary effects, reactive flows, deformable porous media, biomedical applications, and mechanics of the porous substrate. Emphasis will be given to manuscripts that present novel findings pertinent to these areas. The journal will also consider publication of state-of-the-art reviews. Manuscripts applying known methods to previously solved problems or providing results in the absence of scientific motivation or application will not be accepted. Submitted articles should contribute to the understanding of specific scientific problems or to solution techniques that are useful in applications. Papers that link theory with computational practice to provide insight into the processes are welcome.

JOURNAL OF POROUS MEDIA

JOURNAL OF POROUS MEDIA

Volume 13, Number 12, 2010

CONTENTS

Journal of Porous Media (ISSN: 1091-028X) is published 12 times per year and is owned by Begell House, Inc, 50 Cross Highway, Redding, Connecticut 06896, Phone (203) 938-1300. USA subscription rate for 2010 is $1071.00. Add $10.00 per issue for foreign airmail shipping and handling fees for all orders shipped outside the United States or Canada. All subscriptions are payable in advance. Subscriptions are entered on an annual basis, i.e., January to December. For immediate service and charge card sales, please call (203) 938-1300 Monday through Friday 9 AM — 5 PM EST. Orders can be faxed to (203) 938-1304 or mailed to Subscriptions Department, Begell House, Inc. 50 Cross Highway, Redding, Connecticut 06896.

Indexing and Abstracting: *Journal of Porous Media* is covered by several services provided by ISI®, including Current Contents®/ Engineering, Computing, and Technology, ISI Alerting Services™, and SCI, Science Citation Index®.

Printed December 17, 2010

Journal of Porous Media 13(12), 1039–1058 (2010)

THE INSTABILITY OF A DEVELOPING THERMAL FRONT IN A POROUS MEDIUM. III SUBHARMONIC INSTABILITIES

Asma Selim & D. Andrew S. Rees*

Department of Mechanical Engineering, University of Bath, Claverton Down, Bath BA2 7AY, United Kingdom

*Address all correspondence to D. Andrew S. Rees E-mail: ensdasr@bath.ac.uk

Original Manuscript Submitted: 12/29/2008; Final Draft Received: 6/12/2009

In this paper we study the instability of the developing thermal boundary layer that is induced by suddenly raising the temperature of the lower horizontal boundary of a uniformly cold semi-infinite region of saturated porous medium. The basic state consists of no flow, but the evolving temperature field may be described by a similarity solution involving the complementary error function. In very recent papers, Selim and Rees (2007a) (Part I) have sought to determine when this evolving thermal boundary layer becomes unstable and then Selim and Rees (2007b) (Part II) followed the subsequent evolution of horizontally periodic disturbances well into the nonlinear regime. In this paper we investigate the secondary instability of the nonlinear cells by introducing subharmonic disturbances into the evolving flow. We consider three different types of subharmonic disturbance, namely, the 2:1, 3:2, and 4:3 types. Cellular disturbances are seeded into the evolving basic state, the primary mode having an amplitude that is greater than that of the subharmonic. In general, we find that the subharmonic decays at first, while the primary mode grows, but at a time that is dependent on the relative initial amplitudes, the subharmonic experiences an extremely rapid growth and quickly establishes itself as the dominant flow pattern. A fairly detailed account of the 2:1 case is given, including an indication of how the time of transition between the primary and the subharmonic varies with wave number and initial amplitudes. The other two types of subharmonic disturbance yield a richer variety of behaviors; therefore, we present some typical cases to indicate some of the ways in which the primary mode may be destabilized.

KEY WORDS: *boundary layer, secondary instability, sub-harmonic disturbances*

1. INTRODUCTION

The study of convection generated by a heated horizontal surface underlying a fluid-saturated porous medium has attracted much interest in recent years due to its application to the sudden heating of porous rocks from below such as might occur in volcanically active regions. Recently, convection induced by the sequestration of CO_2 in saturated porous rocks during oil recovery has received attention (Riaz et al., 2006). Indeed, such convection could easily occur during the long-term underground storage of CO_2 gas, as described by Xu et al. (2004), Socolow (2005), and Ennis-King and Paterson (2005), when surface pollutants are present, or indeed when surface evaporation increases the brine density near the surface of a saline lake (Wooding et al. 1997). In all of these cases the presence of thermal or solutal instability will cause an increased mixing, which is generally undesirable. In this paper we shall analyze situations caused by sudden heating as the exemplar of the two different cases, although they are essentially identical when the Boussinesq approximation applies.

When a semi-infinite cold domain has the temperature of its lower impermeable surface raised suddenly, the temperature field evolves according to the standard complementary error function conduction solution, as given by

1091–028X/10/$35.00

NOMENCLATURE

a	related to disturbance amplitude
A	amplitude of disturbance
g	gravity
k	wavenumber of disturbance
K	permeability
L	natural length scale
N	number of modes used
p	pressure
q	heat transfer
q_n	heat transfer for mode n
Ra	Darcy–Rayleigh number
t	time
T	dimensional temperature
u	horizontal velocity
v	vertical velocity
x	horizontal coordinate
y	vertical coordinate

Greek characters

α	thermal diffusivity
β	expansion coefficient
η	similarity variable
θ	nondimensional temperature
μ	dynamic viscosity
ρ	density
τ	scaled time
ψ	streamfunction

Superscripts and subscripts

c	neutral/critical conditions
i	initiation time
s	subharmonic transition
w	wall
∞	ambient

Carslaw and Jaeger (1986). This situation is potentially unstable since relatively heavy fluid lies over relatively light fluid. A Rayleigh number may be defined using a length scale that is based upon the thickness of the evolving hot region. This value increases as time progresses, and therefore a critical time for the onset of convection should be expected. Rees et al. (2008) discuss the many ways in which this criterion for the onset of convection may be obtained. Various methods have been proposed such as quasistatic theory (i.e., a frozen-time theory) and a local Rayleigh number analysis, which are approximate, but which give a rough idea of the time of onset and the expected critical wave number. Energy analyses and amplitude theory (in the sense of solving the time-dependent disturbance equations) yield results that should be expected to tally with experimental results. However, these comparisons and the discussions surrounding them are lengthy; therefore, the reader is referred to Rees et al. (2008), and the references cited therein for further information.

The present paper is an extension of work by Selim and Rees (2007a, 2007b), hereafter referred to as Parts I and II. The former of these papers did not rely upon an approximate theory to give a critical time for the onset of convection. Instead, the full linearized disturbance equations, which are parabolic in time, were solved numerically in order to assess when disturbance ceases to decay and begins to grow, thereby determining a critical time. After a large number of different disturbance wavelengths was considered, a neutral curve was constructed that relates the critical time and the disturbance wave number. It was found that the critical time also depends on the time at which the disturbance is introduced (unless this time is well before the smallest achievable onset time). More surprisingly, it also depends on the manner in which one attempts to define instability (i.e., on how one defines the strength of the evolving disturbance). The resulting neutral curves were compared with the results of a quasistatic or frozen-time approximate theory. The earliest onset time was the one that employed a thermal energy functional as the measure of the disturbance amplitude. In general, it was found that convection occurs much earlier than is predicted by the approximate theories. Moreover, and to one's initial surprise, it was found that growing cells always eventually restabilize and decay.

The linear theory was extended into the nonlinear regime in Part II in order to determine how finite-amplitude disturbances evolve. A mixed finite-difference and Fou-

rier series method was used to follow the evolution of nonlinear cells. Although detailed results were given on the effects of varying the initiation time and amplitude of the disturbance, the most important feature that was found is that even nonlinear cells eventually restabilize and decay. Indeed, nonlinear cells were found to restabilize earlier than their small-amplitude counterparts. This property of restabilization is seemingly at odds with the fact that the Darcy–Rayleigh number based on the thickness of the evolving basic state continues to grow, and therefore the whole configuration becomes increasingly thermoconvectively unstable with time. The aim of the present paper is to begin the process of resolving this apparent conflict.

In this paper, then, we are interested in the role played by secondary instabilities of the evolving nonlinear cells. That secondary instabilities should form the correct mode of disturbance may be predicted using the fact that the basic thermal boundary layer thickness grows in time, and larger wavelengths of cells (i.e., smaller wave numbers) are required to ensure that convection cells remain with roughly an $O(1)$ aspect ratio. The shape of the neutral stability curve is also such that the time interval over which growth can occur is much longer for smaller wave numbers. Therefore, it is worth investigating whether secondary disturbances with relatively small wave numbers can destabilize evolving nonlinear cells, thereby allowing strong convection to be maintained at later times.

We concentrate on the 2:1, 3:2, and 4:3 subharmonic cases where the respective wave numbers of the primary and subharmonic modes are in the ratio, m:n.

2. GOVERNING EQUATIONS AND BASIC SOLUTION

We are considering the instability of a basic state that is composed of a quiescent semi-infinite region of saturated porous medium at the uniform cold temperature T_∞, in which the lower horizontal boundary has its temperature raised suddenly to a new uniform level T_w, where $T_w > T_\infty$. The porous medium is considered to be homogeneous and isotropic, and the solid and fluid phases are in local thermal equilibrium. We assume that the flow is governed by Darcy's law modified by the presence of buoyancy and subject to the Boussinesq approximation. Thus, the governing equations for the fluid motion and temperature field for buoyancy-driven convection are expressed in the following nondimensional form:

$$\frac{\partial u}{\partial x} + \frac{\partial v}{\partial y} = 0 \tag{1a}$$

$$u = -\frac{\partial p}{\partial x} \tag{1b}$$

$$v = -\frac{\partial p}{\partial y} + \theta \tag{1c}$$

$$\frac{\partial \theta}{\partial t} + u\frac{\partial \theta}{\partial x} + v\frac{\partial \theta}{\partial y} = \frac{\partial^2 \theta}{\partial x^2} + \frac{\partial^2 \theta}{\partial y^2} \tag{1d}$$

The appropriate boundary conditions are as follows:

$$y=0: \ v=0, \ \theta=1 \quad \text{and} \quad y\to\infty: \ v,\theta\to 0 \tag{1e}$$

while $\theta = 0$ everywhere within the porous medium when $t = 0$. In Eqs. (1a) and (1b) x and y are the horizontal and vertical coordinates, respectively, while u and v are the corresponding seepage velocities. In addition, p is the pressure while θ is the temperature.

It is essential to mention that there is no physical length scale in this semi-infinite domain, but that it is possible to define a length scale in terms of the properties of the fluid and porous matrix:

$$L = \frac{\mu\alpha}{\rho g \beta K (T_w - T_\infty)} \tag{2}$$

where ρ, g, β, K, T_w, T_∞, μ and α are the reference density, gravity, coefficient of cubical expansion, permeability, wall temperature, ambient temperature, dynamic viscosity, and effective thermal diffusivity, respectively. This definition of the length scale means that the usual Darcy–Rayleigh number takes a unit value

$$\mathrm{Ra} = \rho g \beta K L (T_w - T_\infty)/\mu\alpha = 1. \tag{3}$$

After eliminating pressure p between Eqs. (1b) and (1c) and on introducing stream function ψ, which is defined according to

$$u = \frac{\partial \psi}{\partial y} \quad \text{and} \quad v = -\frac{\partial \psi}{\partial x} \tag{4}$$

then the continuity equation is satisfied. Equations (1b)–(1d) now reduce to the pair

$$\frac{\partial^2 \psi}{\partial x^2} + \frac{\partial^2 \psi}{\partial y^2} = \frac{\partial \theta}{\partial x} \tag{5a}$$

$$\frac{\partial \theta}{\partial t} + \frac{\partial \psi}{\partial x}\frac{\partial \theta}{\partial y} - \frac{\partial \psi}{\partial y}\frac{\partial \theta}{\partial x} = \frac{\partial^2 \theta}{\partial x^2} + \frac{\partial^2 \theta}{\partial y^2} \tag{5b}$$

which are to be solved subject to the boundary conditions

$$y=0: \ \psi=0, \ \theta=1 \quad \text{and} \quad y\to\infty: \ \psi,\theta\to 0 \tag{5c}$$

and the initial condition that

$$\psi = \theta = 0 \quad \text{at} \quad t = 0 \tag{5d}$$

Therefore, at $t = 0$, the temperature of the lower boundary of the semi-infinite region of porous medium is raised suddenly from 0 to 1 where it remains for all $t > 0$.

The basic conduction profile is independent of x with no flow, and the thermal energy equation reduces to

$$\frac{\partial \theta}{\partial t} = \frac{\partial^2 \theta}{\partial y^2} \tag{6}$$

Equation (6) admits the well-known solution,

$$\theta = \operatorname{erfc} \eta = \frac{2}{\sqrt{\pi}} \int_{\eta}^{\infty} e^{-\xi^2}\, d\xi \tag{7}$$

where the similarity variable is given by

$$\eta = \frac{y}{2\sqrt{t}} \tag{8}$$

In this paper we choose to consider disturbances to the basic profile given in Eq. (7) by transforming the governing equations into the new coordinate system (η, τ), where η is given above and $\tau = \sqrt{t}$; this transformation of t to τ avoids the explicit appearance of fractional powers of t within the governing equations. Equations (5a) and (5b) now become

$$4\tau^2 \frac{\partial^2 \psi}{\partial x^2} + \frac{\partial^2 \psi}{\partial \eta^2} = 4\tau^2 \frac{\partial \theta}{\partial x} \tag{9a}$$

$$\begin{aligned} 2\tau \frac{\partial \theta}{\partial \tau} + 2\tau \left(\frac{\partial \psi}{\partial x} \frac{\partial \theta}{\partial \eta} - \frac{\partial \psi}{\partial \eta} \frac{\partial \theta}{\partial x} \right) = 4\tau^2 \frac{\partial^2 \theta}{\partial x^2} \\ + \frac{\partial^2 \theta}{\partial \eta^2} + 2\eta \frac{\partial \theta}{\partial \eta} \end{aligned} \tag{9b}$$

Given that the coefficient of θ on the right-hand side of Eq. (9a) increases with time, it is clear that the strength of the buoyancy forces also increases. Physically, the thickness of the region over which the temperature varies from 1 on the lower boundary to a nominal value, such as 0.01, also increases with time, and therefore a local Rayleigh number based on the thermal boundary layer thickness is seen to increase.

3. NUMERICAL METHOD

In Part II, we undertook a numerical investigation of the nonlinear evolution of spanwise periodic disturbances by taking a truncated spanwise Fourier expansion of the form

$$\psi(x, \eta, \tau) = \sum_{n=1}^{N} \psi_n(\eta, \tau) \sin nkx \tag{10a}$$

$$\begin{aligned} \theta(x, \eta, \tau) = \operatorname{erfc} \eta + \frac{1}{2}\theta_0(\eta, \tau) \\ + \sum_{n=1}^{N} \theta_n(\eta, \tau) \cos nkx \end{aligned} \tag{10b}$$

where k is the wave number and N is the truncation level. In Part I we retained only the ψ_1 and θ_1 terms since they were assumed to be infinitesimally small in magnitude. Therefore, nonlinearities were neglected in order to form a linearized stability theory. In Part II ψ_1 and θ_1 formed the primary mode and this mode interacted with itself to induce components with wave numbers $2k$, $3k$, and so on. The term $\frac{1}{2}\theta_0$ yields the mean change to the basic state due to the presence of convective cells. In this paper we shall refer to the pair (ψ_n, θ_n) as mode n.

The substitution of the expansions (10) into Eqs. (9a) and (9b) is very lengthy to present and has been omitted for the sake of brevity. The resulting system is comprised of $2N + 1$ second-order partial differential equations in η and τ. In the numerical simulations of Part II, the truncation level was chosen to be $N = 5$, which was sufficient since the magnitude of θ_5 was always very small compared with unity. The full system was then solved by a standard Keller-box method using the numerical differentiation methodology described by Lewis et al. (1997) to obtain the Newton–Raphson iteration matrix.

In the present paper we are interested in how subharmonic disturbances destabilize the solutions obtained in Part II. For the 2:1 subharmonic case, mode 2 (which has wave number $2k$) is termed the primary mode, while mode 1 is the potentially destabilizing subharmonic. For the 3:2 case, mode 3 forms the primary mode while mode 2 is the subharmonic disturbance. This naming scheme follows in the obvious way for the 4:3 subharmonic case.

In general, then, thermal disturbances are introduced at the initiation time $\tau = \tau_i$ for a given wave number k and the disturbance profiles take the form

$$\theta_n = A_n \eta e^{-3\eta} \tag{11}$$

where A_n is the amplitude of the mode n disturbance. Part II showed that the mode shape is largely irrelevant, as the disturbances quickly evolve to a common shape that is essentially independent of the initial disturbance shape and time of introduction. For the nonlinear study of Part II we set $A_1 = A$ and $A_n = 0$ otherwise. Here, for the 2:1 case, both A_1 and A_2 will be nonzero with $A_2 > A_1$, since mode 2 is to be destabilised by mode 1. All other A_n values will be set to zero. Likewise, for the 3:2 case

we will have $A_3 > A_2$ with all other values of A_n set to zero.

Given that $N = 5$ was the smallest truncation level that yielded reliable results in Part II, we need to take $N = 10$ for the 2:1 case, $N = 15$ for the 3:2 case, and $N = 20$ for the 4:3 case.

A rectangular domain in η and τ was used where η ranges from 0 to 10 with the uniform step of 0.05, this maximum value of η being sufficient to contain the evolving disturbance, while a step length of 0.1 was used in the τ direction.

For reference, Fig. 1 depicts the neutral stability characteristics obtained in Part I, and forms the context into which to set the present computations. Two neutral curves are shown, namely, that obtained using a quasistatic theory (continuous curve) and that obtained by using an energy integral to determine the magnitude of the evolving disturbance (symbols). Disturbances decay when the wave number and time correspond to locations below the curve, to the right of the right-hand branch and to the left of the left-hand branch, otherwise they grow. For the quasistatic approximate theory disturbances for which $k > 0.101053$ (see Part I) are always destined to decay, i.e., they are stable. All other disturbances decay until they first cross the curve vertically, after which point they grow, but then they restabilize and decay upon crossing the upper branch of the curve. The equivalent maximum wave number for the exact theory is $k = 0.1124$.

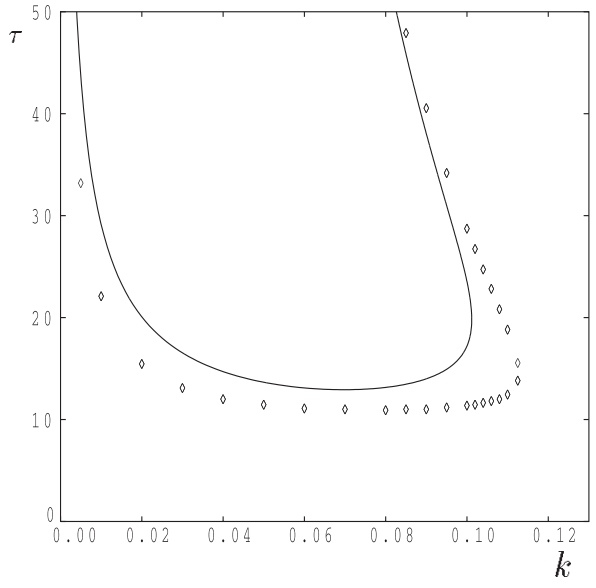

FIG. 1: Neutral stability curve: τ against k.

Of more importance is the earliest time after which disturbances grow; for the quasistatic theory this critical time and its associated wave number are given by

$$\tau_c = 12.944356 \quad \text{and} \quad k_c = 0.069623 \tag{12a}$$

while the corresponding data for the exact theory are

$$\tau_c = 8.9018 \quad \text{and} \quad k_c = 0.07807 \tag{12b}$$

Thus, disturbances always decay when $\tau < 8.9018$.

4. NUMERICAL RESULTS

In this section we present a detailed account of how the presence of subharmonic disturbances affects the evolution of the primary mode. In all cases we shall take $\tau_i = 8$ as the initiation time for both the primary and the subharmonic. This leaves us with a choice of the wave number, the type of subharmonic (i.e., 2:1, 3:2, or 4:3), and the amplitudes of the initiating disturbances. The strength of the various horizontal Fourier modes may be gauged in terms of the surface rate of heat transfer of each:

$$q_n(\tau) = \left.\frac{\partial \theta_n}{\partial \eta}\right|_{\eta=0} \tag{13}$$

The overall evolution of the flow is also assisted by the heat transfer footprint of disturbance, $q(x, \tau)$, which is defined as follows:

$$q(x, \tau) = \frac{1}{2} q_0 + \sum_{n=1}^{N} q_n(\tau) \cos nkx \tag{14}$$

The expression for q is useful, in particular, for showing how many convection cells are present at any point in time, and for showing when the peak rates of heat transfer occur.

4.1 The 2:1 Subharmonic Case

In this case we specify a relatively large value of amplitude A_2 of mode 2 (the primary mode) and attempt to destabilize it with a small disturbance in the form of mode 1. Figure 2 represents a typical set of cases where the wave number of the subharmonic is $k = 0.035$, so that the primary mode has a wave number of 0.07. We have chosen $A_2 = 10^{-1}$ as the initial amplitude of the primary mode. A selection of values of A_1 have been used to show the influence of the amplitude of the subharmonic on how quickly the primary mode is destabilized. Also included is the basic case with $A_1 = 0$ in order to show how the

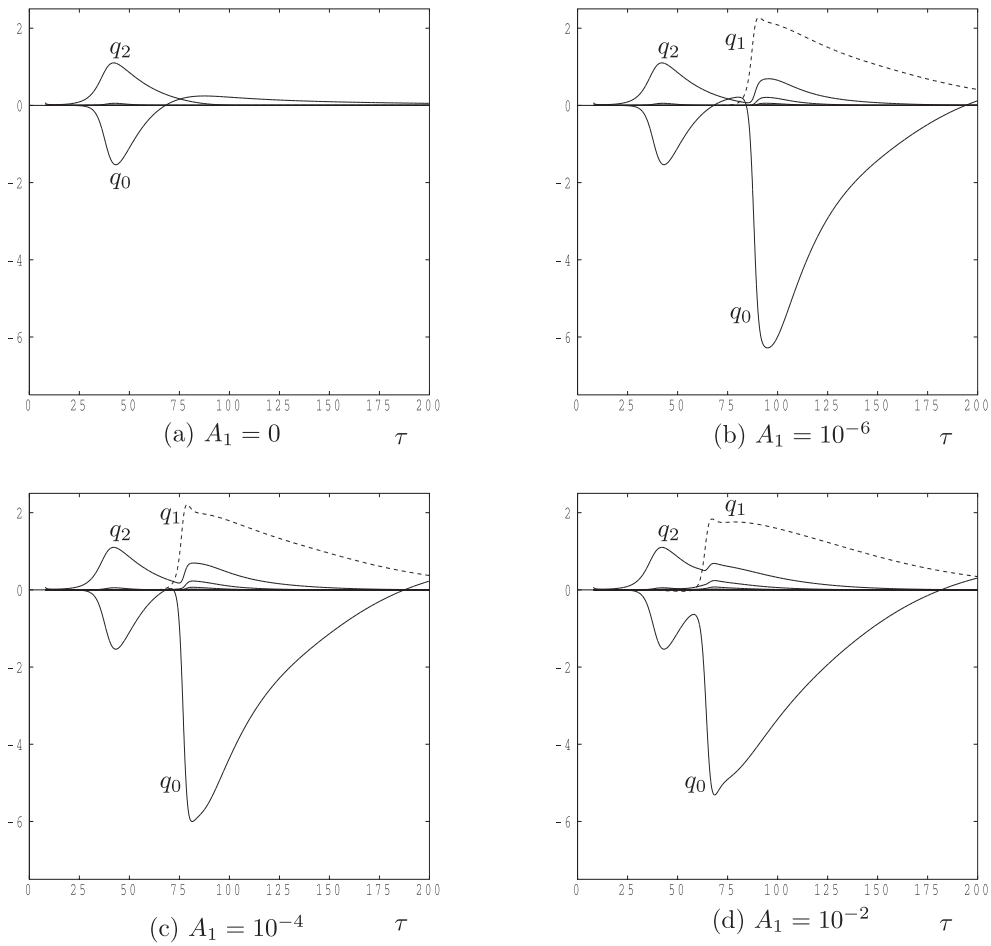

FIG. 2: Variation with τ of the surface rates of heat transfer, q_n, corresponding to the modes, $n = 0, 1, 2 \cdots$. These simulations correspond to $\tau_i = 8$, $k = 0.035$, and $A_2 = 10^{-1}$ and a selection of values of A_1.

primary mode varies without subharmonic disturbances being present. Solutions are presented in terms of the surface rate of heat transfer of the different Fourier modes.

Concentrating first on the unrestricted evolution of the primary mode, for which $A_1 = 0$, both Fig. 2 and the data it represents show that the primary mode begins to grows at a time that is roughly consistent with the $k = 0.07$ mode in Fig. 1. It is worthy of note that the neutral curve shown in Fig. 1 corresponds to a thermal energy criterion which gives an earlier onset time a curve which is based on the surface rate of heat of heat transfer; see Part I for a detailed discussion of this point. The primary mode then decays at $\tau \equiv 45$, which is well before the stabilization time for linear theory, which is roughly $\tau \equiv 75$. The strength of the nonlinear convection may be gauged by the magnitude of $\frac{1}{2}q_0$, which, at its peak, almost doubles the rate of heat transfer due to the basic temperature profile. Therefore, strongly nonlinear effects have altered the x-independent background state from that of the solution given in Eq. (7), and it is this that causes the premature restabilization when compared with linearized theory.

Concentrating now on how subharmonic disturbances alter the evolution of the primary mode, Fig. 2 also presents the effect of three different subharmonic amplitudes, $A_1 = 10^{-6}$, 10^{-4}, and 10^{-2}, while keeping all other parameters fixed. We note that the subharmonic, for which $k = 0.035$, has a later onset time and a much later restabilization time than the primary mode, which has a wave number of 0.070, at least for linearized theory (see Fig. 1). In all three cases the subharmonic appears very suddenly while the primary mode is undergoing a slow decline. In fact, when A_1 is much smaller than 10^{-2}, the primary

mode has already decayed substantially before the subharmonic begins to grow, and the late appearance of the subharmonic is due entirely to how small its amplitude has become since $\tau = \tau_i$ and the need to be able to grow again to an $O(1)$ magnitude. However, when A_1 is as large as 10^{-2}, the subharmonic grows well before the primary modes decay greatly. Figure 2 also shows that destabilization of the primary mode occurs increasingly early as A_1 increases, but that the peak magnitude of q_0 decreases as A_1 increases. In Figs. 1 and 2 the behavior of the higher modes is most easily illustrated by noting the heights of the various maxima situated at $\tau \simeq 90$ in Fig. 2(b); here, the highest maximum corresponds to mode 1, the next to mode 2, and so on.

The behavior of the mean rate of heat transfer q_0 also deserves some discussion. In Part II we saw that the maximum magnitude of q_0 is attained at roughly the same time as the maximum value of the heat transfer since the primary mode is attained. The large value of q_0 is a consequence of the fact that the mean temperature field has been altered substantially by the strongly nonlinear convection pattern. Thereafter, the magnitude of q_0 decreases rapidly, and q_0 itself changes sign. This feature also occurs here. However, when the primary mode is destabilized, the magnitude of q_0 rises rapidly once more as the subharmonic mode is established, and then it falls away again as the subharmonic mode eventually begins to decay.

Figure 3 shows an alternative view of the solutions shown in Fig. 2 by depicting the isolines of the surface rate of heat transfer of the disturbance as a function of x and τ; i.e., the heat transfer footprint given by Eq. (14). In each subfigure, contours are drawn using 20 equally spaced intervals centered at zero. Therefore, the levels vary from subfigure to subfigure. Four whole wavelengths of the primary mode are depicted, but the subharmonic instability reduces this to two wavelengths. The evolution of the primary mode, for which $A_1 = 0$, shows a clear period of growth followed by decay. The strength of the nonlinearity is indicated by the lack of symmetry between neighboring thermal cells. The four strongest cells correspond to situations where the fluid is moving toward the surface, bringing cold fluid downward and increasing the rate of heat transfer. The weaker cells, which interleave the stronger ones, correspond to outflow, and these rise up from the surface (see Part II).

When subharmonic disturbances are present, the initial evolution of the primary mode is unaffected until well after they have achieved their maximum rate of heat transfer. In fact, the bottom half of each of the subfigures with $A_1 \neq 0$ are almost identical to the subfigure with $A_1 = 0$. However, once the subharmonic appears, the primary cells are destroyed rapidly, as seen by the very close spacing of the isotherms. In fact, the subharmonic is so strong that the alternate cells have lifted from the surface, as will be seen in Fig. 4(a). Thus, the contours in the very top parts of the nonzero A_1 subfigures correspond to two periods. Figure 3 also shows very clearly how different values of A_1 affect the time at which the subharmonic appears.

Figures 4(a) and 4(b) show the detailed isotherms and streamlines of the evolving disturbance, respectively, at various values of τ for the $A_1 = 10^{-2}$ case, which is covered in Figs. 2 and 3. In Figs. 2 and 3, two whole horizontal periods of the primary mode are depicted, and this corresponds to one period of the subharmonic. In Fig. 4(a),

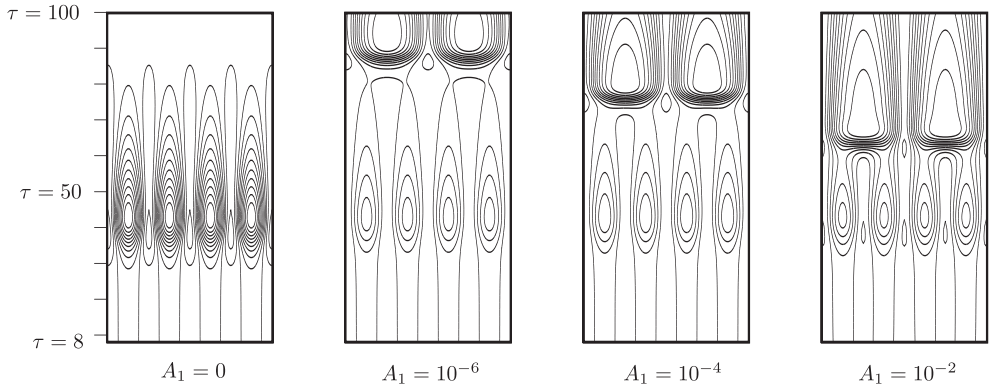

FIG. 3: Isolines of the surface rate of heat transfer, $q(x, \tau)$, for the wave number, $k = 0.035$, using $\tau_i = 8$, $A_2 = 10^{-1}$, and a selection of values of A_1. The horizontal coordinate varies between $x = 0$ and $x = 8\pi/k$; i.e., four horizontal periods, and the vertical axis varies between $\tau = \tau_i = 8$ and $\tau = 100$.

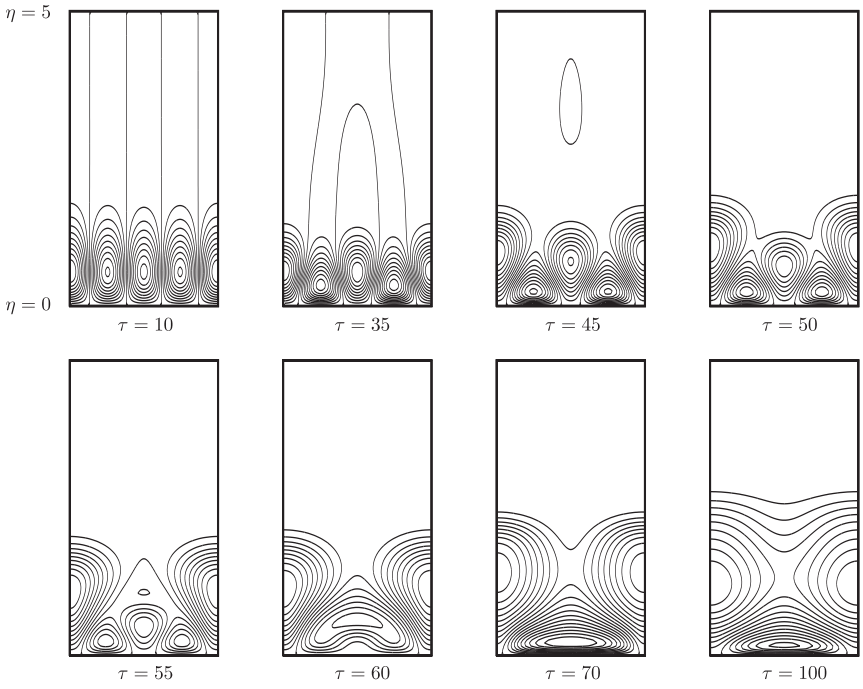

(a)

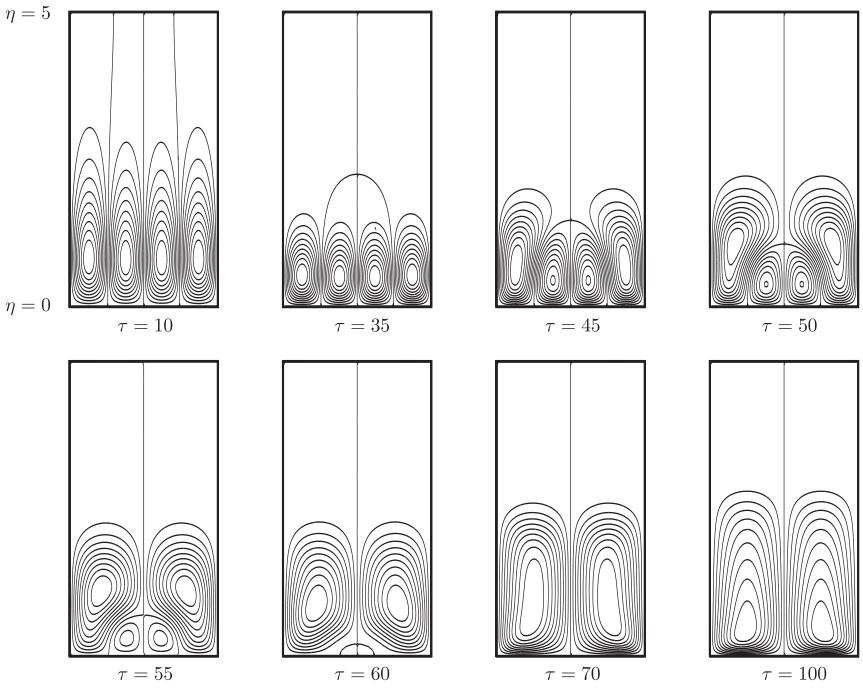

(b)

FIG. 4: (a) Contours of the perturbation temperature profiles and **(b)** streamlines of the flow at chosen times for the evolution of the subharmonic instability given by $\tau_i = 8$, $k = 0.035$, $A_1 = 10^{-2}$, and $A_2 = 10^{-1}$. The horizontal coordinate varies between $x = 0$ and $x = 4\pi/k$; i.e., two horizontal periods.

the transition from the fully developed primary mode to the fully developed subharmonic is shown. At first, the two thermal cells on either side of the central cell shrink compared with the others due to inflow, and it is these cells which are responsible for the higher rates of heat transfer seen in Fig. 3. When $\tau = 50$, the outer half-cells have grown to such an extent that all three cells in the middle are smaller. Although the central cell was larger than its two nearest neighbors when $\tau = 35$, it shrinks and does so to such an extent that these neighbors drive it to extinction at the surface, whereupon they grow and merge. At $t = 70$ the process is complete and the rate of heat transfer at the heated surface is now very large indeed, as is seen by the closeness of the isotherms there, and by the magnitude of q_0 in Fig. 2. When $\tau = 100$ the isotherm spacing has increased, thereby reducing the surface rate of heat transfer once more.

Figure 4(b) depicts the corresponding behavior of the streamlines and this shows an alternative view of the subharmonic instability. Between $\tau = 10$ and $\tau = 35$ the momentum boundary layer decreases in thickness. This happens because each ψ_n function, as given in Eq. (9a), satisfies an equation of the form

$$\psi_n'' - 4n^2k^2\tau^2\psi_n = -4nk^2\tau^2\theta_n \qquad (15)$$

and therefore, for a given k, the e-folding distance decreases as τ increases. After $\tau = 35$ the inner two cells gradually weaken forming a pair of recirculating regions which gradually diminish in size and strength. Just after $\tau = 60$ they disappear, leaving a relatively thick region where the subharmonic forms the dominant solution. The e-folding distance of the subharmonic is double that of the primary mode, which is why the disturbance has roughly doubled in thickness. At later times the thickness of the subharmonic will begin to decrease once more.

Figure 5 shows a summary of the situation depicted in Figs. 2–4 and of a much larger set of computations. Figure 5 displays what we shall call the transition time as a function of the initial amplitudes of the primary mode and the subharmonic. The transition time τ_s is defined as being that time at which the values of q_1 and q_2 have exactly the same magnitude. The value a on the abscissa corresponds to an initial subharmonic amplitude of $A_1 = 10^{-a}$ (i.e., $a = -\log_{10} A_1$), while the different symbols correspond to different initial primary cell amplitudes; these are indicated in the caption to Fig. 5.

The interpretation of Fig. 5 is as follows. Below the horizontal line all modes of the chosen wave number decay, but the primary mode begins to grow upon crossing the line, as the line represents the onset criterion. Given the information represented by Fig. 2, the primary mode then reaches a maximum and subsequently decays. When the symbol representing the chosen value of A_2 is encountered, it is at this point in time that the surface heat transfer due to the growing subharmonic q_1 is equal to that of the decaying primary mode, as given by q_2.

Focusing first on the case $k = 0.04$, for which the primary mode has a wave number of 0.08, it is clear that for a chosen value of A_2, the transition time increases with increasing value of a, i.e., for decreasing amplitudes of the subharmonic disturbance. This happens because it takes a longer time for the subharmonic to grow until it reaches an $O(1)$ magnitude. When we consider the variation in the transition time as a function of A_2, it is also clear that the transition time increases as A_2 decreases. This behavior may be understood easily, for a reduction in the strength of the primary mode requires a less strong subharmonic to destabilize it.

When $k = 0.035$ we obtain a similar pattern of transition times as for $k = 0.04$, but they occur later because the primary mode has the wave number 0.07, which is very close to the critical wave number given in Eq. (12), and therefore it grows more strongly than that given in Fig. 5(a). This trend continues as k is reduced, and becomes more marked because the linearized onset time for the subharmonic now begins to grow quite rapidly compared with that for the primary mode. Thus, the 2:1 subharmonic route to destabilization becomes less effective for these wave numbers.

A corollary of the above conclusion is that if the primary mode is sufficiently weak, then the subharmonic may even be too strong for the "primary" mode to become established. In fact, the absence of data below $\tau \simeq 32$ in Fig. 5(a) is because the subharmonic grows in preference to the primary mode and establishes itself first. This also explains the presence of some "anomolous" transition points in Fig. 5(d) for smaller values of a; in this case, the data points represent a reverse transition where the mode with the smaller wave number is destabilized by the mode with the higher wave number.

When the wave number of the primary mode is greater than 0.08 (and the subharmonic has a wave number greater than $k = 0.04$), the opposite effect is true. In this case, the transition times are earlier because the onset times for the primary mode and its subharmonic are much closer, as may be seen in Fig. 1, and there is now only a small interval of time over which the primary mode can grow. Therefore, this primary mode is easier to destabilize using subharmonic disturbances.

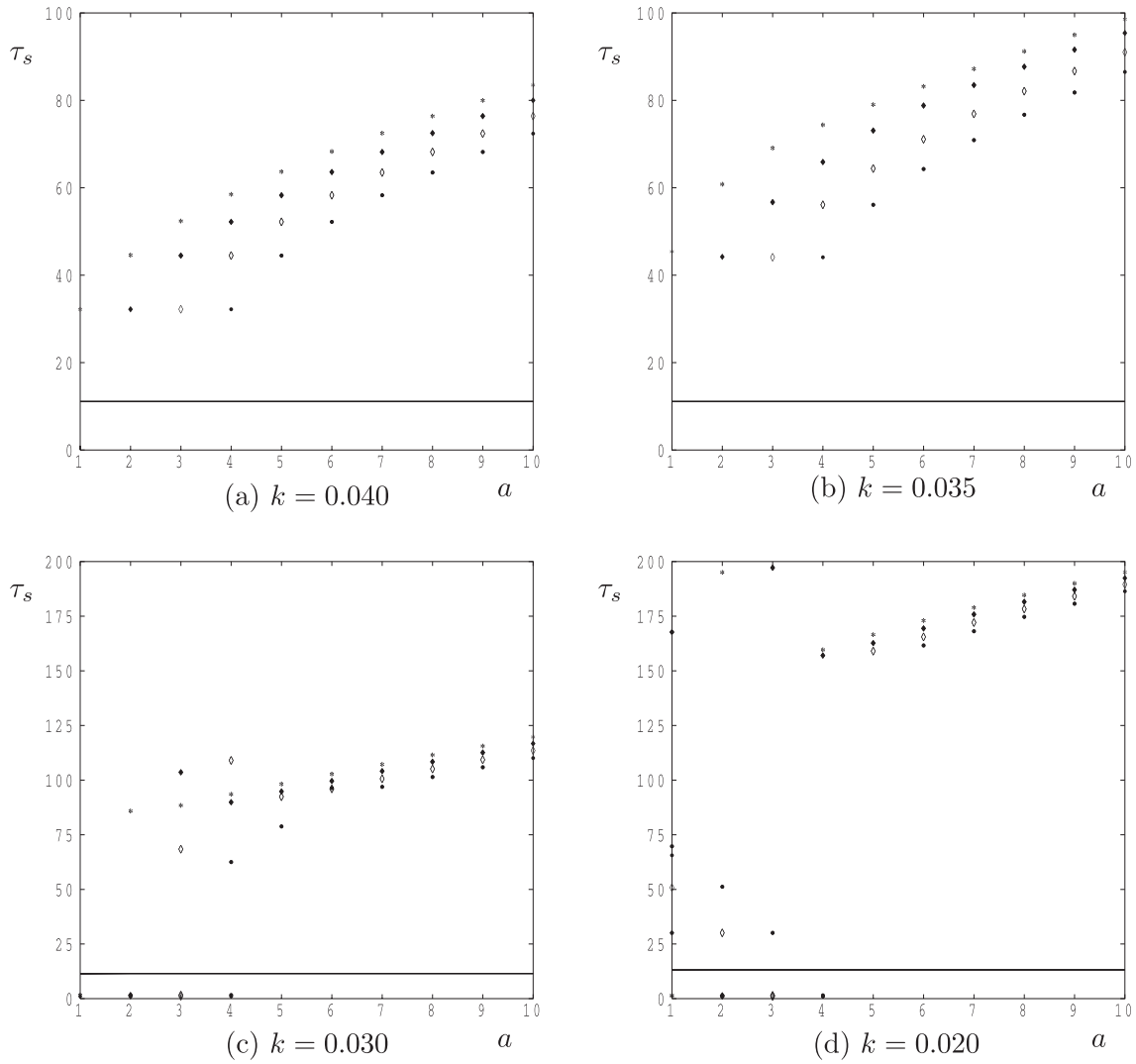

FIG. 5: Variation in the values of the transition time, τ_s, with $a = -\log_{10} A_1$ for different values of A_2 for the wave numbers **(a)** 0.04, **(b)** 0.035, **(c)** 0.03, and **(d)** 0.02. The line near to $\tau = 13$ corresponds the onset of instability of the primary cell. The symbols •, ◊, ♦, and $*$ refer to $A_2 = 10^{-1}$, 10^{-2}, 10^{-3}, and 10^{-4}, respectively.

4.2 The 3:2 Subharmonic Case

We now turn to the 3:2 subharmonic route to destabilization. Here, we consider the primary mode to have wave number $3k$ while the disturbance has wave number $2k$. We shall consider two cases in detail, namely, those for which the primary mode has wave numbers 0.07 and 0.09. These cases represent the typical behavior found during our various simulations.

We consider first the case where $3k = 0.07$. We take $A_3 = 0.1$ as the disturbance amplitude of the primary mode, $A_1 = 0$, and A_2 taking the values, 0, 10^{-6}, 10^{-4}, and 10^{-2}. Figure 6 represents the variation of the surface rate of heat transfer q_n with τ.

When $A_2 = 0$, both q_3, the surface rate of heat transfer of the primary mode, and q_0, the mean change of heat transfer, follow precisely the same evolutionary path as shown in Fig. 2 when neglecting the influence of the subharmonic disturbance, as the wave number of the primary mode is the same in both cases. The other three subfigures show how the primary mode is affected by the presence of three different subharmonic disturbances. In all three

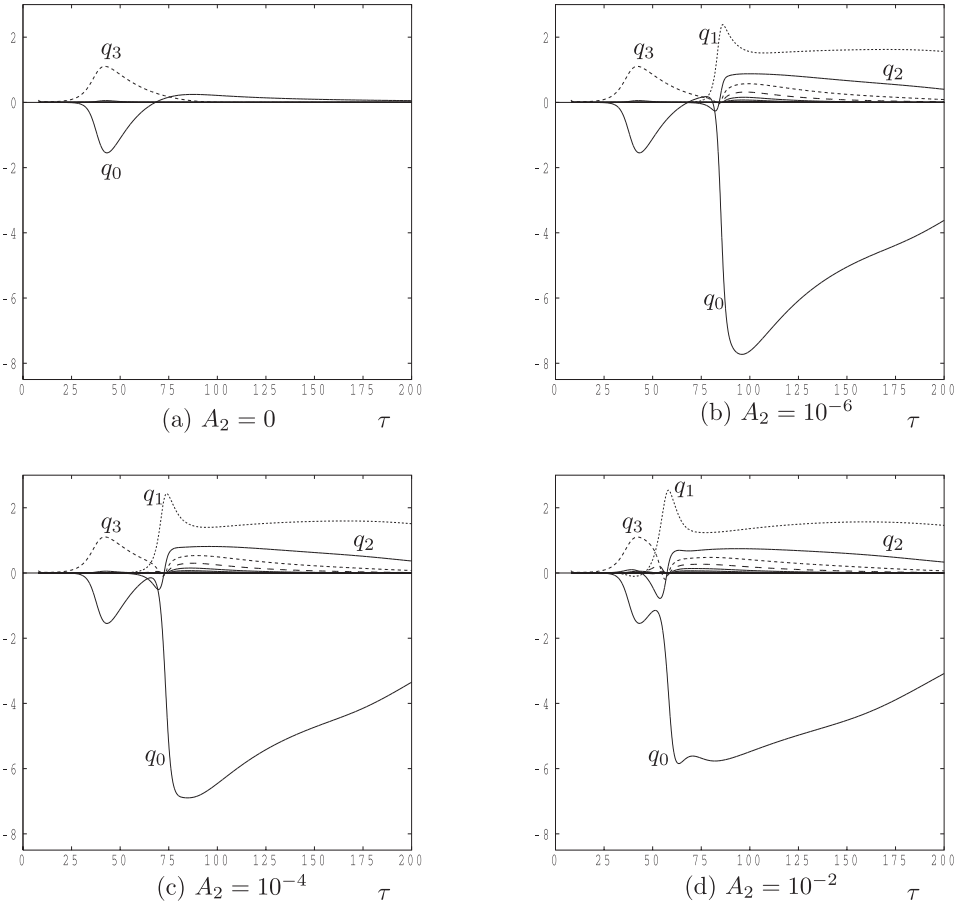

FIG. 6: Variation with τ of the surface rate of heat transfer, q_n, corresponding to the modes, $n = 0$, 1, 2, and 3. The simulations correspond to $\tau_i = 8$, $3k = 0.07$, and $A_1 = 0$; $A_3 = 10^{-1}$; and a selection of values of A_2. Short dashes: q_1; medium dashes: q_3; long dashes: q_4; unbroken curves: q_0, q_2, and all other modes—this convention also applies to Figs. 9 and 12.

of these cases, q_1 and q_2 begin to grow at roughly the same rate, although with different signs. However, mode 1 eventually grows faster, takes over as the dominant mode, with mode 2 following the growth of mode 1 as the latter is the first superharmonic of the former.

On comparing Fig. 6 with Fig. 2, we see that mode 1 also grows very rapidly here, although it is not the subharmonic mode that was introduced. Of interest is the fact that destabilization occurs earlier for the 3:2 case than for the 2:1 case, and the largest absolute mean change to the surface heat transfer q_0 achieves larger values. Thus, it would appear that the 3:2 destabilization is stronger in its effect than the 2:1 case.

Isolines of the surface rate of heat transfer of disturbances $q(x, \tau)$ are shown in Fig. 7 for the cases displayed in Fig. 6. As before, contours are drawn using 20 equally spaced intervals in each subfigure with the middle contour corresponding to a zero value of q. The growth and decay of the primary mode, i.e., when $A_2 = 0$, is shown for reference. The chief difference between these isolines and those in Fig. 3 is that the peak rate of heat transfer for the present case is maintained at a roughly constant level after mode 1 has become established, whereas, for the 2:1 case, the heat transfer begins to decay steadily just after the peak is reached. In fact, this feature is more evident when comparing the q_1 curves in Fig. 6 with those in Fig. 3.

Figures 8(a) and 8(b) represent the detailed isotherms and streamlines of the evolving disturbance, respectively, at different chosen times for the $A_2 = 10^{-2}$ case. Three

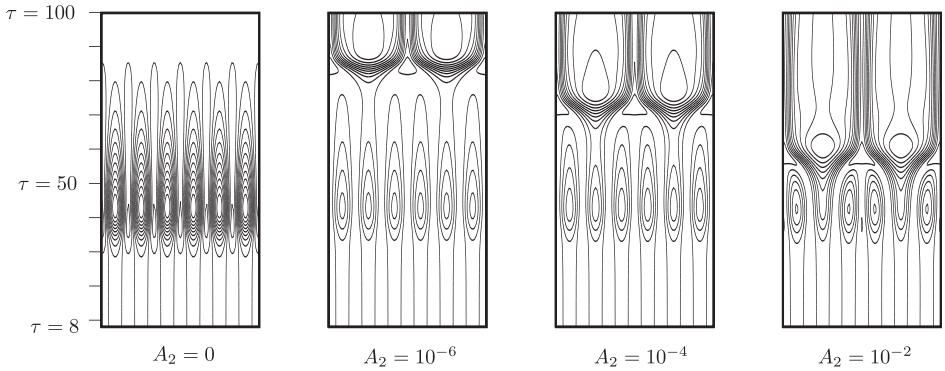

FIG. 7: Isolines of the surface rate of heat transfer, $q(x, \tau)$, for $3k = 0.07$, using $\tau_i = 8$, $A_1 = 0$, $A_3 = 10^{-1}$, and a selection of values of A_2. The horizontal coordinate varies between $x = 0$ and $x = 12\pi/k$; i.e., six horizontal periods, and the vertical axis varies between $\tau = \tau_i = 8$ and $\tau = 100$.

periods of the primary mode are shown and these reduce to one period of mode 1. The evolution of the thermal cells with time is fairly complex and centers around the fact that next-but-one neighbors are not equal in strength. Nonlinear competition then serves to inhibit some thermal cells and to enhance others. If, in the top row of Fig. 8(a), we were to label the cells from 0 to 6, then cells 0 and 2 combine first, thereby eliminating cell 1. The same happens between cells 4 and 6 where cell 5 is eliminated. In the meantime, the middle cell grows and we are left with just one period of a cellular pattern. During the transition, then, two cells disappear while two pairs merge; therefore, at no time do we see a pattern which is at all like a mode 2 pattern with two periods being evident. A similar process happens with the streamlines in Fig. 8(b). Both sets of figures yield a rapidly expanding region of activity, one that is much larger than is depicted in Fig. 4, and this is because the e-folding distance according to Eq. (15) is larger due to k being smaller here than for the cases shown in Fig. 4.

Essentially the same figures are now reproduced in Figs. 9–11 for the case where the primary mode has a wave number of 0.09. We show these because qualitatively different behavior may be found for this choice of wave number.

Figure 1 shows that the expected interval of growth of a mode with a wave number of 0.09 is relatively short, although significant growth can happen. The $A_2 = 0$ subfigure of Fig. 9 appears to show little activity, but this is simply scaled in the same way as for the remaining subfigures. On the other hand, the $A_2 = 0$ subframe of Fig. 10 shows clearly the period of time over which growth occurs, and the mismatch between neighboring thermal cells shows that the mode has become nonlinear, although not strongly so.

Figure 9(b), for which $A_2 = 10^{-6}$, gives an evolutionary behavior that is identical qualitatively to those shown in Fig. 6, in that while mode 2 destabilizes the primary mode (mode 3), it is mode 1 that appears. On the other hand, when the initial amplitude of mode 2 is increased to $A_2 = 10^{-4}$, there is a clear, but short, interval in which mode 2 is dominant before it, too, is overtaken by mode 1. This may be seen in Fig. 10(c) at the point marked by an asterisk where there are now four periods showing, as compared with the original six periods. At larger values of τ there are only two periods of the mode 1 cell.

However, when $A_2 = 10^{-2}$, the successive transitions from mode 3 to mode 2 and from mode 2 to mode 1 takes place in a very clear way with long intervals of time during which each mode is dominant. Interestingly, Fig. 9(d) shows that the transition from mode 2 to mode 1 yields a negative value of q_1, which means that this final transition, a 2:1 subharmonic in effect, yields a pattern that is 180° out of phase with those shown in Fig. 3. Figure 10(d) gives an exceptionally clear representation of both transitions.

Some instantaneous isotherms and streamlines of the evolving disturbance corresponding to the previous two figures are shown in Figs. 11(a) and 11(b) for the cases $A_1 = 0$, $A_2 = 10^{-2}$, and $A_3 = 10^{-1}$. In Figs. 11(a) and 11(b) we see that six cells at $\tau = 10$ transform into four cells at $\tau = 50$ by cell merging and removal, and then into two cells at $\tau = 100$. Of particular interest is the very rapid evolution between $\tau = 90$ and $\tau = 100$, where the cells that are placed close to the heated surface strengthen suddenly.

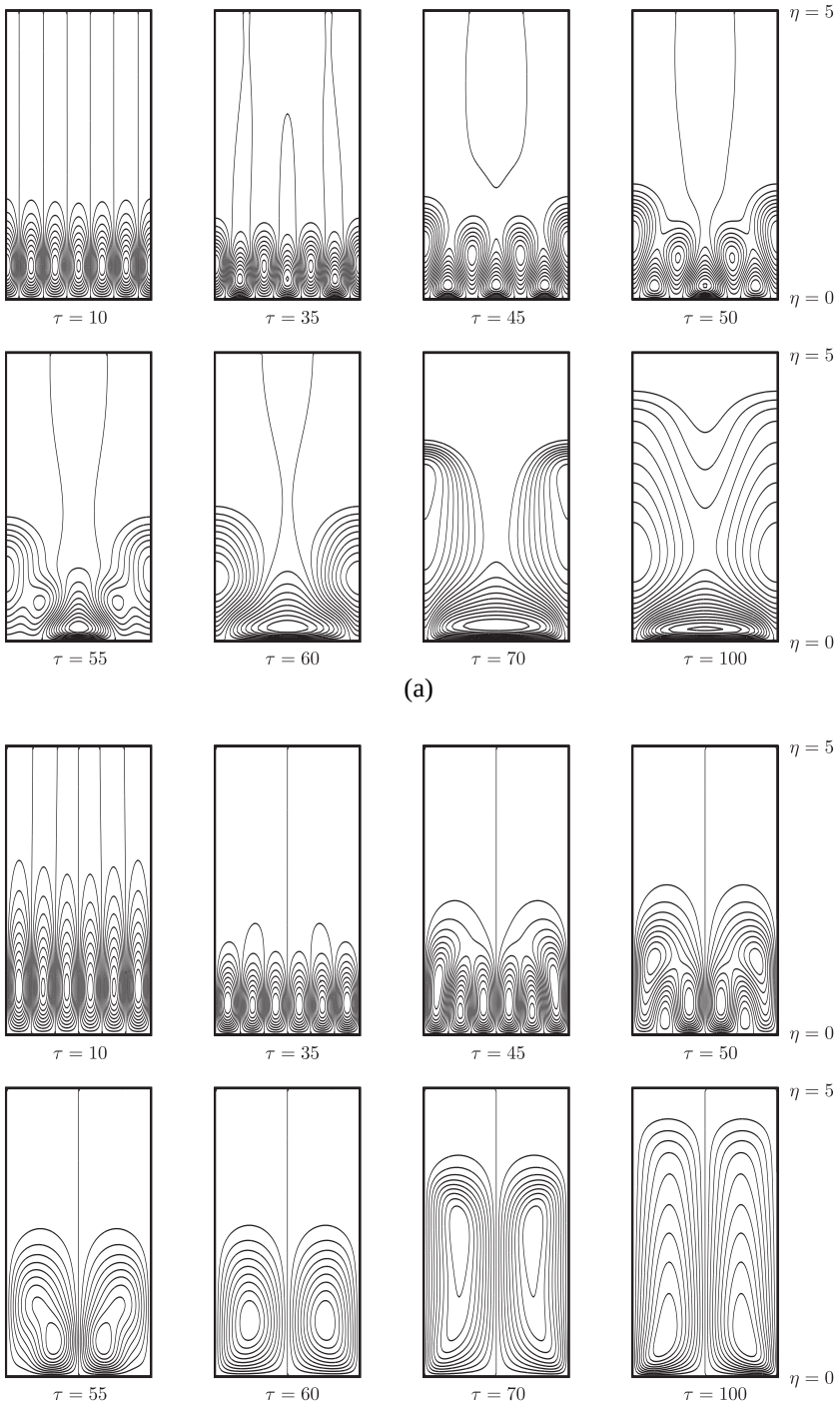

FIG. 8: (a) Contours of the perturbation temperature profiles, and **(b)** streamlines of the evolving flow, at chosen times for the evolution of the subharmonic instability given by $\tau_i = 8$, $3k = 0.07$, $A_1 = 0$, $A_2 = 10^{-2}$, and $A_3 = 10^{-1}$. The horizontal coordinate varies between $x = 0$ and $x = 6\pi/k$; i.e., three horizontal periods.

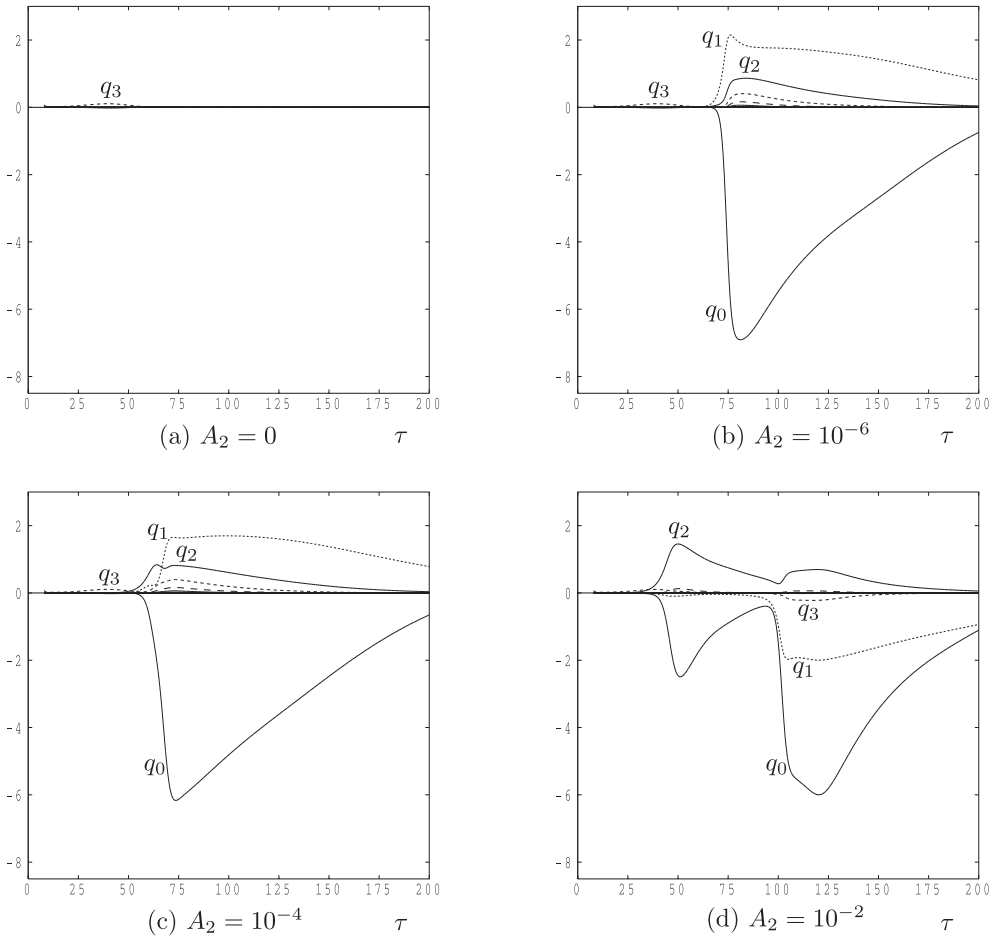

FIG. 9: Variation with τ of the surface rate of heat transfer, q_n, corresponding to the modes, $n = 0$, 1, 2, and 3. The simulations correspond to $\tau_i = 8$, $3k = 0.09$ and $A_1 = 0$, $A_3 = 10^{-1}$, and a selection of values of A_2.

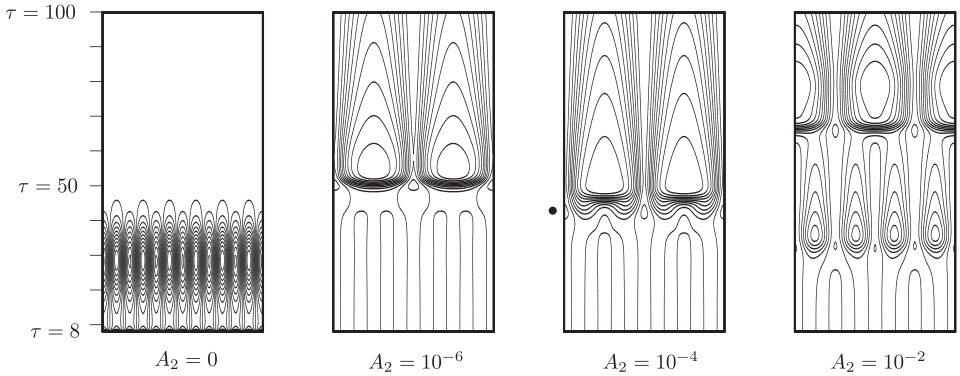

FIG. 10: Isolines of the surface rate of heat transfer, $q(x, \tau)$, for the wave number, $3k = 0.09$, using $\tau_i = 8$, $A_1 = 0$, $A_3 = 10^{-1}$, and a selection of values of A_2. The horizontal coordinate varies between $x = 0$ and $x = 12\pi/k$; i.e., six horizontal periods, and the vertical axis varies between $\tau = \tau_i = 8$ and $\tau = 100$.

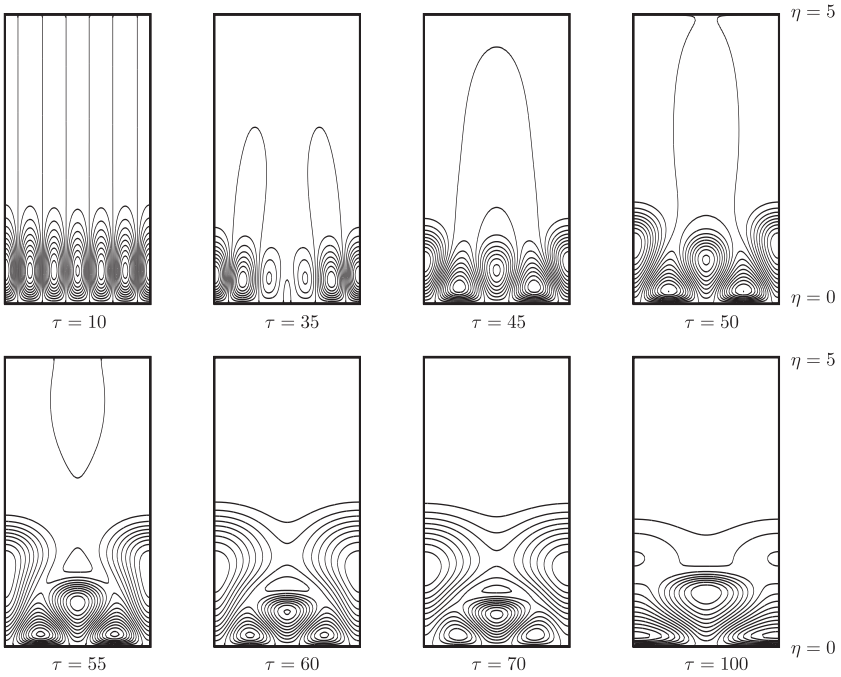

(a)

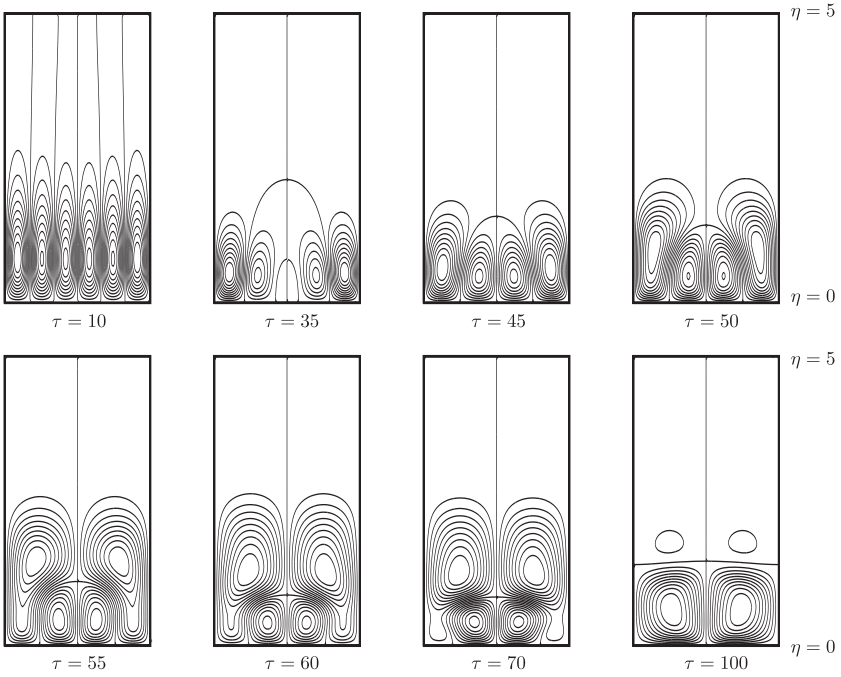

(b)

FIG. 11: (a) Contours of the perturbation temperature profiles, and **(b)** streamlines of the evolving flow, at chosen times for the evolution of the subharmonic instability given by $\tau_i = 8$, $3k = 0.09$, $A_1 = 0$, $A_2 = 10^{-2}$, and $A_3 = 10^{-1}$. The horizontal coordinate varies between $x = 0$ and $x = 6\pi/k$; i.e., three horizontal periods.

4.3 The 4:3 Subharmonic Case

Now we will concentrate on the 4:3 subharmonic case, where modes 3 and 4 in the Fourier expansion represent the subharmonic and primary modes, respectively.

Figure 12 represents the variation of the surface rate of heat transfer q_n with τ. The wave number of the primary mode is given by $4k = 0.07$, and therefore the subharmonic has wave number $3k = 0.0525$. The initial amplitudes of modes 1 and 2 are set to zero, and for the primary disturbance we take $A_4 = 10^{-1}$. As above, we have used the following amplitudes for subharmonic disturbance: $A_3 = 0$, 10^{-6}, 10^{-4}, and 10^{-2}, where $A_3 = 0$ is equivalent to having no subharmonic disturbance. We note that we have again chosen the primary mode to have wave number 0.07, so that all three subharmonic cases (namely, 2:1, 3:2, and 4:3) may be compared.

Figure 12 shows the evolution of the various q_n values with τ, and we find that the ultimate fate of flow depends on the magnitude of the subharmonic disturbance. When $A_3 = 10^{-6}$ the primary mode has decayed almost to nothing before mode 2 makes a brief appearance prior to the establishment of mode 1 as the dominant mode. When A_3 takes larger values, the modal exchanges that take place favor mode 2 as the final convecting state, at least for $\tau \leq 200$. We suspect that mode 1 will destabilize the evolving mode 2 pattern at later times, although we have not tested this hypothesis.

Of interest is the fact that the mean change to the surface rate of heat transfer q_0 is substantially larger when $A_3 = 10^{-6}$ than when A_3 takes the two larger values depicted in Fig. 12. Thus, the magnitude of the response is not necessarily in proportion to the magnitude of the disturbance, but depends on complicated modal exchanges.

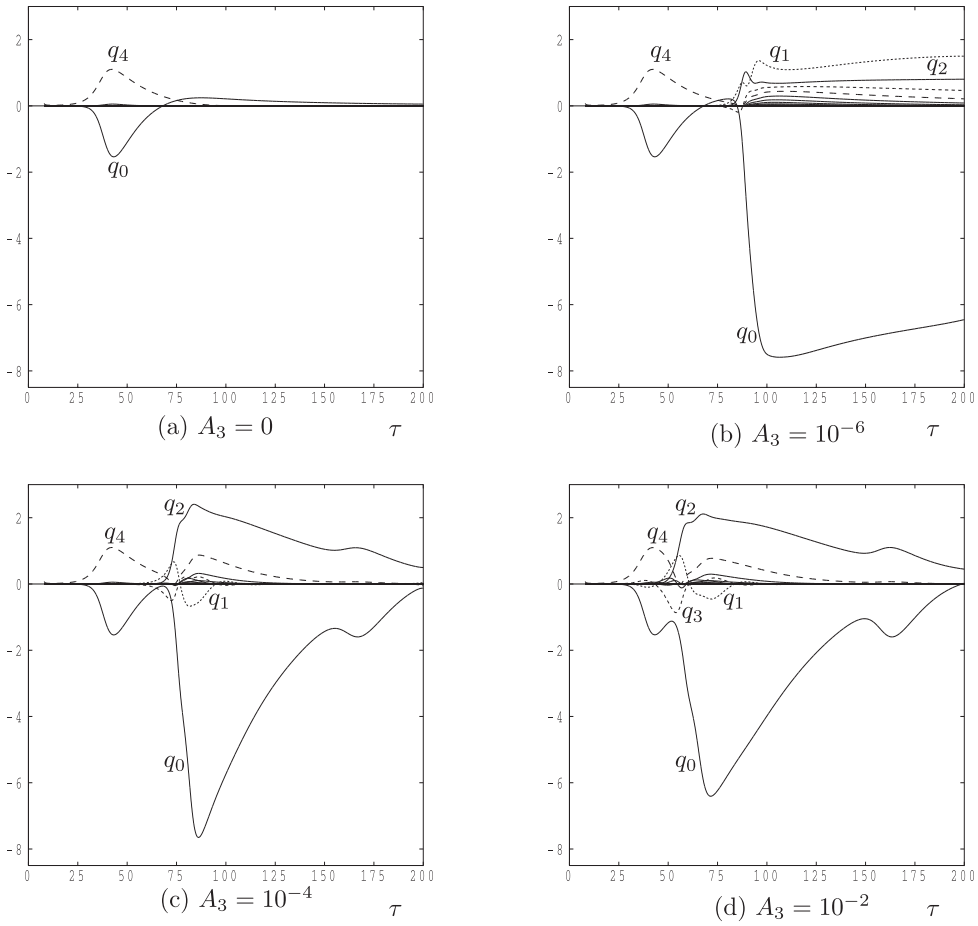

FIG. 12: Variation with τ of the surface rate of heat transfer, q_n, corresponding to the modes, $n = 0$, 1, 2, and 3. The simulations correspond to $\tau_i = 8$, $4k = 0.07$ and $A_1 = 0$, $A_2 = 0$, $A_4 = 10^{-1}$, and a selection of values of A_3.

The surface rates of heat transfer corresponding to the four subfigures in Fig. 12 are depicted in Fig. 13. Here, we see that the initial destabilization of the primary mode is indeed later for the smaller disturbance amplitudes, as one might expect intuitively.

Figure 14 shows instantaneous isotherms and streamlines for the $A_3 = 10^{-2}$ case, for which mode 2 emerges as the dominant mode. We have chosen this case particularly because the surface heat transfer data shown in Fig. 13 do not give a full picture of the complicated evolution that takes place. Concentrating first on the isotherms shown in Fig. 14(a), by the time $\tau = 45$, the thermal cells have either risen or fallen depending on whether they are located where there is outflow or inflow. Moreover, the amount by which the rising cells have risen varies and the pattern is reminiscent of the Eckhaus (or sideband) instability, which is a well-known destabilization mechanism for Bénard–like problems. When $\tau = 55$, the disturbance pattern has modified rapidly into a form that looks superficially like a mode 1 pattern. However, the central cell of this pattern has a detailed three-cell structure close to the surface, and it is this structure that causes q_2 to dominate in Figs. 12 and 13, and that grows strongly as τ increases further. In fact, when $\tau = 100$ the disturbance pattern is a rather unusual mixture of mode 2 near the heated surface and mode 1 further away.

Similar comments may be made about the evolution of the streamlines in Fig. 14(b). The Eckhaus amplitude modulation is very clear when $\tau = 10$, and so is the dual modal structure when $\tau = 100$.

5. DISCUSSION AND CONCLUSIONS

In this paper we have investigated various types of subharmonic instability of an evolving cellular pattern in an unsteady thermal boundary layer in a porous medium. This is an extension of the nonlinear simulations presented in Part II where it was found that, contrary to expectations, the nonlinearly developing cells are always eventually restabilized. In the present paper we have paid particular attention to the 2:1, 3:2, and 4:3 subharmonic cases, and these have all been found to destabilize the primary mode of convection. For the 2:1 case we have provided a comprehensive set of information on how the transition time between the primary and the subharmonic depends on the initial amplitudes of each disturbance. For the 3:2 case we have found two different routes to destabilization: one where mode 3 evolves directly into mode 1 and the other where there is a double transition with mode 3 giving way to mode 2 and then to mode 1. We have also shown some simulations for the 4:3 case, where we have obtained an unusual pattern that consists of one mode near the heated surface and another further away. We have also found that the strength of the response to subharmonic disturbance (in terms of the change in mean rate of heat transfer) is not a smooth function of the amplitude of the disturbance because the identity of the dominant mode also depends on that amplitude.

Given that the passage of time may be interpreted as an increasing Darcy–Rayleigh number, Ra, it is worth making some comparisons with the classical Darcy–Bénard

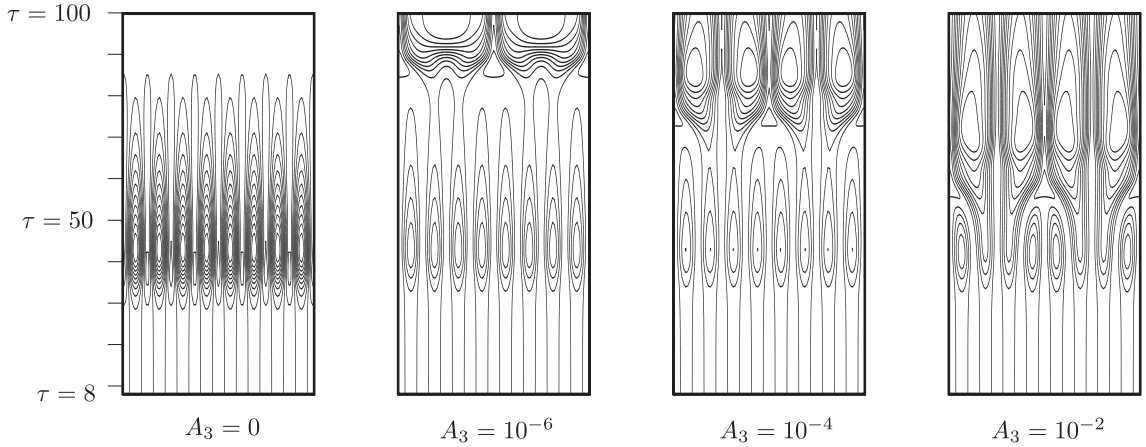

FIG. 13: Isolines of the surface rate of heat transfer, $q(x, \tau)$, for the wave number, $4k = 0.07$, using $\tau_i = 8$, $A_1 = 0$, $A_2 = 0$, $A_4 = 10^{-1}$, and a selection of values of A_3. The horizontal coordinate varies between $x = 0$ and $x = 16\pi/k$; i.e., eight horizontal periods, and the vertical axis varies between $\tau = \tau_i = 8$ and $\tau = 100$.

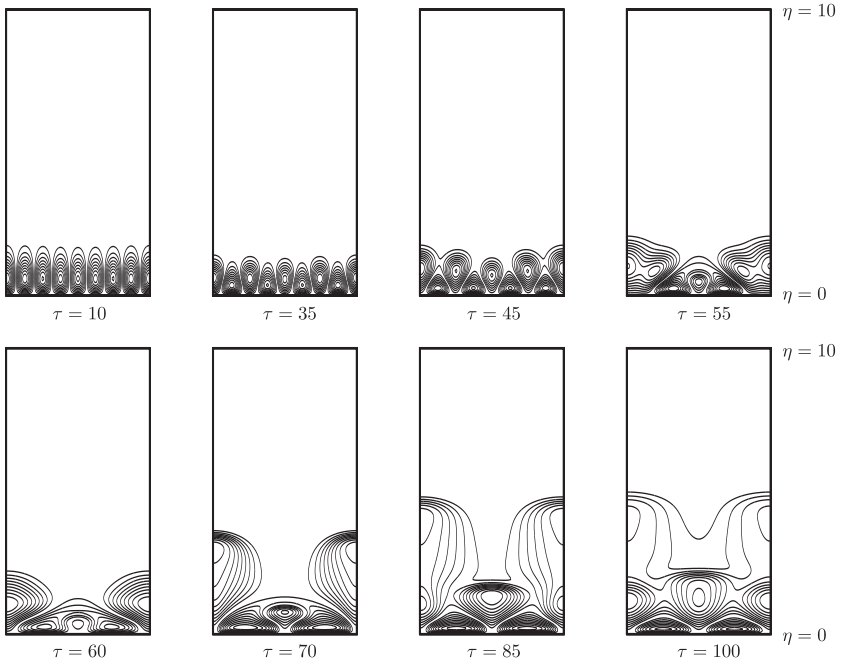

(a)

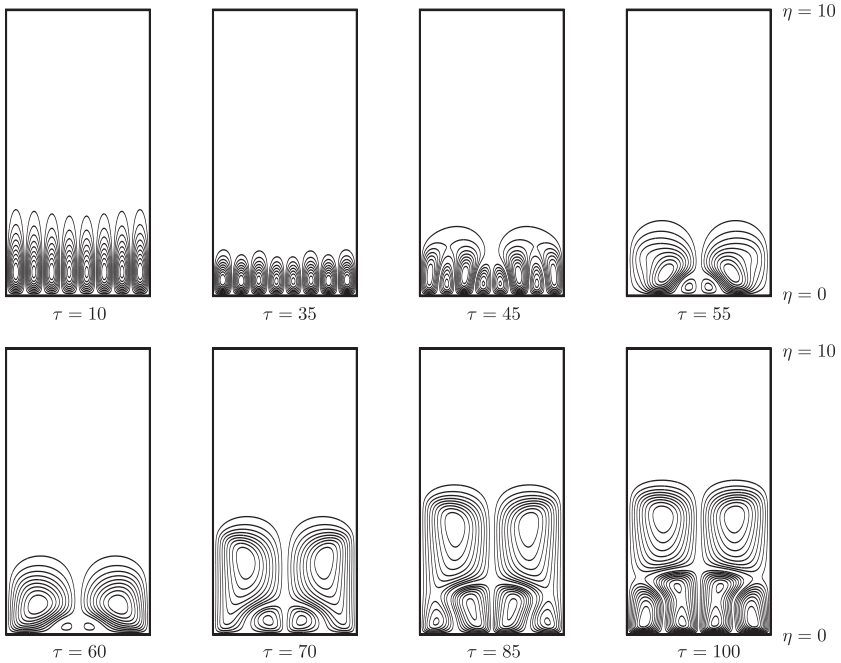

(b)

FIG. 14: (a) Contours of the perturbation temperature profiles, and **(b)** streamlines of the evolving flow, at chosen times for the evolution of the subharmonic instability given by $\tau = \tau_i = 8$, $4k = 0.07$, $A_1 = A_2 = 0$, $A_3 = 10^{-2}$, and $A_4 = 10^{-1}$. The horizontal coordinate varies between $x = 0$ and $x = 8\pi/k$; i.e., four horizontal periods.

problem. The first comprehensive study of the stability of large-amplitude convection in a uniform layer heated from below was undertaken by Straus (1974), who determined the region in wave number/Ra space in which steady two-dimensional convection is stable. Generally, as Ra increases, the range of wave numbers for which convection is stable moves toward higher wave numbers. This is consistent with the computations of Georgiadis and Catton (1986), who found the wave number that corresponds to the largest rate of heat transfer at any chosen value of Ra also increases as Ra increases. The implication of the shape of the stability envelope of Straus (1974) is as follows: should Ra be increased slowly or quasistatically, then eventually convection at the chosen (and originally stable) wave number becomes unstable, and the primary instability mechanism is a cross-roll disturbance with a larger wave number. This observation marks a major qualitative difference between the Darcy–Bénard problem and the present unsteady thermal boundary layer where destabilization causes a reduction in the observed wave number. Although our present calculations are confined to two dimensions, we would expect that any three-dimensional instability mechanism would also consist of roll disturbances (within the linear regime, at least), whose wave number is smaller than that of the evolving pattern; this is the implication of the previously mentioned tendency of cells to try to maintain a roughly $O(1)$ aspect ratio as the boundary layer thickens in time.

Our numerical simulations have the nature of a highly controlled experiment. The adoption of the Fourier ansatz in Eq. (10) means that the results are not affected by noise, taking the form of small-scale random fluctuations, such as one would have quite naturally in a porous medium. In addition, we have not considered the effect of isolated disturbances, nor of three-dimensionality. Indeed, the fact that most of Straus's (1974) stability envelope corresponds to the cross-roll instability suggests that three-dimensional effects may also be significant here. It is also quite certain that the various transitions that we have observed will change should the initiation time we have adopted be changed. In addition, the cascade of instabilities that our computations suggest as a possible destabilization mechanism cannot continue to much later times because the detailed numerical studies of Kimura et al. (1986) and Riley and Winters (1991) suggest that the narrow thermal boundary layer which occurs in the convection cells near to $\eta = 0$ (see the $\tau = 100$ frames in Figs. 4 and 8, for example) may itself be destabilized by traveling waves, thereby leading to yet another potential destabilization mechanism in the present context.

We certainly intend to investigate how isolated disturbances propagate, and preliminary work seems to suggest that the convection cells that are induced tend to have a wavelength that increases with time (Selim 2009). Riaz et al. (2006) also provides much information on chaotic cellular development in two dimensions, but as yet no three-dimensional simulations have been undertaken; it is hoped that this issue also will be addressed in the near future.

ACKNOWLEDGEMENTS

The first author would like to thank the University of Bath for a Departmental Studentship and an Overseas Research Award to enable this research to be undertaken. The authors would like to thank the reviewers for their excellent comments which have served to improve the quality of the manuscript.

REFERENCES

Carslaw, H. S. and Jaeger, J. C., *Conduction of heat in solids*, Oxford University Press, Oxford, 1986.

Ennis-King, J. P. and Paterson, L., Role of convective mixing in the long-term storage of carbon dioxide in deep saline formations, *SPE J.*, vol. **10**, no. 3, pp. 349–356, 2005.

Georgiadis, J. G. and Catton, I., Prandtl number effect on Bénard convection in porous media, *ASME J. Heat Transfer*, vol. **108**, pp. 284–290, 1986.

Kimura, S., Schubert, G., and Straus, J. M., Route to chaos in porous-medium convection, *J. Fluid Mech.*, vol. 166, pp. 305–324, 1986.

Lewis, S., Rees, D. A. S., and Bassom, A. P., High wavenumber convection in tall porous containers heated from below, *Q. J. Mech. Appl. Math.*, vol. **50**, pp. 545–563, 1997.

Rees, D. A. S., Selim, A., and Ennis-King, J. P., The Instability of Unsteady Boundary Layers in Porous Media, *Emerging topics in heat and mass transfer in porous media—from bioengineering and microelectronics to nanotechnology*, (Peter Vadasz, ed.), Springer, pp. 85–110, 2008.

Riley, D. S. and Winters, K. H., Time-periodic convection in porous media: The evolution of Hopf bifurcations with aspect ratio, *J. Fluid Mech.*, vol. **223**, pp. 457–474, 1991.

Riaz, A., Hesse, M., Tchelepi, H. A., and Orr, F. M., Onset of convection in a gravitationally unstable diffusive boundary layer in porous media, *J. Fluid Mech.*, vol. **548**, pp. 87–111, 2006.

Selim, A., Instability of unsteady boundary layers in porous media, Ph.D. thesis (University of Bath), 2009.

Selim, A. and Rees, D. A. S., The instability of a developing

thermal front in a porous medium. I Linear theory, *J. Porous Media*, vol. **10**, pp. 1–15, 2007a [Part I].

Selim, A. and Rees, D. A. S., The instability of a developing thermal front in a porous medium. II Nonlinear evolution, *J. Porous Media*, vol. **10**, pp. 17–33, 2007b [Part II].

Socolow, R. H., Can we bury global warming?, *Sci. Am.*, July, pp. 49–55, 2005.

Straus, J. M., Large amplitude convection in porous media, *J. Fluid Mech.*, vol. **64**, pp. 51–63, 1974.

Wooding, R. A., Tyler, S. W., and White, I., Convection in groundwater below an evaporating salt lake. I. Onset of instability, *Water Resour. Res.*, vol. **33**, pp. 1199–1218, 1997.

Xu, T., Apps, J. A., and Pruess, K., Numerical simulation of CO_2 disposal by mineral trapping in deep aquifers, *Appl. Geochem.*, vol. **19**, pp. 917–936, 2004.

Journal of Porous Media 13(12), 1059–1072 (2010)

BUOYANCY OPPOSED MIXED CONVECTION IN A TWO-SIDED LID-DRIVEN DIFFERENTIALLY HEATED SQUARE CAVITY FILLED WITH A POROUS MEDIUM

Elaprolu Vishnuvardhanarao[1] & Manab Kumar Das[2,*]

[1]*Fluidyn Software and Consultancy Pvt Ltd. Bangalore-560 102, India*

[2]*Department of Mechanical Engineering, Indian Institute of Technology Kharagpur, West Bengal, 721302, India*

[*]Address all correspondence to Manab Kumar Das E-mail: manab@mech.iitkgp.ernet.in

Original Manuscript Submitted: 2/11/2009; Final Draft Received: 5/11/2009

Mixed convection flow in a two-dimensional square cavity filled with a Darcian fluid-saturated uniform porous medium is considered. The cold vertical wall at the left is moving up whereas the hot wall in the right is moving down. The fixed top and the bottom walls are thermally insulated. The normalized governing equations are solved numerically with appropriate boundary conditions by finite volume approach. The code has been validated with previously published work and the results are found to be in excellent agreement. The study is conducted by varying the Richardson number $Ri = (Gr/Re^2)[Ri = (Gr/Re^2)]$*, Darcy number (*$Da = \kappa/H^2\kappa$*, Grashof number* $Gr = (g\beta\Delta TH^3/\upsilon^2)[Gr = (g\beta\Delta TH^3/\upsilon^2)]$*. The Prandtl number is fixed at 0.71. A parametric study is conducted and a set of streamlines and isotherm plots are presented. A heat transfer correlation is also presented.*

KEY WORDS: *lid-driven cavity, mixed convection, porous medium, numerical simulation*

1. INTRODUCTION

Heat and fluid flow studies in porous medium have been done on many occasions on geothermal systems (Cheng, 1978), drying of porous solids, solar collectors (Ideriah, 1980), furnaces, and many others. Moreover, mixed convection problems with lid-driven flows in enclosures are encountered in a variety of engineering applications including cooling of electronic devices, lubrication technologies, chemical processing equipment, float glass production (Pilkington, 1969), etc. Iwastu et al. (1993) reported mixed convection in a lid-driven cavity with a stable vertical temperature gradient. The flow and heat transfer study of viscous fluid contained in a square cavity have been done, where the top wall is moving at constant speed and the remaining walls are kept fixed. The isothermal top wall is hotter than the cold bottom wall and the side walls are adiabatic. Numerical experiments were reported for a range of Richardson numbers ($0 \leq \mathrm{Ri} \leq 10^6$) and Reynolds numbers ($0 \leq \mathrm{Re} \leq 3000$). The computed results indicate the effect of the Richardson number on the flow field. The study of mixed convection in a square enclosure with side walls moving was done by Oztop and Dagtekin (2004). They considered the range of Richardson numbers $0.01 \leq \mathrm{Ri} \leq 100$ in which the Prandtl number was fixed at 0.7. For $\mathrm{Ri} < 1$, the influence of moving walls during heat transfer is the same when the side walls move in the opposite direction regardless of the direction of the walls. For the case of opposing buoyancy and shear forces, and for $\mathrm{Ri} > 1$, the heat transfer is some what better due to the formation of secondary cells on the walls. Kuhlmann et al. (1997) have presented experimental and numerical results on the steady flow in rectangular cavities. The flow is driven by moving two facing walls tangentially in opposite directions. They concluded that the basic two-dimensional flow was not always unique. For low Reynolds numbers, the flow consists of two separate co-rotating vortices adjacent to the moving walls.

1091–028X/10/$35.00

NOMENCLATURE

A	surface area (m^2)
Da	Darcy number (κ/H^2)
g	gravitational acceleration (m/s^2)
Gr	Grashof number [$Gr = (g\beta\Delta T H^3/\upsilon^2)$]
H	enclosure length (m)
i	*x*-direction grid point
j	*y*-direction grid point
k_e	effective thermal conductivity of the porous medium (W/m K)
k_s	thermal conductivity of the solid (W/m K)
k	thermal conductivity ratio (k_s/k_f)
Nu	local Nusselt number
$\overline{Nu}$	average Nusselt number
n	time level
p	nondimensional pressure
Pr	Prandtl number (υ/α_e)
Q	constant
Re	Reynolds number of the fluid ($V_p H/\upsilon$)
Ri	Richardson number [$Ri = (Gr/Re^2)$]
T	dimensional temperature (°C)
u^*, v^*	dimensional velocity components along (*x*,*y*) axes (m/s)
u_r	dimensionless resultant velocity
u, v	dimensionless velocity components along (*X*,*Y*) axes
x^*, y^*	dimensional Cartesian coordinates (m)
x, y	dimensionless Cartesian coordinates

Greek Symbols

α_e	effective thermal diffusivity of porous medium (m^2/s)
β	fluid thermal expansion coefficient
β_s	solid expansion coefficient
θ	dimensionless temperature [$(T - T_c)/(T_h - T_c)$]
υ	effective kinematic viscosity (m^2/s)
κ	permeability of the porous medium (m^2)

Subscripts

c	cold wall
f	fluid
h	hot wall

Superscripts

*	dimensional form

Blohm and Kuhlmann (2002) have investigated experimentally the flow in a rectangular cavity driven by two facing side walls that move steadily in anti-parallel directions for Reynolds numbers up to 1200. They concluded that beyond a first threshold, robust, steady, three-dimensional cells bifurcate super-critically out of the basic flow state. The oscillatory instability is found to be tri-critical if both side walls move with the same velocity (symmetrical driving). The non-Darcian effects were considered by Vafai and Tien (1981), where they studied the inertia and boundary effects on flow and heat transfer in porous media. Lauriat and Prasad (1989) studied the relative importance of inertia and viscous forces on natural convection in porous media via the Darcy–Brinkman–Forchheimer solutions for a differentially heated vertical cavity. Khanafer and Chamkha (1999) investigated a mixed convection flow in a lid-driven cavity enclosure filled with a fluid-saturated porous medium. In their work, the Brinkman-extended Darcy equation of motion was used and the influence of the Richardson and Darcy numbers on the flow was studied. Many authors have reported mixed convection flows with Darcian and non-Darcian effects along vertical plates embedded in porous media (e.g., Lai and Kulacki, 1991; Hsieh et al., 1993) or in rectangular geometries filled with porous media (e.g., Nithiarasu et al., 1997, 1998). Recently, Vishnuvardhanarao and Das (2008) studied the mixed convection flow in a square cavity filled with porous medium, in which the left wall was moving up and was maintained at a constant cold temperature—thus opposing the buoyancy force. The right wall also was moving up with the same velocity and was maintained at a constant hot temperature—thus aiding the buoyancy. These effects have been reported and an empirical correlation has been presented. In the present study, the mixed convection flow in a square cavity filled with porous media is considered. The left wall is moving up and is maintained at a constant cold temperature, whereas the right is moving down and maintained at a

constant hot temperature. The objective of the present work is to consider the Brinkman-extended Darcy equation of motion with the convective terms included, as was used by Khanafer and Chamkha (1999). The governing parameters are Richardson numbers (Ri) and Darcy numbers (Da) for a range of Grashof numbers (Gr).

2. PROBLEM DESCRIPTION

The physical model considered is shown schematically in Fig. 1. A two-dimensional square cavity of height *H* is filled with fluid-saturated uniform porous medium and permeability. The top and the bottom surfaces of the cavity are thermally insulated. The left and the right walls are maintained at temperatures T_c and T_h, respectively, as shown. The left wall is moving up and the right wall is moving down. The velocities of the moving walls are equal and the directions are as shown. The direction of the gravitational force and the *x*–*y* coordinate system are also shown in the Fig. 1.

3. GOVERNING EQUATIONS

Flow is assumed to be two-dimensional, steady, and laminar and the fluid is assumed to be incompressible. The thermophysical properties are assumed to be constant except for the body force term in the momentum equation, which has been approximated by the Boussinesq approximation. Radiation heat transfer is considered negligible with respect to other modes of heat transfer. Inertia effects of the porous medium are negligible, which is appropriate when the Reynolds number is small (Khanafer and Chamkha, 1999). By considering the assumptions mentioned above, the nondimensional form of the governing equations can be written using the following dimensionless variables:

$$x = \frac{x^*}{H}, \quad y = \frac{y^*}{H}, \quad u = \frac{u^*}{V_p}, \quad v = \frac{v^*}{V_p}, \quad p = \frac{p^*}{\rho_0 V_p^2}, \quad \theta = \frac{T - T_c}{T_h - T_c} \tag{1}$$

The resulting dimensionless equations are

$$\frac{\partial u}{\partial x} + \frac{\partial v}{\partial y} = 0 \tag{2}$$

$$u\frac{\partial u}{\partial x} + v\frac{\partial u}{\partial y} = -\frac{\partial p}{\partial x} + \frac{1}{\mathrm{Re}}\left(\frac{\partial^2 u}{\partial x^2} + \frac{\partial^2 u}{\partial y^2}\right) - \frac{u}{\mathrm{Da}\cdot\mathrm{Re}} \tag{3}$$

$$u\frac{\partial v}{\partial x} + v\frac{\partial v}{\partial y} = -\frac{\partial p}{\partial y} + \frac{1}{\mathrm{Re}}\left(\frac{\partial^2 v}{\partial x^2} + \frac{\partial^2 v}{\partial y^2}\right) + \frac{\mathrm{Gr}}{\mathrm{Re}^2}\theta - \frac{v}{\mathrm{Da}\cdot\mathrm{Re}} \tag{4}$$

$$u\frac{\partial \theta}{\partial x} + v\frac{\partial \theta}{\partial y} = \frac{1}{\mathrm{Re}\cdot\mathrm{Pr}}\left(\frac{\partial^2 \theta}{\partial x^2} + \frac{\partial^2 \theta}{\partial y^2}\right) \tag{5}$$

where

$$\mathrm{Re} = V_p H/\upsilon; \quad \mathrm{Gr} = \frac{g\beta\Delta T H^3}{\upsilon^2}; \quad \mathrm{Da} = \kappa/H^2; \quad \mathrm{Pr} = \upsilon/\alpha_e \tag{6}$$

The dimensionless boundary conditions are given as follows:

Left wall: $u = 0.0$, $v = 1.0$, $\theta = 0.0$
Right wall: $u = 0.0$, $v = -1.0$, $\theta = 1.0$
Top wall: $u = 0.0$, $v = 0.0$, $(\partial\theta/\partial y) = 0$
Bottom wall: $u = 0.0$, $v = 0.0$, $(\partial\theta/\partial y) = 0$

The average Nusselt number ($\overline{\mathrm{Nu}}$) is calculated by integrating the local Nusselt number (Nu) along the left wall and is given by

$$\overline{\mathrm{Nu}} = \int_0^1 \mathrm{Nu}\, dy \tag{7}$$

where the local Nusslet number is defined as

$$\mathrm{Nu} = -\left.\frac{\partial \theta}{\partial x}\right|_w \tag{8}$$

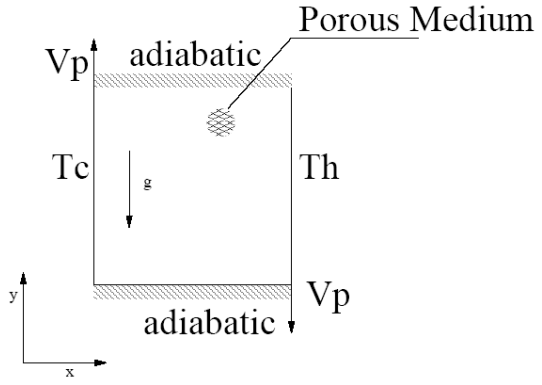

FIG. 1: Schematic diagram and boundary conditions

4. NUMERICAL PROCEDURE

Governing Eqs. (2)–(5) are discretized on a structured collocated grid. The velocity components (*u*, *v*) and the scalar variables (pressure, temperature) are located at the

center of the control volume in a nonstaggered manner. The governing equations are solved numerically by the finite-volume method. The semi-implicit method for pressure-linked equation (SIMPLE) (Patankar, 1980) is used to couple the momentum and the continuity equations. In the nonstaggered grid, the momentum interpolation of Rhie and Chow (1983) has been used to avoid the checkerboard solution.

The deferred quadratic upstream interpolation for convection kinematics (QUICK) scheme is employed to minimize the numerical diffusion for the convective terms in both the momentum and energy equations (Hayase et al., 1992). The solution of the discretized momentum and pressure correction equation is obtained by the line-by-line method. The pseudo-transient approach is followed for the numerical solution as it is useful for situations in which the governing equations give rise to stability problems, e.g., buoyant flows (Versteeg and Malalasekera, 1996). The iterative procedure is initiated by the solution of the energy equation followed by momentum equations and is continued until convergence is achieved. To get a converged solution, the Euclidean norm was used to calculate the error (Van Doormaal and Raithby, 1984) and its value was set to 10^{-6} for dependent the variable ϕu, v, θ and the mass residual was set to 10^{-10}. An underrelaxation of 0.2 is used for pressure.

5. CODE VALIDATION AND GRID INDEPENDENCE STUDY

Validation of the developed code was done for mixed convection flow in a lid-driven enclosure filled with a fluid-saturated porous medium problem of Khanafer and Chamkha (1999). Vishnuvardhanarao and Das (2008) show comparisons of midplane u-velocity, midplane v-velocity, and midplane temperature in their Figs. 3(a), 3(b), and 3(c), respectively. The results are in very good agreement with the benchmark solution for the range of parameters considered. To test and assess the grid independent solutions, numerical experiments were performed for the following grid sizes: 61×61, 81×81, 101×101, 121×121, and 141×141, with extreme values of Richardson numbers (Ri $= 0.01$ and 100) and Darcy numbers (Da $= 10^{-4}$ and ∞). The u-velocity in the horizontal midplane, v-velocity in the vertical midplane, and temperature in the horizontal midplane are shown in Figs. 2(a)–2(c), respectively, for all the grid sizes. It is observed that the curves overlap with each other for 121×121 and 141×141. A grid number of 121×121 is chosen for further computations.

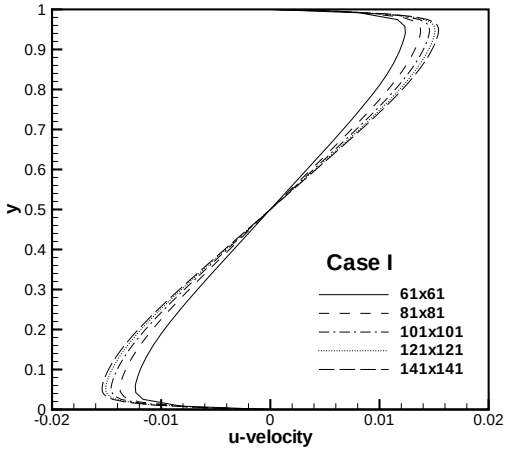

(a)

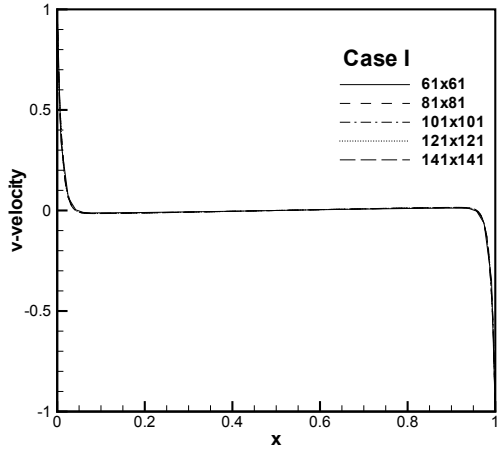

(b)

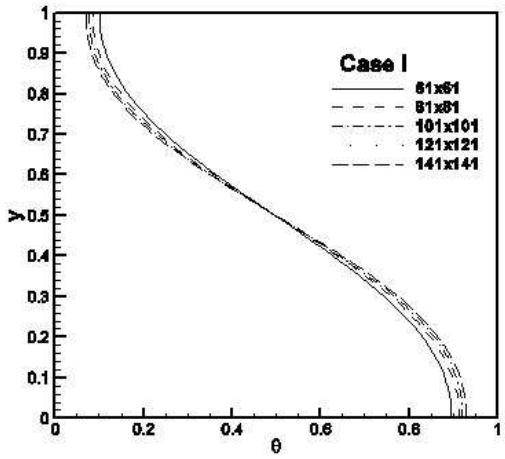

(c)

FIG. 2: Grid independence study

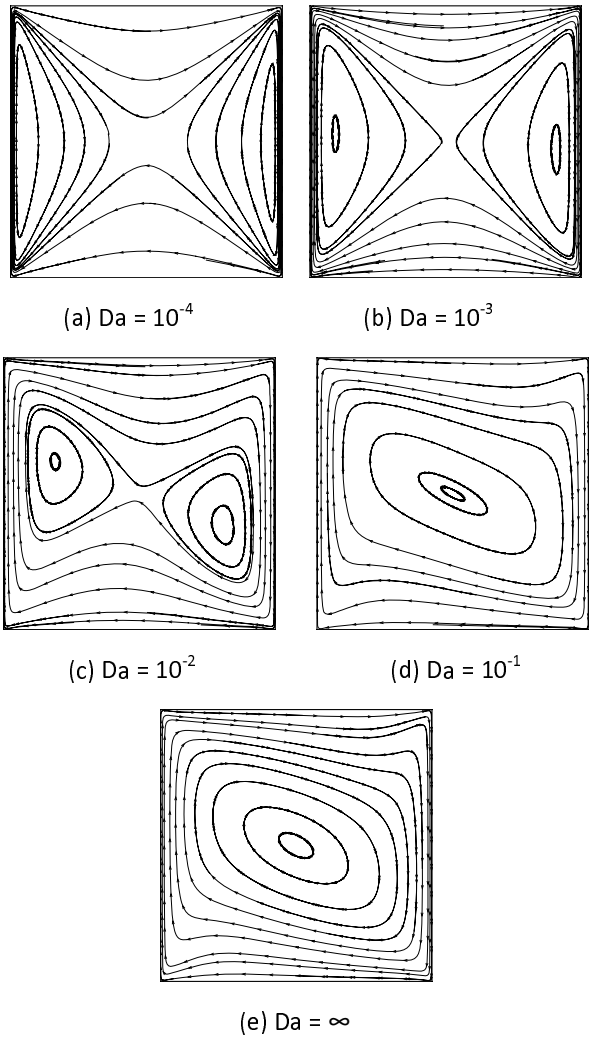

FIG. 3: Streamline plots for Ri $= 10^{-2}$, Gr $= 10^2$ and for various Darcy numbers (Da)

6. RESULTS AND DISCUSSION

In this section, the numerical results for mixed convection flow and heat transfer in a two-sided lid-driven cavity in the presence of uniform porous medium are discussed. The nondimensional governing parameters are the Richardson number that signifies the relative dominance of buoyancy to forced convection and the Darcy number that inversely accounts for the intensity of porous medium. To vary the Richardson number, the Grashof number is fixed at three levels, i.e., at 10^2, 10^3, and 10^4, and correspondingly, the Reynolds number is varied. At each Ri, the Darcy number is varied between 10^{-4} and 10^{-1}, without the presence of porous medium (i.e., Da $= \infty$) and the computations are carried out. For analyzing the characteristics, the streamline and isotherms for one forced convection dominated flow (Ri $= 10^{-2}$) and the other natural convection dominated flow (Ri $= 10^2$) are reported for different Darcy numbers.

In the present case, the forces generated at the sliding lids are opposite to the buoyancy force. Figures 3(a)–3(e) and 4(a)–4(e) represent the streamline and temperature contours, respectively, for Ri $= 10^{-2}$, and Gr $= 10^2$ for different Darcy numbers. It is observed that for Da $= 10^{-4}$ [Fig. 3(a)], most of the flow is attenuated due to the effect of porous medium, convection is limited to near the sliding lids, and isotherms [Fig. 4(a)] are nearly vertical, representing heat transfer by conduction.

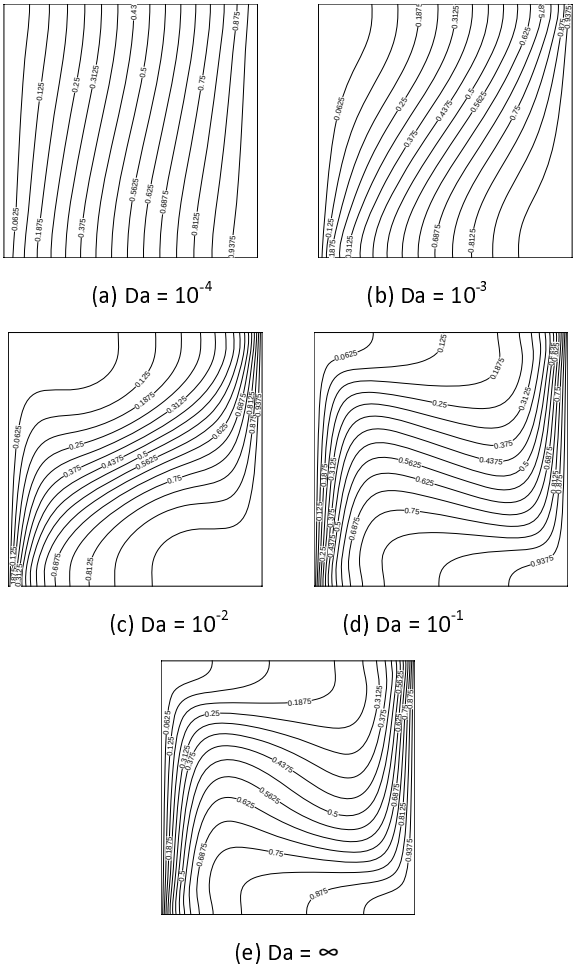

FIG. 4: Temperature contours for Ri = 10^{-2}, Gr = 10^2 and for various Darcy numbers (Da)

As the Darcy number is increased, the strength of convection is increased. The convection domain becomes larger and vortices are generated near the moving lid [Fig. 3(b)]. The vortices grow bigger in size and move closer together [Fig. 3(c)] and they finally merge together and form a single vortex, which is close to the center of the cavity [Figs. 3(d) and 3(e)]. Here, the direction of the vortex is clockwise. The isotherm plots also show a gradual increase in the strength of convection, which is observed by the deviation of the shape of the constant temperature lines and also the formation of the thermal boundary layers on the two vertical walls. The top wall becomes cooler and the bottom wall becomes hotter, which represents forced convection dominated flow. Figures 5(a)–5(e) and 6(a)–6(e) represent the streamline and temperature contours, respectively, for Ri $= 10^{-2}$ and Gr $= 10^4$ for different Darcy numbers. Since Ri is kept constant as Gr is increased to 10^4, Re is increased (Re $= 10^3$) compared with the previous case (Re $= 10^2$). Because of the high inertia force, as the Darcy number is increased, the vortices are shifted to the corners [Fig. 5(b)] and they finally merge together at early Da $= 10^{-2}$ [Fig. 5(c)]. By the same reason, two small vortices are observed at the top-right and the bottom-left corners. The effect of thermal convection is observed even at low Da $= 10^{-4}$ [Fig. 6(a)]. The strength increases with the increase in Da [Figs. 6(b)–6(d)]. At Da $= \infty$ the shape of the isotherms [Fig. 6(e)] is similar to those in a lid-driven cavity flow problem. The formation of the thermal boundary layer at the two moving walls is noticed.

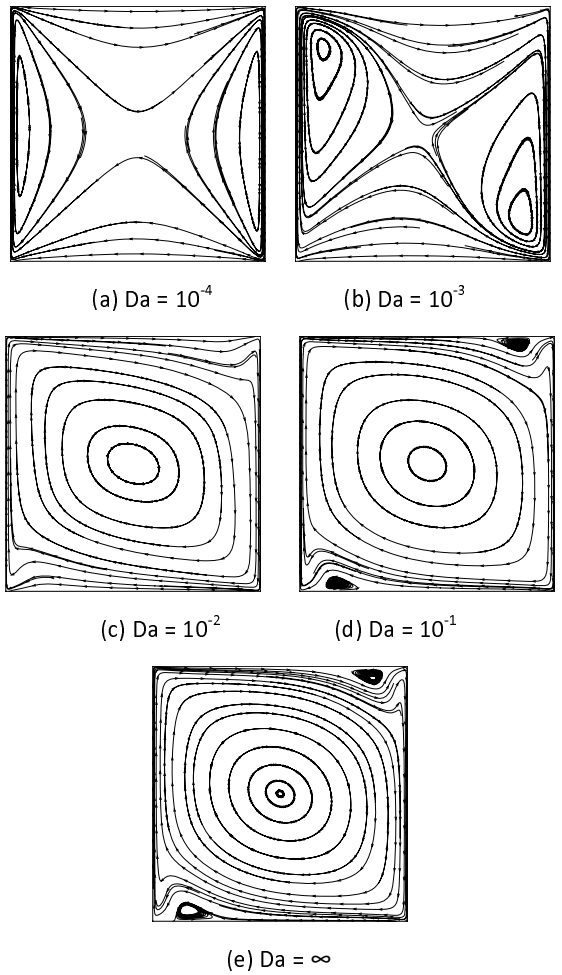

FIG. 5: Streamline plots for Ri $= 10^{-2}$, Gr $= 10^4$ and for various Darcy numbers (Da)

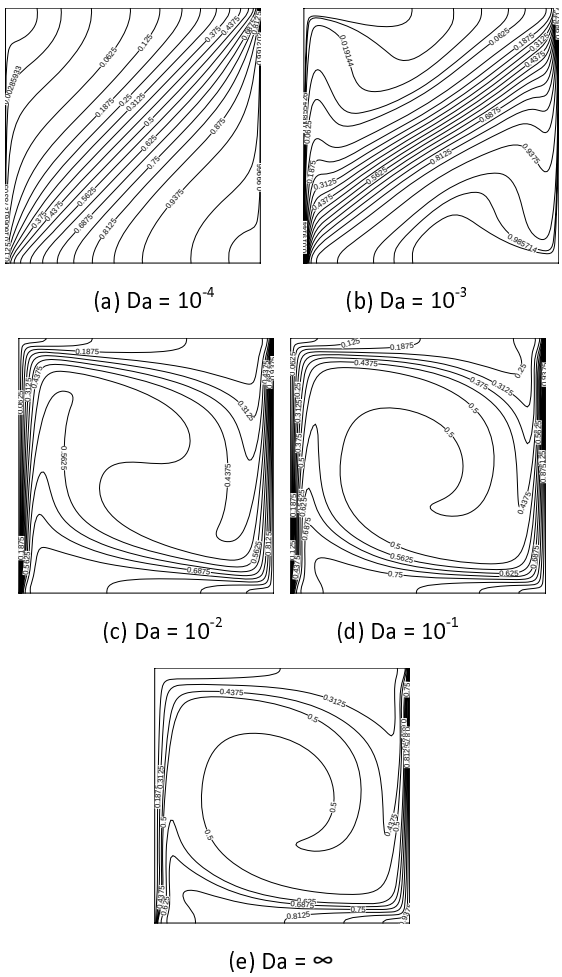

FIG. 6: Temperature contours for Ri $= 10^{-2}$, Gr $= 10^4$ and for various Darcy numbers (Da)

Figures 7(a)–7(e) and 8(a)–8(e) represent the streamline and temperature contours, respectively, for Ri $= 10^2$ and Gr $= 10^2$ for different Darcy numbers. In the present case, the Reynolds number is equal to 1. As the Ri is high, there is a relative dominance of natural convection over the forced convection heat transfer. It is noted that for Da $= 10^{-4}$ [Fig. 7(a)], the flow is confined near to the sliding lids and the vortices are also confined to the walls. As the Darcy number is increased, the vortices move away from the sliding lids [Fig. 7(b)]. Also, new vortices are generated at the top and bottom walls of the cavity due to the natural convection [Fig. 7(c)]. As Da $= 10^{-1}$, the size of these vortices (top and bottom) increase and they merge together [Fig. 8(d)]. The direction of this vortex is anti-clockwise (an effect of the natural convection phenomenon). Even for large Da [Fig. 7(e)], the situation remains same. The isotherms for all Darcy numbers are nearly vertical, indicating the convection currents are very low [Figs. 8(a)–8(e)].

Figures 9(a)–9(e) and 10(a)–10(e) represent the streamline and temperature contours, respectively, for Ri $= 10^2$ and Gr $= 10^4$ for different Darcy numbers. The Reynolds number in the present case is 10. For a low Da $= 10^{-4}$ [Fig. 9(a)], a vortex due to natural convection is observed at the center. Due to the sliding lids, there are two vortices near the side walls. As the Darcy number

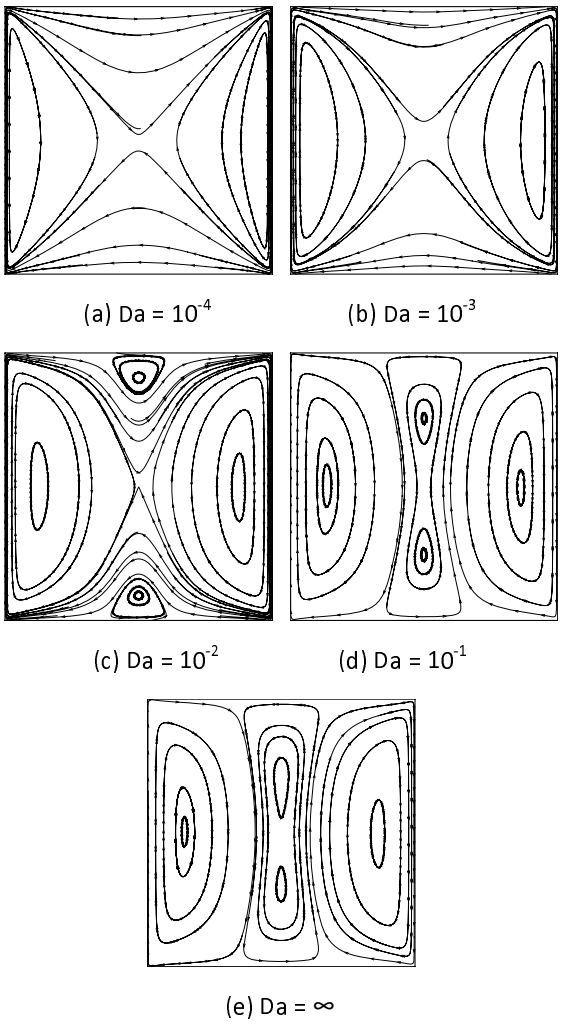

FIG. 7: Streamline plots for Ri $= 10^2$, Gr $= 10^2$ and for various Darcy numbers (Da)

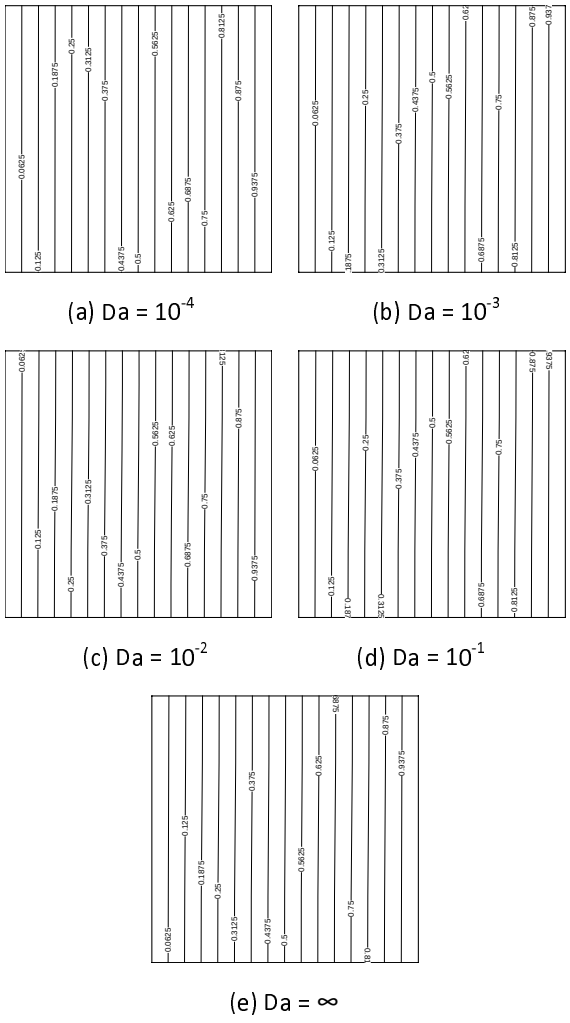

FIG. 8: Temperature contours for Gr $= 10^2$ and for various Darcy numbers (Da)

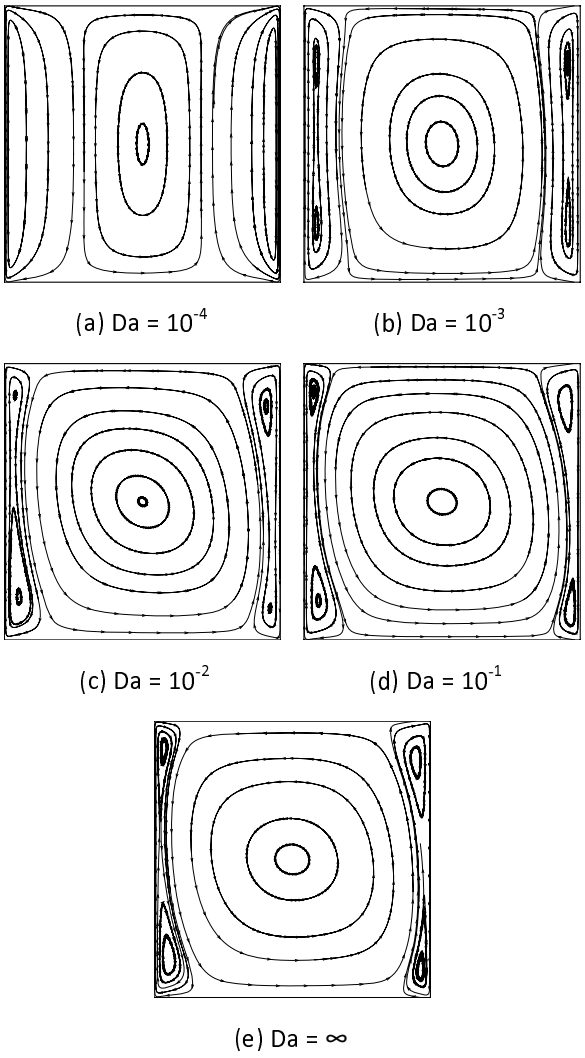

FIG. 9: Streamline plots for Ri $= 10^2$, Gr $= 10^4$ and for various Darcy numbers (Da)

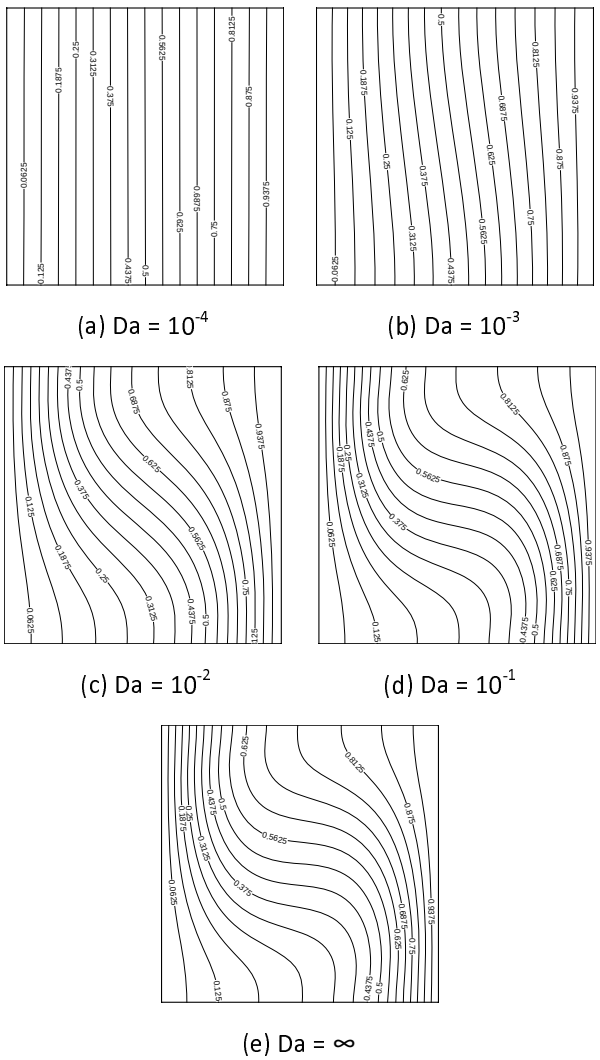

FIG. 10: Temperature contours for Ri $= 10^2$, Gr $= 10^4$ and for various Darcy numbers (Da)

increases, the center vortex becomes larger in size and two vortices near the walls are reduced to smaller regions [Figs. 9(b)–9(e)]. Each one finally splits into two vortices, which clearly shows the dominance of natural convection over forced convection. As the Darcy number is gradually increased, the effect of natural convection is observed [Figs. 10(a)–10(d)]. Finally, for Da $= \infty$ [Fig. 10(e)], the isotherms resemble the natural convection in a differentially heated square cavity problem as given by de Vahl Davis (1983).

Figures 11(a) and 11(b) show the centerline *u*-velocity profile at the vertical midplane of the cavity for Da $= 10^{-4}$ and Da $= \infty$ respectively. The other parameters are Ri $= 10^{-2} - 10^2$ and Gr $= 10^2 - 10^4$. It is clear that convection currents for Da $= 10^{-4}$ are much less when compared with Da $= \infty$ without porous medium). There is a velocity reversal for Ri $= 10^2$ and Gr $= 10^4$, which is due to the formation of the central vortex [Figs. 9(a) and 9(e)]. Figures 11(c) and 11(d) show the centerline velocity profile at the center of the cavity for Gr $= 10^2$ and Gr $= 10^4$. The plots reveal the dominance of natural or forced convection on the flow. The parameters are Da $= 10^{-4}$ and ∞, and Ri $= 10^{-2}$ and 10^2. The cases of Ri $= 10^{-2}$ and 10^2 are dominated by forced and natural

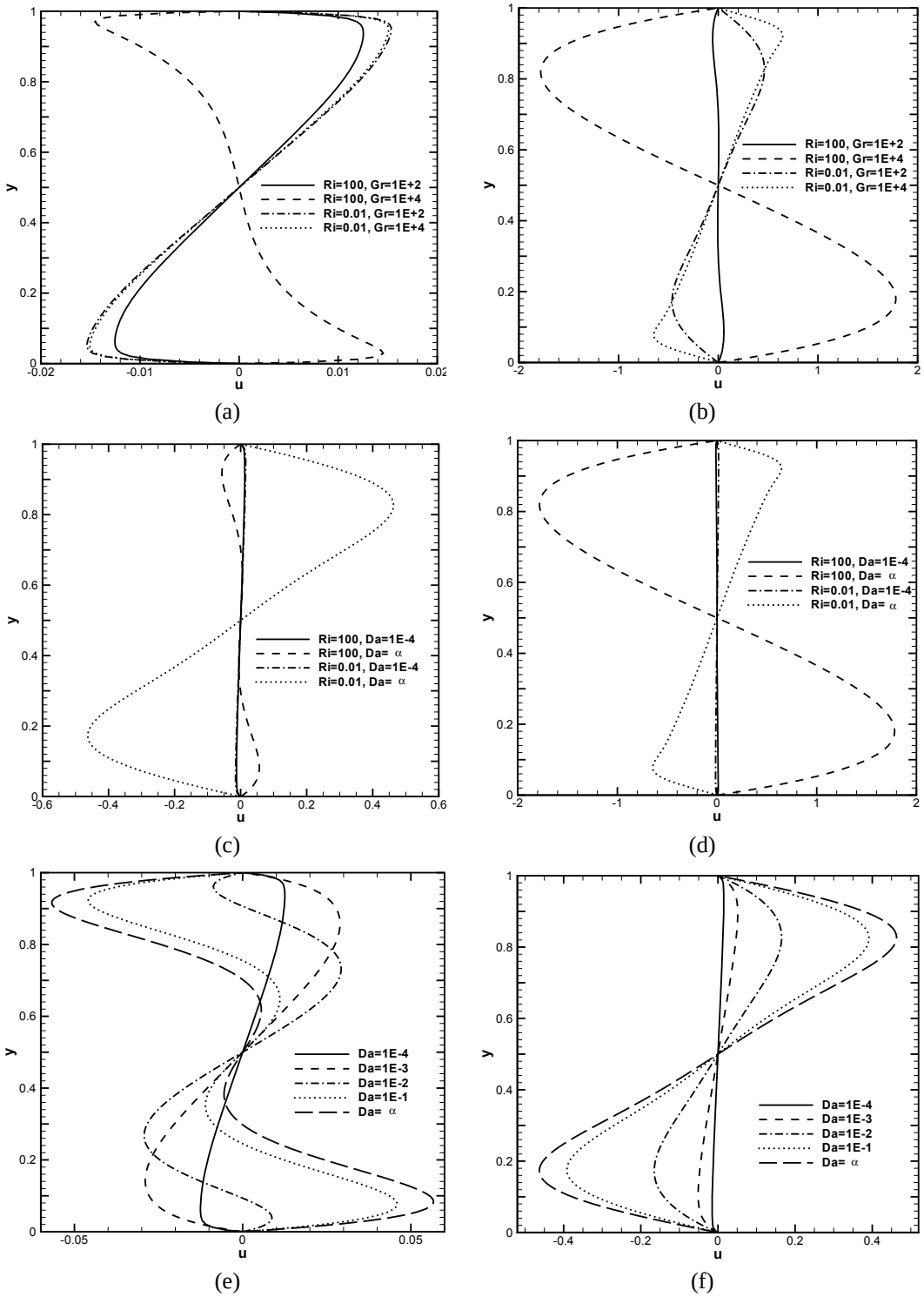

FIG. 11: *u*-velocity along vertical centerline. **(a)** Da $= 10^{-4}$, **(b)** Da $= \infty$, **(c)** Gr $= 10^2$, **(d)** Gr $= 10^4$, **(e)** Ri = 100, Gr = 10^2, and **(f)** Ri = 0.01, Gr = 10^2.

convection, respectively. The opposite nature of the velocity profile is noticed. With the increase in Gr from 10^2 to 10^4, the magnitude of the velocity also reverses for these two cases. Figures 11(e) and 11(f) show the centerline velocity profile at the center of the cavity for $\mathrm{Ri} = 10^2$ and $\mathrm{Ri} = 10^{-2}$, respectively, for $\mathrm{Gr} = 10^2$ and for different Darcy numbers. For $\mathrm{Ri} = 10^2$, the centerline velocities are much less compared with the case for $\mathrm{Ri} = 10^{-2}$. It is observed in Fig. 11(f), that the velocity increases with the increase in Da.

The temperature distribution along the vertical midplane is shown in Fig. 12 for various parameters. It is observed that for low Ri, the bottom wall is hot and the top wall is cold [Fig. 12(a)], and the magnitude depends upon the Gr value. For a high Ri value, the opposite situation is observed [Fig. 12(b)]. The temperature distributions for two Grashof numbers are shown in Figs. 12(c) and 12(d) for various Ri and Da. Similar profile has been observed and the temperature difference increases with increase in Da. The variations of temperature at the center of the cavity along the *y*-direction for $\mathrm{Gr} = 10^2$ and $\mathrm{Ri} = 10^2$ [Fig. 12(e)] and $\mathrm{Ri} = 10^{-2}$ [Fig. 12(f)] with the Darcy number as the parameter. It is clearly demonstrated that for $\mathrm{Ri} = 10^2$ conduction predominates, while for $\mathrm{Ri} = 10^{-2}$ convection takes place.

The local Nusselt number (Nu) distribution along the left wall is presented in Fig. 13. Figures 13(a)–13(b) represent the cases for two Darcy numbers. In the case of low Ri (forced convection), Nu is high near the bottom wall, whereas for high Ri, the opposite is true. For large Da, the magnitude of Nu is also high. In the cases of $\mathrm{Ri} = 10^2$ and $\mathrm{Gr} = 10^2$, conduction with the Nu remains constant at a value of 1. The same is presented for two Gr cases in Figs. 13(c) and 13(d). It is to be observed that for small Ri and large Gr, the Reynolds number is also large. Thus, the local Nu is large in the case of large Gr [Fig. 13(d)]. Figures 13(e) and 13(f) represent the local Nusselt number along the cold wall for $\mathrm{Ri} = 10^2$ and $\mathrm{Ri} = 10^{-2}$ at $\mathrm{Gr} = 10^2$, respectively. It is observed that for $\mathrm{Ri} = 10^2$, the Nusselt number variation is very small and is almost unity for all Darcy numbers. For $\mathrm{Ri} = 10^{-2}$, the Nusselt number is very high at the bottom wall and decreases to approximately unity for all Darcy numbers.

Figure 14(a) shows the average Nusselt number for three Darcy numbers with Gr = 10^2. It is observed, that $\overline{\mathrm{Nu}}$ increases as the Darcy number increases. For a fixed Grashof number, as the Richardson number increases, $\overline{\mathrm{Nu}}$ for all Darcy numbers reaches asymptotically to a same constant value and is approximately equal to 1, which represents strong conduction-dominated flow. But, for a fixed Darcy number, as the Richardson number increases, $\overline{\mathrm{Nu}}$ asymptotically reaches a constant value and then increases as the Grashof number is further increased [Fig. 14(b)].

7. A HEAT TRANSFER CORRELATION

The numerically calculated heat transfer results were correlated for mixed convection in a square cavity and in the presence of porous medium. The average Nusselt number is correlated as a function of the inverse Darcy number [$\mathrm{Da}^{-1} = 1/\mathrm{Da}$], the Richardson number $\mathrm{Ri} = \mathrm{Gr}/\mathrm{Re}^2$, and the Grashof number. The equation is given by

$$\overline{\mathrm{Nu}} = 1 + \frac{0.1289}{\left(1 + \mathrm{Da}^{-1}\right)^{0.1953}} \mathrm{Ri}^{-0.4278} \mathrm{Gr}^{0.3785} \qquad (9)$$

8. CONCLUSIONS

In this study, numerical results of mixed convection heat transfer in a two-dimensional enclosure filled with a fluid-saturated porous medium and subjected to the left wall moving up and the right wall moving down have been presented. The left and the right walls were under cold and hot conditions, respectively. The finite-volume method using the SIMPLE algorithm in a collocated grid arrangement was employed for the present problem. The deferred QUICK scheme was used to minimize the numerical diffusion. Comparisons with previously published work on special cases of the problem were performed and found to be in good agreement. The constant stream function and temperature plots for various parametric conditions were presented and discussed. To vary the Richardson number, the Grashof number was fixed at three levels (i.e., at 10^2, 10^3, and 10^4, and correspondingly, the Reynolds number was varied.

In the case of $\mathrm{Ri} = 10^{-2}$, a single vortex was observed for low Gr. The strength of the vortex increases when Gr is increased. However, in the case of $\mathrm{Ri} = 10^2$, the vortex cell due to the lid-movement and natural convection were present. The effect of natural convection increases when Gr is increased. Also, significant suppression of the convective currents was obtained by the presence of a porous medium. The local Nusselt number distribution along the left wall has a large value at the bottom for low Ri, which is opposite in the case of a large Ri value. With the increase in Ri, the average Nusselt number approaches a value of 1 asymptotically. This signifies that heat transfer is dominated by conduction only.

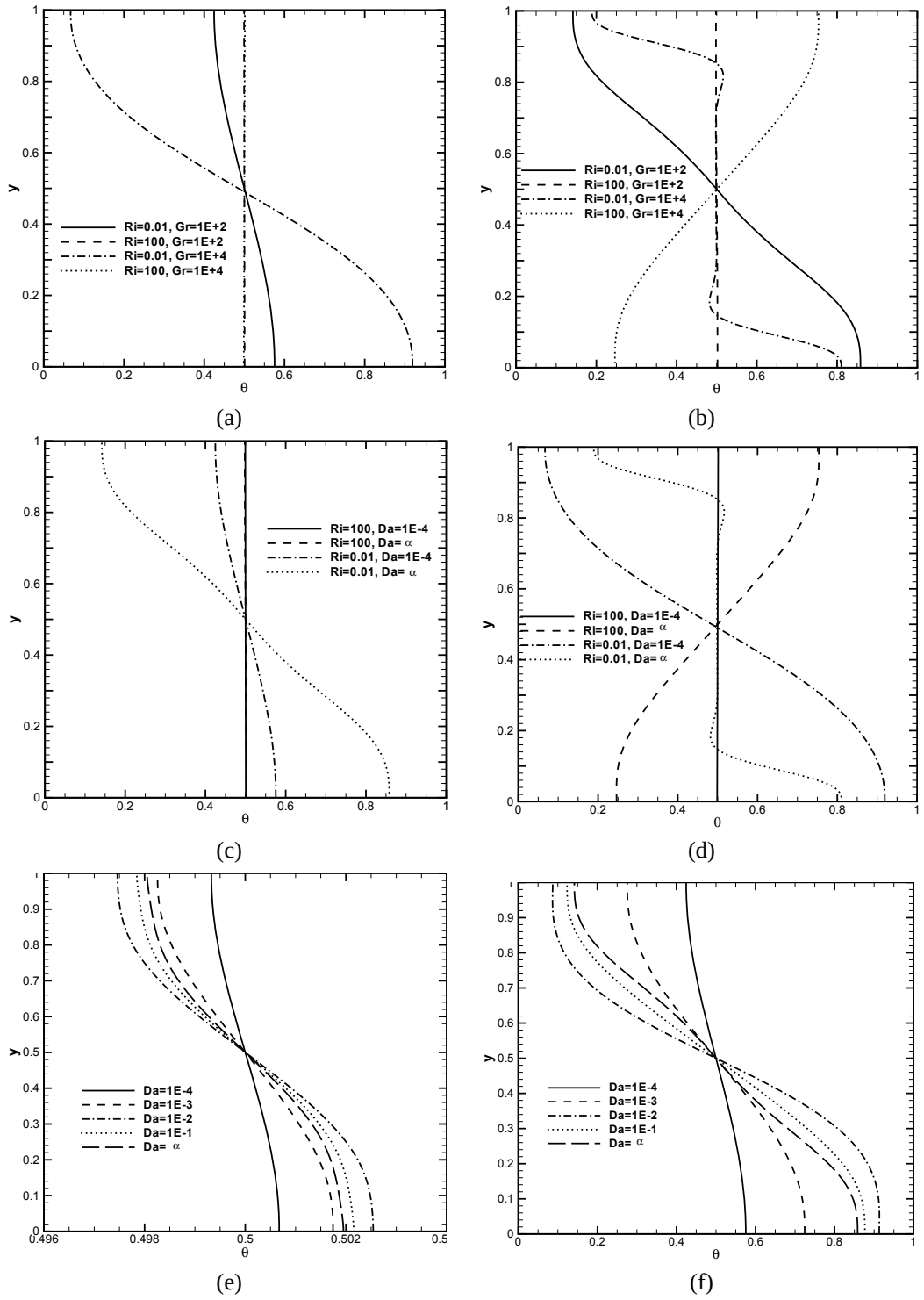

FIG. 12: Variation of temperature along vertical centerline. **(a)** Da $= 10^{-4}$, **(b)** Da $= \infty$, **(c)** Gr $= 10^2$, **(d)** Gr $= 10^4$, **(e)** Ri = 100, Gr = 10^2, and **(f)** Ri = 0.01, Gr = 10^2.

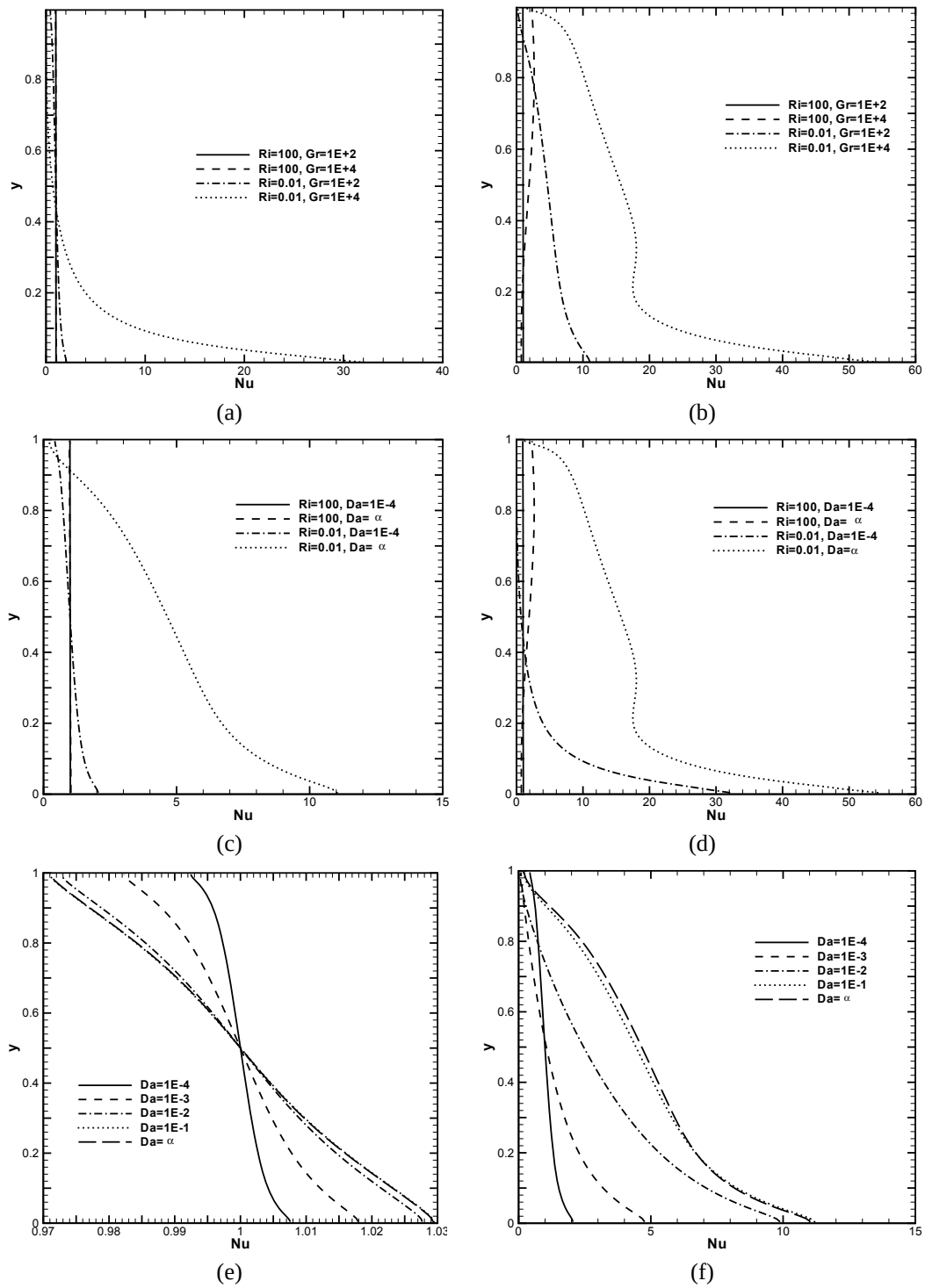

FIG. 13: Variation local Nusselt number (Nu_y) along the right wall. **(a)** $\mathrm{Da} = 10^{-4}$, **(b)** $\mathrm{Da} = \infty$, **(c)** $\mathrm{Gr} = 10^2$, **(d)** $\mathrm{Gr} = 10^4$, **(e)** Ri = 100, Gr = 10^2, and **(f)** Ri = 0.01, Gr = 10^2.

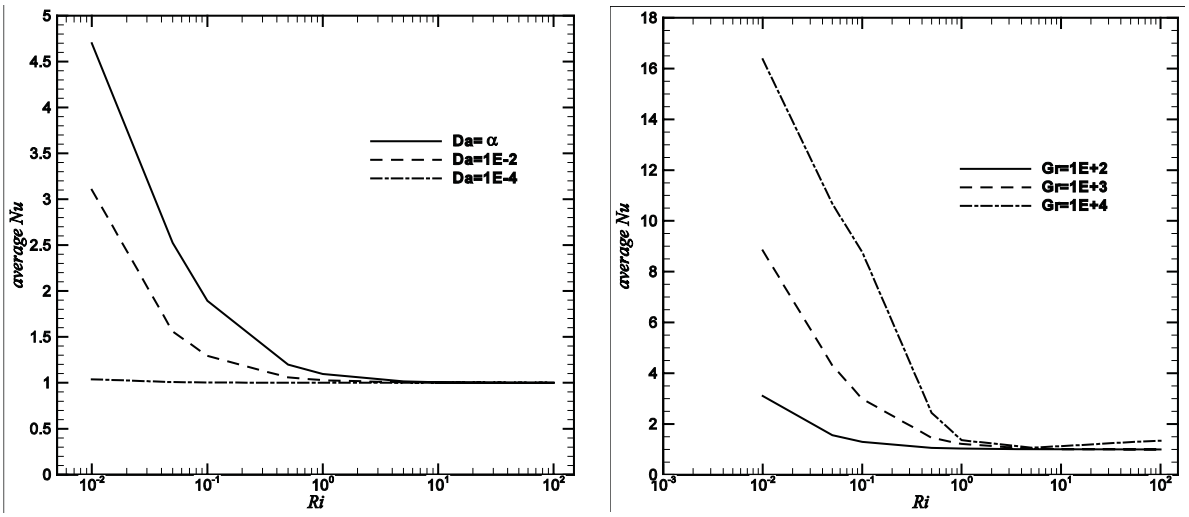

(a) (b)

FIG. 14: Variation of average Nusselt number ($\overline{\mathrm{Nu}}$). **(a)** $\mathrm{Gr} = 10^2$, **(b)** $\mathrm{Da} = 10^{-2}$.

REFERENCES

Blohm, Ch. and Kuhlmann, H. C., The two-sided lid-driven cavity: Experiments on stationary and time-dependent flows, *J. Fluid Mech.*, vol. **450**, pp. 67–95, 2002.

Cheng, P., Heat transfer in geothermal systems, *Adv. Heat Transfer*, vol. **4**, pp. 1–105, 1978.

de Vahl Davis, G., Natural convection of air in a square cavity: A bench mark solution, *Int. J. Numer. Methods Fluids*, vol. **3**, pp. 249–264, 1983.

Hayase, T., Humphrey, J. A. C., and Greif, R., A consistently formulated QUICK scheme for fast and stable convergence using finite-volume iterative calculation procedures. *J. Comput. Phys.*, vol. **98**, pp. 108–118, 1992.

Hsieh, J. C., Chen, T. S., and Armaly, B. F., Nonsimilarity solutions for mixed convection from vertical surface in a porous medium-variable surface temperature or heat flux, *Int. J. Heat Mass Transfer*, vol. **36**, pp. 1485–1493, 1993.

Ideriah, F. J. K., Prediction of turbulent cavity flow driven by buoyancy and shear, *J. Mech. Eng. Sci.*, vol. **22**, pp. 287–295, 1980.

Iwatsu, R., Hyun, J. M., and Kuwahara, K., Mixed convection in a driven cavity with a stable vertical temperature gradient, *Int. J. Heat Mass Transfer*, vol. **36**, pp. 1601–1608, 1993.

Khanafer, K. M. and Chamkha, A. J., Mixed convection flow in a lid-driven enclosure filled with a fluid-saturated porous medium, *Int. J. Heat Mass Transfer*, vol. **42**, pp. 2465–2481, 1999.

Kuhlmann, H. C., Wanschura, M., and Rath, H. J., Flow in two-sided lid-driven cavities: Non-uniqueness, instabilities, and cellular structures, *J. Fluid Mech.*, vol. **336**, pp. 267–299, 1997.

Lai, F. C. and Kulacki, F. A., Non-Darcy mixed convection along a vertical wall in a saturated porous media, *J. Heat Transfer*, vol. **113**, pp. 252–255, 1991.

Lauriat, G. and Prasad, V., Non-Darcian effects on natural convection in a vertical porous enclosure, *Int. J. Heat Mass Transfer*, vol. **32**, pp. 2135–2148, 1989.

Nithiarasu, P., Seetharamu, K. N., and Sundararajan, T., Natural convective heat transfer in a fluid saturated variable porosity medium, *Int. J. Heat Mass Transfer*, vol. **40**, pp. 3955–3967, 1997.

Nithiarasu, P., Seetharamu, K. N., and Sundararajan, T., Effect of porosity on natural convective heat transfer in a fluid saturated porous medium, *Int. J. Heat Fluid Flow*, vol. **19**, pp. 56–58, 1998.

Oztop, H. F. and Dagtekin, I., Mixed convection in two-sided lid-driven differentially heated square cavity, *Int. J. Heat Mass Transfer*, vol. **47**, pp. 1761–1769, 2004.

Patankar, S. V., *Numerical Heat Transfer and Fluid Flow*, Hemisphere, New York, 1980.

Pilkington, L. A. B., Review lecture: The float glass process, *Proc. R. Soc. London, Ser. A*, vol. **314**, pp. 1–25, 1969.

Rhie, C. M. and Chow, W. L., A numerical study of the turbulent flow past an isolated airfoil with trailing edge separation, *AIAA J.*, vol. **21**, pp. 1525–1532, 1983.

Vafai, K. and Tien, C. L., Boundary and inertia effects on flow and heat transfer in porous media, *Int. J. Heat Mass Transfer*, vol. **24**, pp. 195–203, 1981.

Van Doormaal, J. P. and Raithby, G. D., Enhancements of the SIMPLE method for predicting incompressible fluid flows, *Numer. Heat Transfer*, vol. **7**, pp. 147–163, 1984.

Versteeg, H. K. and Malalasekera, W., *An Introduction to Computational Fluid Dynamics. The Finite Volume Method*, Longman, London, 1996.

Vishnuvardhanarao, E. and Das, M. K., Laminar mixed convection in a parallel two-sided lid-driven differentially heated square cavity filled with a fluid-saturated porous medium, *Numer. Heat Transfer*, vol. **53**, pp. 88–110, 2008.

Journal of Porous Media 13(12), 1073–1085 (2010)

LAMINAR AND TURBULENT FLOW THROUGH AN ARRAY OF CYLINDERS

J. Gunnar I. Hellström,[1,] P. Jonas P. Jonsson,[1,2] & T. Staffan Lundström[1]*

[1]*Division of Fluid Mechanics, Luleå University of Technology, SE-971 87 Luleå, Sweden*

[2]*Epsilon High Tech AB, Göteborg SE-417 56, Sweden*

[*]Address all correspondence to J. Gunnar I. Hellström E-mail: gunnar.hellstrom@ltu.se

Original Manuscript Submitted: 3/2/2009; Final Draft Received: 7/13/2009

When modeling fluid flow through porous media it is necessary to know when to take inertia effects into account, as well as when to switch to a turbulent description of the flow. From an engineering point of view, the problem is often solved with the empirically derived Ergun equation or a recently upgraded version by Nemec and Levec [Chem. Eng. Sci., vol. 60, pp. 6947–6957, 2005]. The drawback with this approach is, however, that the mechanisms for the transitions between the three states of flow are not revealed and time-consuming experiments have to be performed. In order to increase knowledge of the detailed flow, numerical studies of flow through arrays of quadratically packed cylinders at a variety of Re values were carried out. One result is that the laminar and turbulent approaches used both mimic experimental results for low Re, while for higher Re only the turbulent approach resembles the empirically derived equations. The deviation from Darcy's law for different porosities of the array can be defined by usage of Re based on the hydraulic radius and the average interstitial velocity. However, to find a common Re when turbulence need to be accounted for, another Re based solely on the averaged interstitial velocity and the diameter of the cylinders was used. It was found that at low Re the laminar and turbulent setups give practically the same velocity fields, while the turbulent dissipation at higher Re results in larger circulation zones and weaker jets.

KEY WORDS: *porous media, turbulence, computation, fluid mechanics, hydrodynamics*

1. INTRODUCTION

Flow through porous media is important in many technical areas, including ground water flow, flow through embankment dams, paper-making, composites manufacturing, filtering and drying, and sintering of iron ore pellets. In some of these applications the characteristics of flow are unknown, while for others higher demands on the environment, security, and process efficiency imply that the flow must be studied in more detail. In the present case we want to study the forces on individual particles in connection to flow through embankment dams. Therefore we need to know when inertia effects should be accounted for and when turbulence comes into play. In this context definition of the Reynolds number (Re) becomes important. Therefore we carried out a computational fluid dynamics (CFD)–based micromechanical investigation of flow through porous media ranging from creeping, strictly Darcian, to fully turbulent.

Creeping flow of a Newtonian fluid through porous media follows Darcy's law on a global scale according to

$$v_i = -\frac{K_{ij}}{\mu} p_{,j} \tag{1}$$

in a general form and

$$\frac{K}{\mu}\frac{\Delta p}{L} = \frac{Q}{A} \tag{2}$$

in one-dimensional form. In these equations v_i is the superficial velocity vector, K_{ij} the permeability tensor, μ the dynamic viscosity of the fluid, p pressure, Q flow rate through an area A, and Δp the pressure drop over a length

1091–028X/10/$35.00

L in the streamwise direction. The permeability is set by the geometry of the porous media, and many expressions have been derived for this relationship. For flow perpendicular to an array of cylinders, the following equation is strictly valid for low porosities ϕ and the error is less than 10% for $\phi = 0.65$ (Gebart, 1992):

$$K_\perp = C\left(\sqrt{\frac{1-\phi_{\min}}{1-\phi}}-1\right)^{5/2} R^2, \tag{3}$$

where C and $\phi_{\min}$ are determined from the geometrical arrangement (such as quadratic or hexagonal arrangement). When the flow in the pores is fully or partly turbulent, a nonlinear term is often introduced for flow of a Newtonian fluid to form the Forchheimer equation:

$$\frac{K}{\mu}\frac{\Delta p}{L} = \frac{Q}{A} + b\left(\frac{Q}{A}\right)^m, \tag{4}$$

where b is a property of the porous media, and m, in this case, is a measure of the influence of fluid turbulence (Forchheimer, 1901; Papathanasiou et al., 2001). As a special case of Eq. (4), Ergun derived the following expression:

$$\frac{\Delta p_F}{L} g = 150\frac{(1-\phi)^2}{\phi^3}\frac{\mu\frac{Q}{A}}{D_p^2} + 1.75\frac{(1-\phi)}{\phi^3}\frac{\rho\left(\frac{Q}{A}\right)^2}{D_p}, \tag{5}$$

by fittings to the experimental data (Ergun, 1952). In this equation p_F is the pressure represented as a force, g is the gravitational constant, D_p the effective diameter of particles, and ρ the density of the fluid. In between the creeping flow region and the turbulent one, laminar inertia gives a substantial contribution to the resistance to flow and experiments have indicated that it is possible to use Eqs. (4) and (5) in this case as well. Hence, measurements of averaged quantities have thus shown that the transition from laminar to turbulent flow is smooth. In accordance with this observation, Dybbs and Edwards (1984) conclude, from their experimental visualizations of flow around cylinders arranged in an array, that there is a smooth transition from an unsteady laminar flow regime to a highly unsteady and chaotic flow regime. They also state that further investigations on the nature of these regimes are needed in order to give insight into velocity distributions and various transport phenomena inside porous media. Results in Seguin et al. (1998) indicate that the local transition within porous media takes place at various global Re, since the local velocity as well as the characteristic length scales vary as a function of spatial coordinate; hence laminar and turbulent flow may coexist. This certainly affects the forces on individual particles within a porous media. Another result in Seguin et al. (1998) is that when increasing Re the velocity gradient starts to fluctuate at an increasing rate until a certain Re where this rate is stabilized.

Returning to the global description of the flow, the Ergun equation has shown best agreement with a bed of randomly distributed spheres and is therefore not optimal for all geometries. Instead the following expression is proposed by Nemec and Levec (2005):

$$\frac{\Delta p}{L}\frac{1}{\rho g} = \Psi = A^*\frac{\mathrm{Re}^*}{\mathrm{Ga}^*} + B^*\frac{\mathrm{Re}^{*2}}{\mathrm{Ga}^*}, \tag{6}$$

where Re^* and Ga^* are defined as

$$\mathrm{Re}^* = \frac{\rho\varphi D_p U}{\mu(1-\varepsilon)} \tag{7}$$

and

$$\mathrm{Ga}^* = \frac{\rho^2 g\varphi^3 D_p^3\varepsilon^3}{\mu^2(1-\varepsilon)^3} \tag{8}$$

and where the material-dependent constants A^* and B^* range between 180–280 and 1.9–4.6, respectively. This reveals that additional variables besides ϕ and D_p need to be introduced in order to fully describe the relation between the detailed geometry and the resistance to flow through porous media. Another common way to globally relate pressure to flow rate is by the Blake-type friction factor, defined as

$$f' = \frac{\Delta p}{L}\frac{D_p}{\rho\left(\frac{Q}{A}\right)^2}\frac{\phi^3}{1-\phi}. \tag{9}$$

Introducing this relationship into the Ergun Eq. (5) yields

$$f' = 1.75 + \frac{150}{\mathrm{Re}'}, \tag{10}$$

which resembles experimental data and where the modified Re is defined as

$$\mathrm{Re}' = \frac{\rho D_p\frac{Q}{A}}{\mu}\frac{1}{1-\phi}. \tag{11}$$

This definition of Re stems from Ergun (1952), with the hydraulic diameter and the real average velocity set as the characteristic length L and the characteristic velocity U, respectively, and where Re, in general terms, is expressed as

$$\mathrm{Re} = \frac{UL}{\nu}, \tag{12}$$

where ν is the kinematic viscosity. We mainly use Re' throughout this paper, but as pointed out in Comiti (2000), this is just one way of defining Re for porous media. For the characteristic length, typical size of the pores, typical size of the particles, and the square root of the permeability of the porous media were also employed, while the characteristic velocity is often set as the superficial velocity.

The validity of the global equations presented above has been thoroughly investigated. Fand et al. (1987), for instance, performed an experimental study of flow through simple and complex porous media with the conclusion that Darcy's law is valid for Re, based on the superficial velocity and the diameter of the sphere Re^S below 2.3. Inertia needs to be considered when $5 < \mathrm{Re}^S < 80$, and turbulence is the dominating mechanism contributing to loss when Re^S is above 120. This range was extended in an experimental study on a pore scale by Lesage et al. (2004), who concluded that the flow is laminar for Re^S below 110 and turbulent for Re^S above 280, which is also in agreement with additional results presented in Hlushkou and Tallarek (2006). The experiments performed in Seguin et al. (1998) indicate that the flow is laminar until Re, based on average pore space and average pore velocity Re^d, reaches 180, and the fully turbulent region starts when Re^d becomes equal to 900. Hence similar results to those presented above are obtained. McFarland and Dranchuk (1976) discovered that transition to turbulent flow took place for Re from 0.241 to 4.56, where Re is based on the Darcy superficial velocity and a length parameter equal to the product of the permeability and an inertial resistance coefficient, a definition leading to the relatively small values for the transition. Yet another way of defining Re was used by Venkataraman et al. (1998), who related Re to the square root of the permeability Re^K. Thus there are several ways to define Re in a porous media, and a variety of critical Re for inertia and turbulence have been proposed. The latter is confirmed by Bear (1960), who state that there is an uncertainty in the critical Re for inertia by a factor of 750.

In order to understand porous media flow, a number of numerical methods have been applied as outlined by Ziólkowska and Ziólkowski (1988). The increases in computer capacity in recent decades have facilitated even more detailed studies, including the one presented here. In the numerical investigation by Koch and Ladd (1997), drag is calculated for some arrays of cylinders. One result is that the magnitude of drag per unit length on cylinders in a square array at moderate Re is strongly dependent on the orientation of the pressure gradient. Another is that in random arrays, drag makes a transition from quadratic to a linear Re dependence at Re^D, based on the diameter of the cylinders and the average interstitial velocity between 2 and 5. Ghaddar (1995) also considers flow through a regular array of cylinders, showing that the flow becomes unsteady for Re' greater than 150. However, Pedras and de Lemos (2003) present a strategy for computations of turbulent simulations in porous media using a low-Re *k*-ε model, which shows good agreement with published data incorporating a steady flow assumption.

Lattice-Boltzmann simulations have also been performed in order to bridge the gap between Stokes flow and moderate Re simulations of flow in porous media (Hill et al., 2001). In Beetstra et al. (2007) this technique was applied for a variety of solid volume fractions and Reynolds numbers up to Re^S= 1000.

The short literature survey presented above does not clarify which Re to use when defining when inertia becomes important and the onset of turbulence. Furthermore it is not apparent how inertia and turbulent flow are composed in a porous media, although the experiments by Dybbs and Edwards (1984) and Seguin et al. (1998) are a very good starting point. In this paper we therefore perform a CFD-based micromechanical investigation ranging from creeping, strictly Darcian flow to fully turbulent, full Navier-Stokes equation flow in order to investigate the limitations of the equations for flow through a quadratic array of cylinders packed at different solid fractions. We perform the simulations with very fine meshes (high accuracy) and with a laminar flow setup (creeping to turbulent Re), as well as with a two-equation turbulence model (creeping to turbulent Re). This enables us to study the flow field in detail and to do simulations at much higher Reynolds numbers than practically possible with the Lattice-Boltzmann technique (Beetstra et al., 2007). The outcomes from laminar and turbulent flow setups are then compared to each other and to results from the literature.

2. GOVERNING EQUATIONS

To be able to capture the complete flow field as a function of Re, the Navier-Stokes equations are applied. To start with the equations are set up for laminar flow of a Newtonian and incompressible fluid according to

$$u_{i,t} + u_j u_{i,j} = -\frac{1}{\rho} p_{,i} + \nu u_{i,jj} \tag{13}$$

and

$$u_{i,i} = 0. \tag{14}$$

Then at a second stage the flow is allowed to be turbulent by applying Reynolds averaging by decomposing the total velocity $\tilde{u}$ into a mean U and fluctuation component u, i.e., $\tilde{u} = U + u$ where $U \equiv \bar{\tilde{u}}$, resulting in the following equations:

$$U_{i,t} + U_j U_{i,j} = -\frac{1}{\rho} p_{,i} + \nu U_{i,jj} - \left(\overline{u_j u_i}\right)_{,j} \qquad (15)$$

and

$$U_{i,i} = 0. \qquad (16)$$

Here ν is the kinematic viscosity and $\overline{u_i u_j}$ are the Reynolds stresses. These equations represent the mean flow characteristics where turbulent effects are modelled via the Reynolds stresses in order to obtain closure. Since focus is set on flow around a number of periodically arranged cylinders having curved surfaces, the shear-stress-transport (SST) turbulence model is applied (Menter, 1993) because of its good behavior when considering adverse pressure gradient flows and separating flow. In the SST model the best ingredients from the *k*-ε and the *k*-ω models are combined via a blending factor. This factor activates the *k*-ω model in the near-wall region and the *k*-ε model in the bulk, showing that the shift from the *k*-ω to the *k*-ε formulation takes place in the logarithmic part of the boundary layer. The model is based on the assumption that the principal shear stress is proportional to the turbulent kinetic energy, which is introduced to the definition of the eddy viscosity, the so-called Bradshaw's assumption. The mathematical formulations thus develop into

$$\frac{D\rho k}{Dt} = S_{ij}\frac{\partial u_i}{\partial x_j} - \beta^* \rho\omega k + \frac{\partial}{\partial x_j}\left[\left(\mu + \sigma_k \mu_T\right)\frac{\partial k}{\partial x_j}\right] \qquad (17)$$

and

$$\frac{D\rho\omega}{Dt} = \frac{\gamma}{\nu_T} S_{ij}\frac{\partial u_i}{\partial x_j} - \beta\omega^2 + \frac{\partial}{\partial x_j}\left[\left(\mu + \sigma_\omega \mu_T\right)\frac{\partial \omega}{\partial x_j}\right] + 2\rho\left(1 - F_1\right)\sigma_{\omega 2}\frac{1}{\omega}\frac{\partial k}{\partial x_j}\frac{\partial \omega}{\partial x_j}, \qquad (18)$$

where *k* is the turbulent kinetic energy, S_{ij} the turbulent stress tensor, ω the turbulent frequency, μ_T the turbulent dynamic viscosity, ν_T the turbulent kinematic viscosity, and β^*, σ_k, γ, σ_ω, F_1, and $\sigma_{\omega 2}$ are constants (Menter, 1993).

The laminar and turbulent setups are *both* used to calculate the flow through a porous media at a variety of Reynolds numbers, from fractions of 1 up to values near 10,000. Obviously the laminar and turbulent simulations are thus applied in areas of Reynolds numbers where they are usually not valid. However, it will turn out that a number of interesting results are generated by this approach.

3. GEOMETRY AND NUMERICAL VERIFICATION

The geometry chosen for this study is an array of quadratically packed infinite long cylinders for which a unit-cell approach is applied, where for each porosity two unit cells are defined (see Fig. 1) that are divided into finite volumes with the aid of ANSYS ICEM CFD 10.0 Hexa. In order to get a high-quality design of the numerical grid, a block structure is created that is projected onto the respective unit cell. The eight blocks used in this procedure are arranged so that the main flow features in the unit cells can be resolved. For laminar flow it has previously been shown that the quality of the grid is by all means good enough, yielding an error of less than 0.3 per mille when using 370,000 nodes (Hellström and Lundström, 2006). The flow field is solved with the commercial software ANSYS CFX 10.0, and the computational domain is parallelized with the MeTis partitioning method and simulated on homogenous Windows and LINUX clusters. For the Windows part of the simulations the MPICH-1.2.5 message-passing libraries (MPI) are applied, and for the LINUX part a HP-MPI-2.1 routine is chosen (see Hellström et al., 2006). For the turbulent simulations measures are taken to keep the *y*-plus value low enough. This is a dimensionless distance from the wall used to provide information on the near wall resolution. To exemplify, when Re′ is equal to 2000 the maximum *y*-plus is 1.3. This is within the limits of the recommendations in the CFX-manual CFX® (2005), stating that the *y*-plus value should be lower than 2, and the requirements the European Research Community on Flow, Turbulence and Combustion (ERCOFTAC) Best practice Guidelines (2000), where the conditions are that *y*-plus should be below 4 and close to unity.

The boundary conditions of the unit cell are defined as follows: The top and the bottom part are symmetry planes,

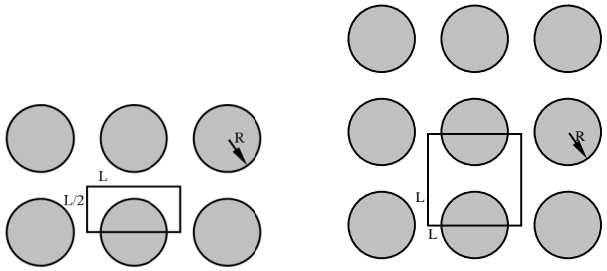

FIG. 1: Schematic sketch of the computational domains. To the left is the unit cell for the steady simulations and to the right the unit cell for the unsteady simulations.

the cylinder wall is assumed to be smooth with a no-slip condition, and the left- and right-hand sides are periodic domain interfaces, all in all, representing the repeatable structure of the array. In order to drive the flow, a momentum source is defined in a subdomain. The advection scheme used to solve the continuity and momentum equations is chosen to be strictly second-order accurate by setting the specified blend factor equal to one in CFX-Pre. The simulations are furthermore assumed to be well converged when the root-mean-square (RMS) residuals have dropped 5–6 orders of magnitude and when the maximum residuals are less than 1.5 orders of magnitude above the RMS residuals.

For the unsteady calculations a second-order backward Euler scheme is applied, and the time step is selected so that the Courant number is between 0 and 5, where the Courant number is defined as the fluid velocity times the timestep divided by the mesh size. To discern the unsteady behavior of the simulations, a number of monitor points were introduced that recorded pressure at nine locations and logged the mass flow at the domain interfaces. Most turbulent simulations were performed with the SST model for reasons already presented, and other turbulence models tested gave similar results and thus indicate the same behavior but they need more central processing unit (CPU) time.

In order to decrease the usage of CPUs, most simulations were initially based on former runs, in particular, when appropriate each turbulent simulation was based on its laminar counterpart, that is, the laminar simulation with the same pressure gradient. For the laminar simulations as well as the turbulent simulations with high pressure gradients, there is no initial guess of the velocity field. Initial conditions for the turbulent kinetic energy and the eddy frequency were 0.03 m^2/s^2 and 300 Hz, respectively, based on experience from former simulations and post-processing. For the periodic domain interface boundaries the turbulence option is set as a conservative interface flux. To ensure that the selected values of the turbulent parameters are relevant for the problem studied, a perturbation analysis was carried out. The variations introduced only weakly influence the results, indicating that the solutions obtained are stable in this context.

At higher Re the laminar simulations were performed by an unsteady approach, since the steady simulations indicated problems like oscillating residuals and unstable values of the mass flow. This is in agreement with the results in Ghaddar (1995) and Seguin et al. (1998), who got indications of an oscillating numerical solution and experimentally derived the velocity gradient as described in the Introduction. For the turbulent setup this behavior was not observed, which also follows the experimental results in Seguin et al. (1998) showing that the fluctuation rate of the velocity gradient stabilizes at a certain Re. Hence, all turbulent simulations were performed with steady flow approach.

4. REYNOLDS NUMBERS FOR A QUADRATIC ARRAY OF CYLINDERS

As stated in the Introduction there are several ways to define Re, and here we will derive and compare a couple of those for a quadratic arrangement of cylinders. Comparisons between results from the simulations are critically dependent on which Re is used. Thus let

$$U = U_a = \frac{Q}{A\phi} = \frac{U_0}{\phi} \tag{19a}$$

and

$$L = D_h = \frac{V_p}{A_s} = \frac{D_p\phi}{4\,(1-\phi)}, \tag{19b}$$

where U_a is the average velocity within the array, U_0 the porous media superficial velocity, D_h the hydraulic diameter of the array, V_p the volume of the pore space within the array, A_s the surface of the solid phase within the array, and D_p is the diameter of the cylinders. The resulting Re then becomes

$$\mathrm{Re}^{Dh} = \frac{D_p U_0}{\nu 4\,(1-\phi)} = \frac{\mathrm{Re}'}{4}. \tag{20}$$

The interpretation is that when ϕ increases, an increase of the scale of the pores combined with an overall decrease in velocity results in an Re that *increases*, with ϕ keeping the flow rate constant (see Fig. 2). Another way of defining Re is to set the typical length scale to the diameter of the cylinders while using the same definition of the velocity to form

$$\mathrm{Re}^{D} = \frac{U_0 D_p}{\nu\phi}. \tag{21}$$

This Re is not coupled to the detailed geometry of the array and has been termed the interstitial Re (Comiti et al., 2000). For a given size of the cylinders it relates Re to the actual averaged velocity within the array. Hence Re^D decreases with porosity (see Fig. 2). A third possible way to define Re is to find a typical length scale in the pore space within the array. One such scale is the distance between the fibers, *d*. In this gap a corresponding velocity U_d may

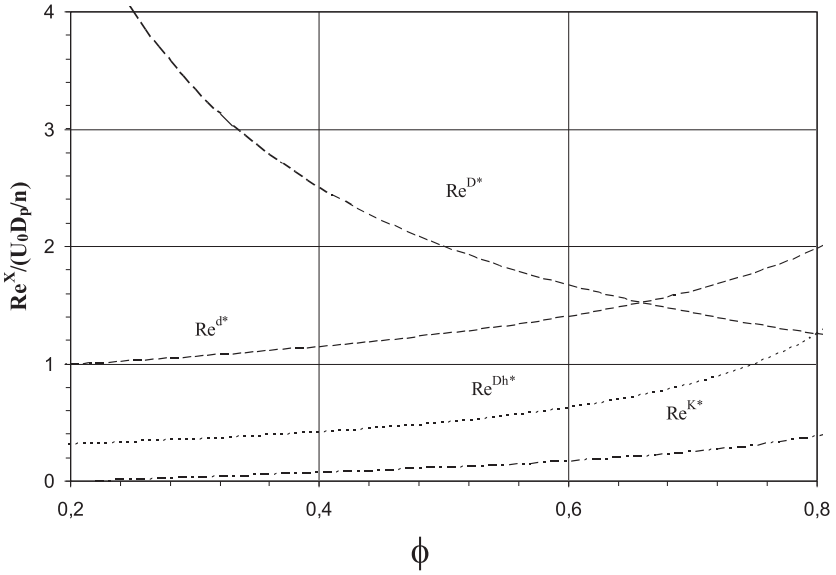

FIG. 2: Comparison between different Reynolds number formulations for a variety of porosities

be identified. These quantities are usually not known, but after some algebra, the following Re materializes:

$$\mathrm{Re}^d = \frac{U_0 D_p}{\nu} \frac{\sqrt{\pi}}{2\sqrt{1-\phi}}. \tag{22}$$

As for Re^{Dh}, Re^d *increases* with porosity (see Fig. 2). The typical length scale can also be linked to the permeability of the array, hence

$$\mathrm{Re}^K = \frac{U_0 \sqrt{K_q}}{\nu\phi}, \tag{23}$$

where

$$K_q = \frac{4}{9\pi\sqrt{2}} \left(\sqrt{\frac{\pi/4}{1-\phi}} - 1 \right)^{5/2} D_p^2. \tag{24}$$

In this case also, Re increases with porosity; however, the magnitude of it is much lower than for the other definitions of Re for the porosities studied (see Fig. 2). In this context it is also of interest to notice that Re^S, defined in the Introduction, is independent of porosity and equal to 1 for all $\phi > 0$ in Fig. 2.

5. RESULTS AND DISCUSSION

For the simulation carried out with the full Navier–Stokes equations and a laminar flow assumption, there is a drop in permeability at $\mathrm{Re}' \approx 10$ (see Fig. 3). As Re' is increased, the curve for the apparent permeability then makes a smooth bend and seems to level out. In reality and at the high end of this curve it is likely that large-scale eddies are generated that strongly affect the flow field. Before presenting results from the simulations with a turbulent flow assumption, let us study the flow field calculated for various setups with the laminar flow hypothesis.

As Re' is increased a sort of jet is formed, transporting most of the fluid through the porous medium, which is in agreement with measurements of velocity profiles in Johns et al. (2000). Also, the stagnation point on the left-hand side of the cylinder climbs "uphill" toward the top of the cylinder and the corresponding recirculation zone becomes smaller and seemingly more chaotic (see Fig. 4). At very low Re' the circulation generated acts on a larger scale, while as Re' increases the structure splits into several zones and the contribution from the circulation is taken as a whole, as the overall resistance to flow becomes more significant (see Fig. 4). The fact that the circulation zone becomes smaller at even higher Re' may explain the result that the apparent permeability levels out (cf. Figs. 3 and 4).

The laminar flow simulations may also be compared to experiment on a global scale by using the empirically derived and previously defined Blake-type friction factor, i.e., Eqs. (9) and (10). The simulated values correspond very well to the Ergun equation and its modified version

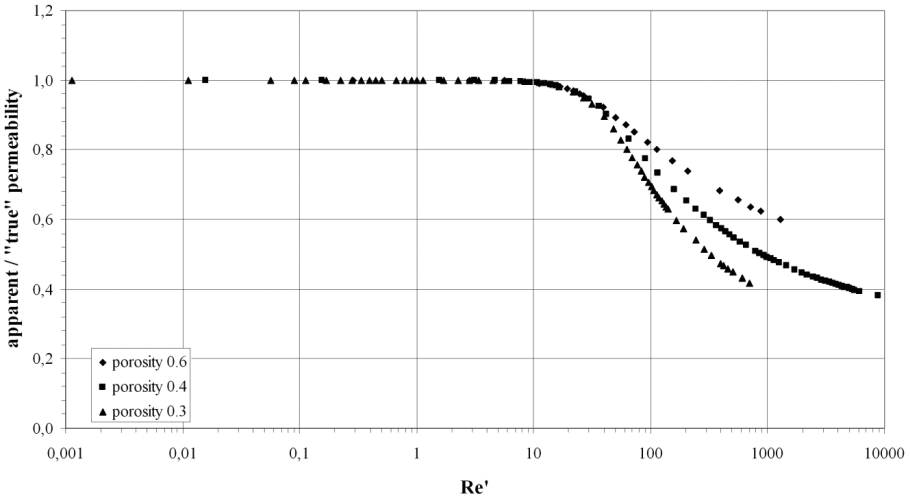

FIG. 3: Apparent permeability divided by true permeability for the three porosities studied here, 0.3, 0.4, and 0.6

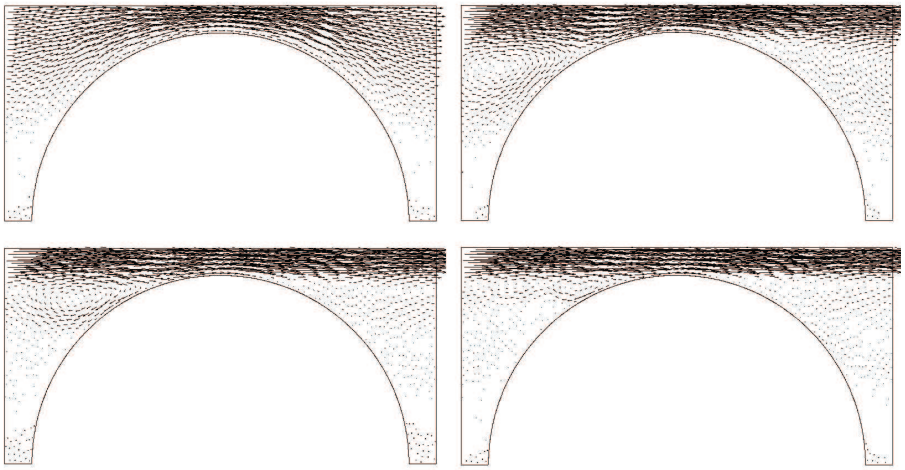

FIG. 4: Vectors representing the velocity for the laminar configuration with different Re' for 0.4 porosity: **(top left)** $\mathrm{Re}' = 0.02$, **(top right)** $\mathrm{Re}' = 200$, **(bottom left)** $\mathrm{Re}' = 1000$, and **(bottom right)** $\mathrm{Re}' = 4000$

until $\mathrm{Re}' \approx 30$, but as Re' is allowed to increase further the simulated results start to deviate from this equation (see Fig. 5). To exemplify, the difference between the case of porosity 0.6 and the Ergun equation is about 20% at $\mathrm{Re}' = 30$. This indicates that mechanisms other than inertia effects such as turbulence become important when Re' is larger than about 30.

When comparing the results from the turbulent simulations (denoted as white symbols in Fig. 6) with the laminar equivalents (denoted with black symbols in Fig. 6), it is shown that the SST formulation captures the main feature of the flow field even at very low Re' values. Increasing Re' further implies that the turbulent simulations give lower apparent permeability values than the laminar ones. This is expected and there is no sign of a rapid transition, as the one in the pipe flow which here is in conformity with the results of Seguin et al. (1998), although the mechanism differs slightly. In Seguin et al. (1998) the smooth transition is attributed to the transition appearing at different Reynolds numbers within different pores, while the simulations presented here indicate rather that the smooth transition is a result of an interplay between inertia and turbulence within a single pore. A comparison of the results at three solid fractions yields that the devia-

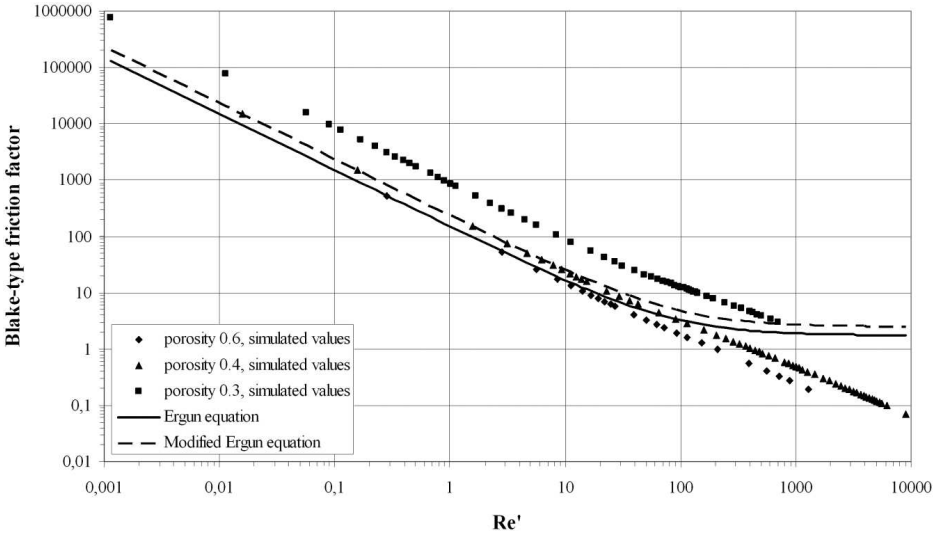

FIG. 5: The Blake-type friction factor calculated for the simulations as well as the Ergun equation and the modification by Nemec and Levec for the different porosities

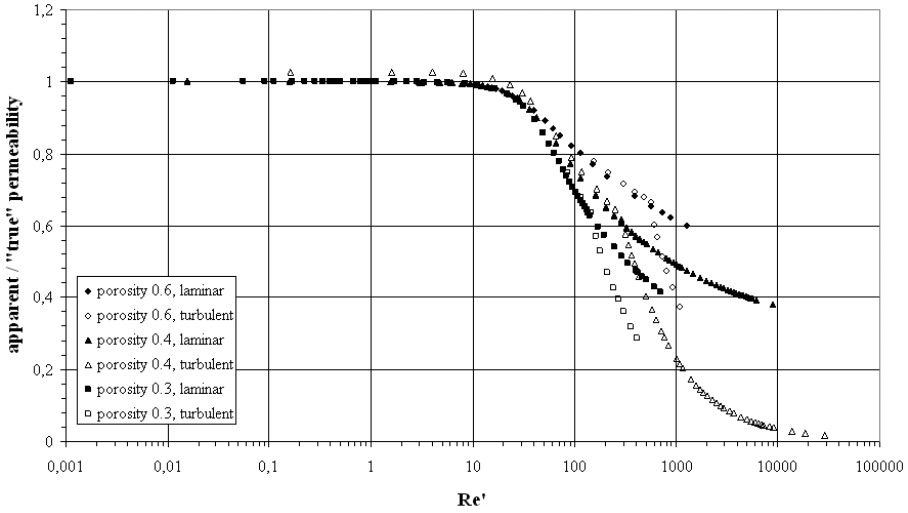

FIG. 6: The apparent permeability divided by the true permeability for the three porosities (0.3, 0.4, and 0.6), values for both the laminar and the turbulent case

tion between the laminar and turbulent setups takes place for Re' ranging from 100 to 600, depending on the porosity. This fact stresses that Re' denotes the onset of inertia while another Re yielding the onset of turbulence has to be defined.

When comparing the simulated values with the Ergun and the modified Ergun equation, the discrepancy for $\mathrm{Re}' > 30$ is now reduced (cf. Figs. 5 and 7). This confirms that turbulence needs to be considered at Re' larger than 100–600. However, this very large range can be considerably reduced by plotting the results as a function of Re^D instead, which is directly related to the average velocity within the porous media (see Figs. 8 and 9). The deviation between the laminar and turbulent simulations now takes place at practically the same Re^D ($\mathrm{Re}^D = 300$), regardless of the porosity.

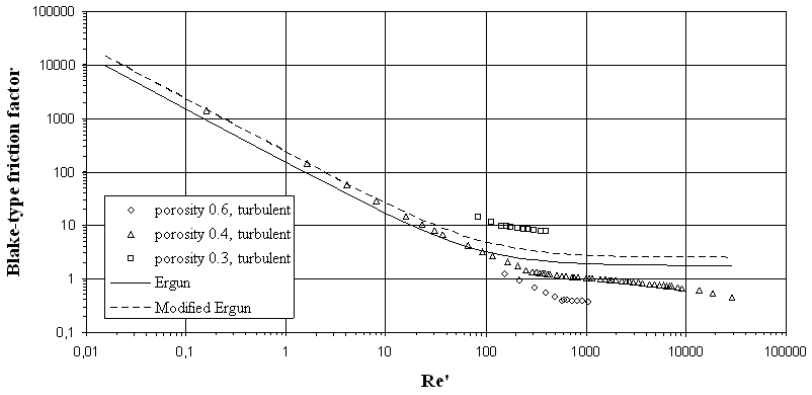

FIG. 7: The Blake-type friction factor for the Ergun and the modified Ergun equation as well as for the simulated values, only the turbulent case

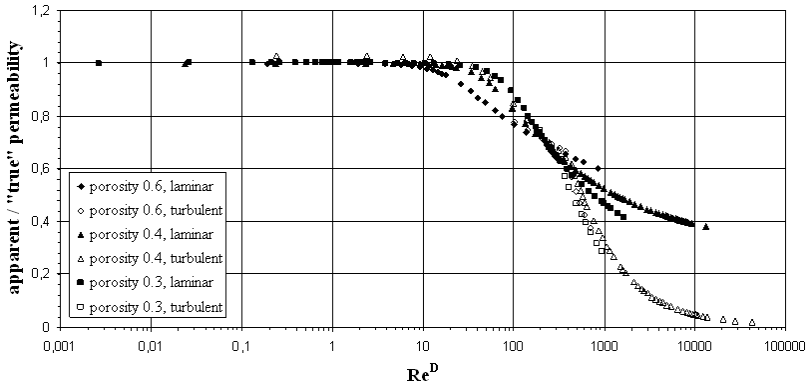

FIG. 8: Apparent permeability divided by true permeability for the three porosities (0.3, 0.4, and 0.6), values for both the laminar and also the turbulent case plotted with respect to the new Re^D

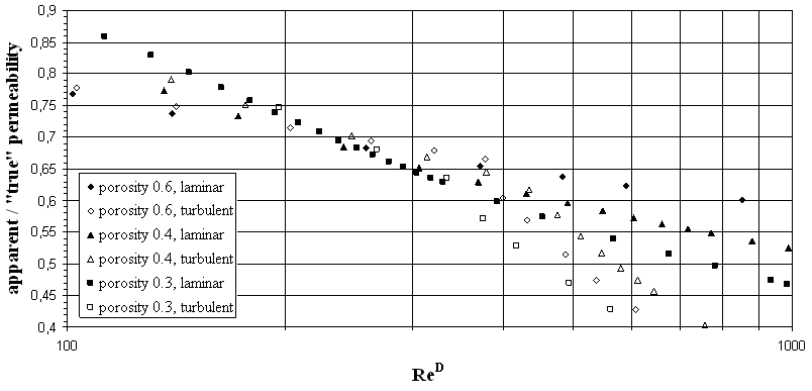

FIG. 9: Apparent permeability divided by true permeability for the three porosities (0.3, 0.4, and 0.6) zoomed in at the area where the onset takes place, values for both the laminar and also the turbulent case plotted with respect to Re^D

By scrutinizing the averaged turbulent velocity field in detail it can be seen that the large circulation zone has more or less the same position for all Re' but increases in strength with Re' (see Fig. 10). When comparing with the results from the laminar setup (Fig. 4), the jet formed has a much weaker development as a function of Re', confirming that the turbulent energy losses are more evenly distributed in the bulk flow (Fig. 10). The next significant flow feature after the jet for the turbulent flow appears on the right-hand side of the cylinder where a distinct separation materializes as the large circulation zone increases in strength. The point of separation climbs closer to the top of the cylinder as Re' increases (see Fig. 11). This predeparture of the jet from the cylinder may cause a relatively lower resistance to flow and might be one of the reasons the simulated results deviate from the Ergun equation at $\mathrm{Re}' > 300$ for $\phi = 0.4$ (see Fig. 7). Such a deviation has not been reported in the literature, to the authors knowledge, and may be related to either the geometrical setup used in this investigation or the fact that rather high Re' values (higher than before) have been simulated with very high accuracy (better than before). As a final remark, it is evident that at low Reynolds numbers the flow fields produced by the laminar and turbulent setups are practically the same.

The force per unit area acting on the cylinder increases dramatically with Re (see Figs. 12 and 13). It is also evident that a turbulent flow assumption will generate larger forces on the cylinder than a laminar one, and that the normal forces are considerably larger than the shear forces (see Figs. 12 and 13). This result is of great importance, for instance, when considering internal erosion in embankment dams, as larger forces acting on the particles create a larger risk of forming a sinkhole and/or progression of the process for a dam to breach. Hence knowledge of the size and distribution of the forces acting inside porous media is important in order to know which simulation approach to use for which flow conditions, since the forces for high Re differ as much as 1 decade when comparing laminar and turbulent setups.

6. CONCLUSIONS

Literature review as well as analysis of a quadratic array of cylinders shows that a number of different Reynolds number values can be defined for porous media. Analysis further shows that this number can be independent of the porosity of the porous media (Re^S), as well as increase (Re', Re^d, and Re^K) or decrease (Re^D) with it. Thus the outcome is critically dependent on which Re is used.

CFD simulations for flow through a quadratic array of cylinders at three solid fractions with a turbulent as well as laminar setup were then performed. All simulations were in good agreement with each other and with the experimental data regarding permeability and friction factor from the creeping flow region up to Re' of about 30. The turbulent simulations with the shear stress transport turbulence model thus capture main flow features even at very low Re' flows. In conformity with the data in the literature, all simulations yield an Re' of about 10 when inertia

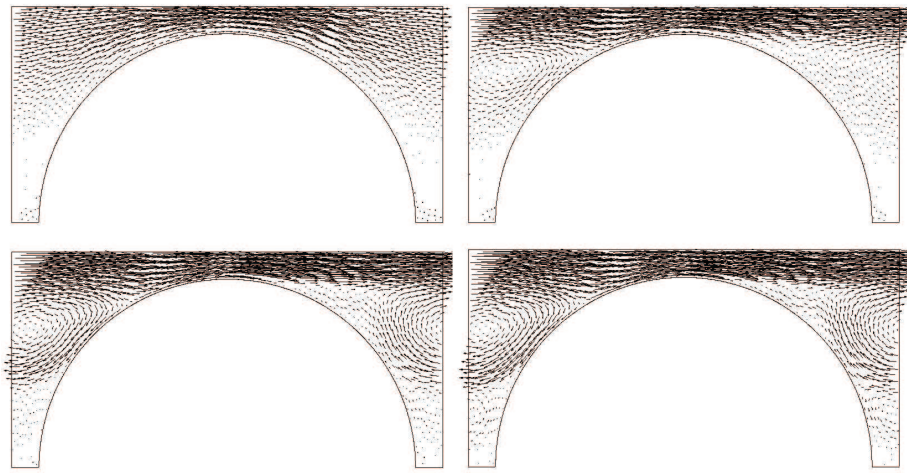

FIG. 10: Vectors representing the velocity field for the turbulent configuration with different Re' values for 0.4 porosity; **(top left)** $\mathrm{Re}' = 1.5$, **(top right)** $\mathrm{Re}' = 200$, **(bottom left)** $\mathrm{Re}' = 1000$, and **(bottom right)** $\mathrm{Re}' = 2000$.

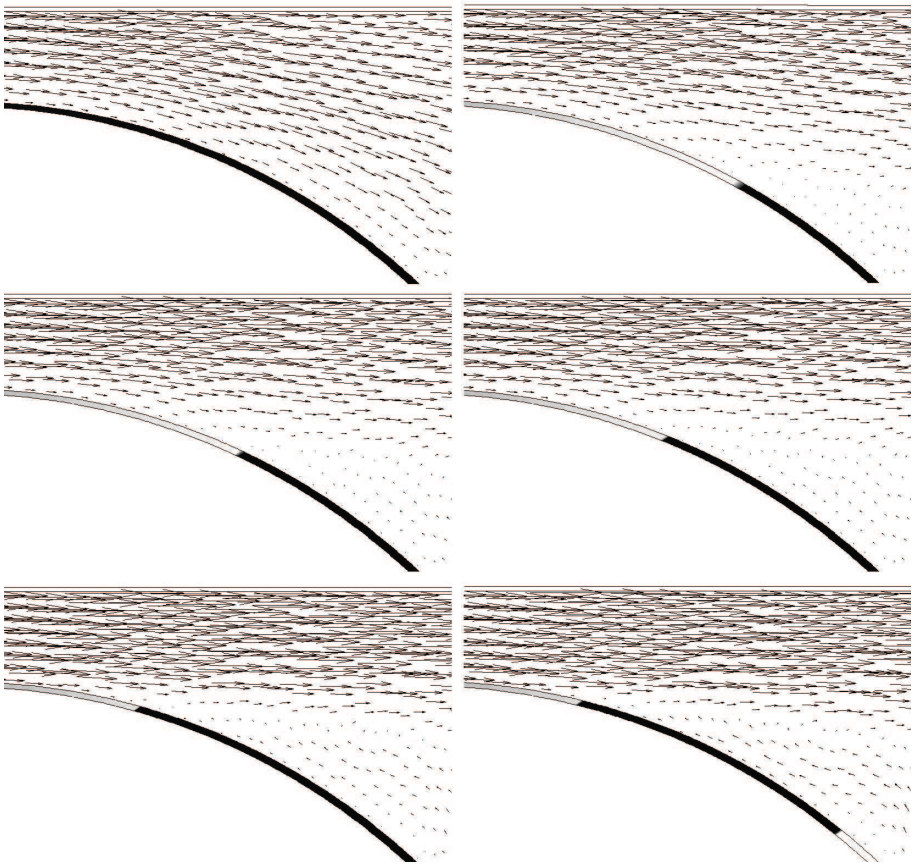

FIG. 11: The length of the vectors represents the velocity and the velocity gradient, du/dy, displayed on the cylinder wall for different Re′ numbers: **(top left)** Re′ = 1.5, **(top right)** Re′ = 65, **(middle left)** Re′ = 120, **(middle right)** Re′ = 210, **(bottom left)** Re′ = 1000, and **(bottom right)** Re′ = 2000. When the velocity gradient turns black, the gradient switches sign and separation occurs.

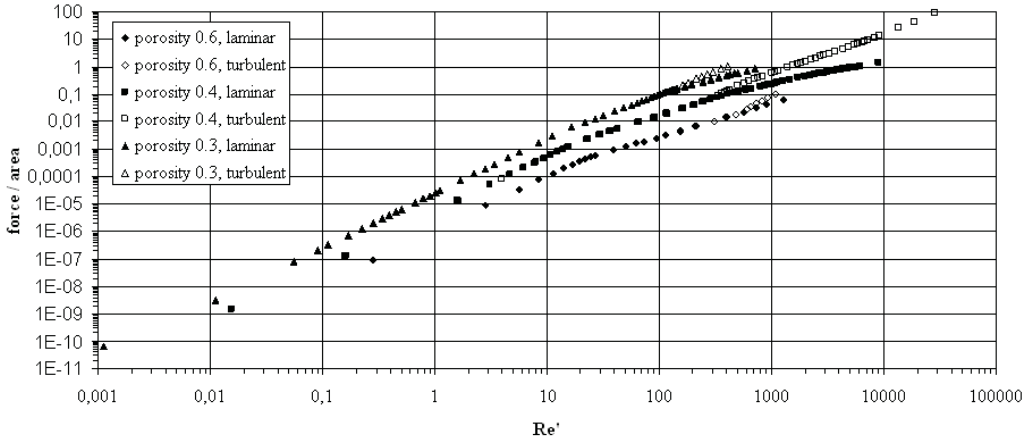

FIG. 12: Shear force acting on the cylinder for different porosities

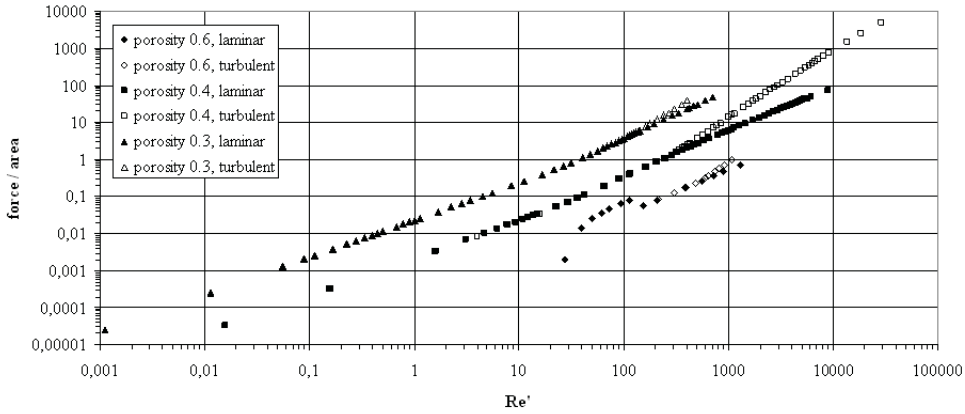

FIG. 13: Normal forces acting on the cylinder for different porosities

effects are considered. For higher Re′ values than 30 the laminar flow simulations produce results that differ from the simulations with a turbulent formulation as well as experimental data from literature. The results from the latter two are similar, however, indicating that the point where turbulence must be considered can be defined as the Re where the laminar and turbulent simulations start to deviate from each other. To get similar conformity regarding this possible onset of turbulence as for the onset of inertia, Re^D must be used instead of Re′. By doing this it is found that turbulent flow needs be considered when Re^D is above 300, since the laminar setup of equations fails to predict the experimental results over this value. The difference between Re′ (or Re^{Dh}) and Re^D is that for the latter only the increase in interstitial velocity is captured when the porosity is decreased, while in the former the decrease in hydraulic diameter is also modelled.

A detailed comparison between the flow fields for the laminar and turbulent setup furthermore yields that a pronounced jet formed close to the middle of the gap for the laminar case is smeared out in the turbulent case. It is also found that circulation zones formed are larger when using a turbulent formulation.

In order to predict the normal and shear forces acting in the porous media, it is essential to make the right choice between laminar and turbulent setup, since the force prediction differs considerably at high Re. This is vital for modelling internal erosion in embankment dams, for instance.

It now remains to link the results obtained in this study to other ordered materials, as well as more disordered materials such as those used in embankment dams, including three-dimensional materials, internal wall effects and effects of a multidisperse system.

ACKNOWLEDGEMENTS

This research presented was carried out as part of the Swedish Hydropower Centre - SVC. SVC has been established by the Swedish Energy Agency, Elforsk, and Svenska Kraftnät together with Luleå University of Technology, The Royal Institute of Technology, Chalmers University of Technology, and Uppsala University (www.svc.nu).

REFERENCES

Beetstra, R., van der Hoef, M. A., and Kuipers, J. A. M., Drag force of intermediate Reynolds number flow past mono- and bidisperse arrays of spheres, *AIChE J.*, vol. **53**, pp. 489–501, 2007.

CFX® (Copyright© 1996-2005), Version 10.0, ANSYS Europe, Ltd.

Comiti, J., Sabiri, N. E., and Montillet, A., Experimental characterization of flow regimes in various porous media—III: Limit of Darcy's or creeping flow regime for Newtonian and purely viscous non-Newtonian fluids, *Chem. Eng. Sci.*, vol. **55**, pp. 3057–3061, 2000.

Casey, M. and Wintergerste, T., Eds., ERCOFTAC (European Research Community on Flow, Turbulence and Combustion) *Special Interest Group on Quality and Trust in Industrial CFD: Best Practice Guidelines*, Version 1.0, 2000.

Dybbs, A. and Edwards, R. V., A new look at porous media fluid mechanics – Darcy to turbulent, In *Fundamentals of Transport Phenomena in Porous Media*, edited by Bear, J. and Corapcioglu, M. Y., Dordrecht: Martinus Nijhoff Publishers, 1984.

Ergun, S., Fluid flow through packed columns, *Chem. Eng. Prog.*, vol. **48**, pp. 89–94, 1952.

Fand, R. M., Kim, B. Y. K., Lam, A. C. C., and Phan, R. T., Resistance to the flow of fluids through simple and complex porous media whose matrices are composed of randomly packed spheres, *J. Fluids Eng*., vol. **109**, pp. 268–274, 1987.

Forchheimer, P., *Wasserbevegung durch Boden, Z. Ver. Deutsch, Ing*., vol. **45**, pp. 1782–1788, 1901.

Gebart, B. R., Permeability of unidirectional reinforcements for RTM, *J. Compos. Mater*., vol. **26**(8), pp. 1100–1133, 1992.

Ghaddar, C. K., On the permeability of unidirectional fibrous media: A parallel computational approach, *Phys. Fluids*, vol. **7**, pp. 2563–2586, 1995.

Hellström, J. G., Marjavaara, B. D., and Lundström, T. S., Parallel CFD simulations of an original and redesigned hydraulic drat tube, *Adv. Eng. Software*, vol. **38**, pp. 338–344, 2006.

Hellström, J. G. I. and Lundström, T. S., Flow through porous media at moderate Reynolds number, *Proc. of the 4th Int'l. Scientific Colloquium Modelling for Material Processing*, Riga, pp. 129–134, 2006.

Hill, R. J., Koch, D. L., and Ladd, A. J. C., The first effects of fluid inertia on flows in ordered and random arrays of spheres, *J. Fluid Mech*., vol. **448**, pp. 213–241, 2001.

Hlushkou, D. and Tallarek, U., Transition from creeping via viscous-inertial to turbulent flow in fixed beds, *J. Chromatogr. A*, vol. **1126**, pp. 70–85, 2006.

Johns, M. L., Sederman, A. J., Bramley, A. S., Gladden, L. F., and Alexander, P., Local transitions in flow phenomena through packed beds identified by MRI, *AIChE J*., vol. **46**, pp 2151–2161, 2000.

Koch, D. L. and Ladd, A. J. C., Moderate Reynolds number flows through periodic and random arrays of aligned cylinders, *J. Fluid Mech*., vol. **349**, pp. 31–66, 1997.

Lesage, F., Midoux, N., and Latifi, M. A., New local measurements of hydrodynamics in porous media, *Exp. Fluids*, vol. **37**, pp. 257–262, 2004.

McFarland, J. D. and Dranchuk, P. M., Visualization of the transition to turbulent flow in porous media, *J. Can. Pet. Technol*., April–June, pp. 71–78, 1976.

Menter, F. R., Zonal two equation k-ω turbulence models for aerodynamic flows, AIAA, Paper 93-2906, July 1993.

Nemec, D. and Levec, J., Flow through packed bed reactors: 1. Single-phase flow, *Chem. Eng. Sci.*, vol. **60**, pp. 6947–6957, 2005.

Papathanasiou, T. D., Markicevic, B., and Dendy, D., A computational evaluation of the Ergun and Forchheimer equations for fibrous media, *Phys. Fluids*, vol. **13**, pp. 2795–2804, 2001.

Pedras, M. H. and de Lemos, M. J. S., Computation of turbulent flow in porous media using a low-Reynolds *k*-ε model and an infinite array of transversally displaced elliptic rods, *Numer. Heat Transfer, Part A*, vol. **43**, pp. 585–602, 2003.

Scheidegger, A. E., *The Physics of Flow through Porous Media*, Toronto: University of Toronto Press, 1960.

Seguin, D., Montillet, A., Comiti, J., and Huet, F., Experimental characterization in various porous media—II: Transition to turbulent regime, *Chem. Eng. Sci*., vol. **53**, pp. 3897–3909, 1998.

Venkataraman, P. and Rama Mohan Rao, P., Darcian, transitional and turbulent flow through porous media, *J. Hydraul. Eng*., vol. **124**, pp. 840–846, 1998.

Ziólkowska, I. and Ziólkowski, D., Fluid flow inside packed beds, *Chem. Eng. Process*, vol. **23**, pp. 137–164, 1988.

Journal of Porous Media 13(12), 1087–1100 (2010)

NEW MODELING APPROACH FOR HEAT AND MASS TRANSFERS DURING SORPTION PHENOMENA IN A PLANE ADSORBER

Abdelaziz Zegnani,[1,*] Abdallah Mhimid,[1] Hacen Dhahri,[1] & Khalifa Slimi[2]

[1]*Ecole Nationale d'Ingénieurs de Monastir, Rue Ibn Eljazzar, 5019, Monastir, Tunisia*

[2]*Institut Préparatoire aux Etudes d'Ingénieurs, Rue Ibn Eljazzar, 5019, Monastir, Tunisia*

[*]Address all correspondence to Abdelaziz Zegnani E-mail: aziz_zegnani@voila.fr

Original Manuscript Submitted: 3/7/2009; Final Draft Received: 6/23/2009

A model approach for heat and mass transfers during gas sorption by a zeolite bed is developed. The mathematical modeling is based on assuming the bed to be formed with three phases—solid, liquid, and gaseous. The classical finite volume method is used to numerically solve the differential set of governing macroscopic equations. Numerical results provide us the time–space evolutions of temperature and moisture content. A comparison between results obtained with a three-phase model versus those obtained with a two-phase model is performed and discussed. A comprehensive analysis of the influence of the bed porosity and the grain porosity on the average reduced moisture content and average reduced temperature is also investigated.

KEY WORDS: *zeolite, desorption, plane desorber, moisture content, numerical simulation, three-phase model, two-phase model*

1. INTRODUCTION

Heat transfer and fluid flow in porous media with phase change appears in many applications such as drying systems, geothermal systems, heat-transfer materials design, and nuclear analysis (Auriault and Adler, 1995; Andrew et al., 2003; Duval et al., 2004; Badruddin et al., 2006). Modeling heat and mass transfers in porous media has attracted important research interest in many published books (Ingham and Pop, 1998; Nield and Bejan, 1999; Vafai, 2000; Pop and Ingham, 2001). There are two different modeling approaches for heat transfer in porous medium based on the validity or invalidity of the local thermal equilibrium. When the local thermal equilibrium assumption is assumed to hold (Mhimid, 1998), only one energy conservation equation is required to predict heat-transfer behavior. However, in the local thermal nonequilibrium case (Berthoud and Valette, 1994; Angelini et al., 1995; Duval et al., 2004), the two phases are not in local thermal equilibrium condition. Consequently, the two phases have different temperatures. In this case, two energy conservation equations, one for the fluid and the other for the solid matrix, are needed to predict heat transfer. These two energy conservation equations are coupled together by a convective term.

The difficulty inherent to heat-transfer modeling in sorption phenomena is strongly subordinate to whether the local thermal equilibrium assumption is valid or not. Numerous published studies related to sorption phenomena are based on a two-temperature model (Mhimid et al., 1997; Wu et al., 2009; Hu et al., 2009). In the local nonequilibrium thermal approach, the involved temperatures are that of the gas and that of the solid, so the liquid and the solid together are supposed to form the same phase. The local thermal nonequilibrium model for two-phase flows with phase change in porous media

1091–028X/10/$35.00

NOMENCLATURE

C_p	specific heat, J kg^{-1}K^{-1}
d_p	mean particle diameter, m
H	height of the bed, m
h_m	heat-transfer coefficient between the bed and the heating source, W m^{-2}
h_0	heat-transfer coefficient at the bed inlet, W m^{-2}
k	permeability, m^2
L	length of the bed, m
$\dot{m}$	evaporation rate, kg m^{-3} s^{-1}
P	pressure, kg m^{-1}s^{-2}
T	temperature, K
t	time, s
U_0	heating gas velocity, m s^{-1}
V_g	gas velocity, m s^{-1}
X	moisture content, kg/kg
y	transverse coordinate, m
z	axial coordinate, m

Greek symbols

ΔH	latent heat of vaporization, J kg^{-1}
ε_b	bed porosity
ε_m	grain porosity
λ	thermal conductivity, W m^{-1}K^{-1}
ρ	density, kg m^{-3}
μ	viscosity, kg m^{-1} s^{-1}
τ	volume, m^3

Subscripts

c	condenser
eff	effective
g	gas
h	heating
i	initial
l	liquid
s	solid
sat	saturation
vap	vapor
y	along *y*-axis
z	along *z*-axis

has been studied by Duval et al. (2004). The volume-averaging method has been used in order to derive a three-temperature macroscopic model assuming a local thermal nonequilibrium between the three phases (gas, solid, and liquid).

Studies related to heat and mass transfer modeling in an adsorber (Mhimid, 1998; Maggio et al., 2004; El Fadar et al., 2009; Demir et al., 2009) have supposed the system to be composed of two phases: the solid and the liquid are one phase and the vapor constitutes the second phase. Marletta et al. (2002) have undertaken a nonuniform temperature and a nonuniform pressure dynamic model of heat and mass transfers in compact adsorbent beds composed of three phases, solid, liquid, and vapor. Liu and Leong (2005) have numerically investigated the effect of operating conditions on thermal performance (coefficient of performance and specific cooling power) of zeolite 13X/water adsorption cooling systems. Both heat- and mass-transfer limitations are taken into account in the numerical model. Darcy's law and the linear driving force (LDF) model are used to describe the mass-transfer limitation between the particles and within the particle, respectively. Hu et al. (2008) have considered the composite zeolite/foam aluminum–water mass recovery adsorption refrigeration system driven by engine exhaust heat. In this paper the composite zeolite/foam aluminum is proposed to enhance heat and mass transfers for adsorption refrigeration. The effective thermal conductivity of this composite material is 2.89 W/mK measured by the hot disk method with the same zeolite packed bed adsorption performance. The performance of this composite zeolite/foam aluminum–water mass recovery adsorption refrigeration device driven by engine exhaust gases has also been calculated by the authors. Both numerical simulations and experimental study of a modified zeolite 13X–water adsorption refrigeration model have been presented by Wu et al. (2009). The performance of the adsorption cooling module (16 mm in diameter and 1020 mm in length) with zeolite 13X–water as the adsorption working pair has been calculated by the authors. A dynamic heat- and mass-transfer model has been established based on the LDF model. Ferni et al. (2009) have developed

a mathematical model for zeolite synthesized on copper foam for adsorption chillers. In this study, a new adsorbent bed for adsorption chillers is proposed. Highly porous copper foams were directly sintered on the external surface of copper pipes. Afterward, the foam surface was coated by several layers of zeolite 4A by in situ hydrothermal synthesis. The performance of an adsorbent bed based on the proposed configuration was then evaluated using a dynamic model.

As far as we know, studies related to the three-phase model during desorption have not been performed, which motivated the present investigation. In the current study we aim to develop a mathematical model simulating coupled heat and mass transfers within a plane adsorber during the gas sorption by a zeolite 13X on the basis of a scale change. It is assumed that the representative elementary volume (REV) is formed with three phases, gas, liquid, and solid. The considered phases are supposed to be in local thermal equilibrium, and therefore a one-equation model is adopted to predict the heat-transfer rate.

A comparison between numerical results obtained by the proposed model with three phases (MOD3P) versus those obtained using a classical model assuming the existence of only two phases (MOD2P) is performed and discussed.

2. MATHEMATICAL FORMULATION

2.1 Problem Definition and Governing Equations

The plane adsorber considered in this paper can exchange heat through all surfaces (Fig. 1) with hot air at constant temperature and constant flow rate. The adsorber is composed of a solid phase (zeolite), liquid phase (water), and a gaseous phase (vapor water). The macroscopic equations governing coupled heat and mass transfer are derived from the volume-averaging technique (Whitaker, 1977).

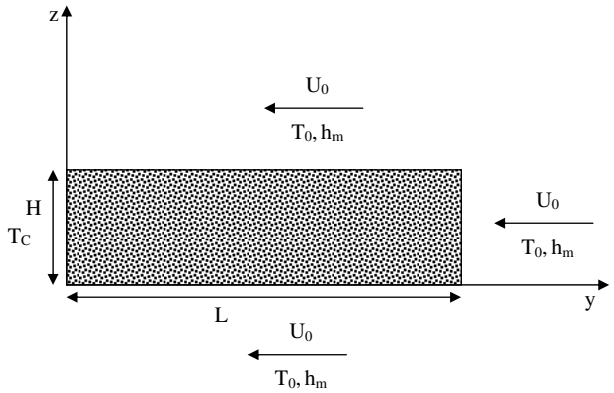

FIG. 1: Sketch of the physical problem and the coordinates system

Figure 2 shows a skeleton of an REV. The liquid and gas phases were in a rigid section of the porous medium. Solid is denoted by s-phase, liquid by l-phase, and the vapor by g-phase. The thermophysical properties of the porous bed are assumed to be constant and independent of temperature in the range of pressure and temperature considered here.

2.2 Model with Two Phases (MOD2P)

In this model, the solid and liquid are assumed to form the same phase. Several assumptions are made in order to obtain a closed set of governing macroscopic equations:

- Coupled heat and mass transfers and fluid flow are assumed to be two-dimensional;
- The solid particles are incompressible;
- The local thermal equilibrium assumption for the energy conservation equation as well as the Darcy flow model are assumed to be valid;
- The compression work and viscous dissipation are negligible;
- The gas phase is ideal from a thermodynamic point of view, and radiative transfer is negligible regardless of the other heat-transfer modes;
- A unique macroscopic porosity (or bed porosity) is used.

On the basis of the above assumptions, the macroscopic governing equations can be written as follows:

Mass conservation equation

$$\varepsilon_b \frac{\partial \rho_g}{\partial t} + \operatorname{div}\left(\rho_g \overrightarrow{v}_g\right) = -\dot{m}, \tag{1}$$

where ρ_g, $\overrightarrow{v}_g$, and $\dot{m}$ are the gas density, the gas velocity, and the desorbed mass rate, respectively.

Momentum equation (Darcy's law)

$$\overrightarrow{v_g} = -\frac{k}{\mu}\overrightarrow{\operatorname{grad}}\, P, \tag{2}$$

where *k* is the permeability of the medium, given by the Koseny-Carmen empirical relation as follows:

$$k = \frac{\varepsilon_b^3 d_p^2}{150\left(1-\varepsilon_b\right)^2}.$$

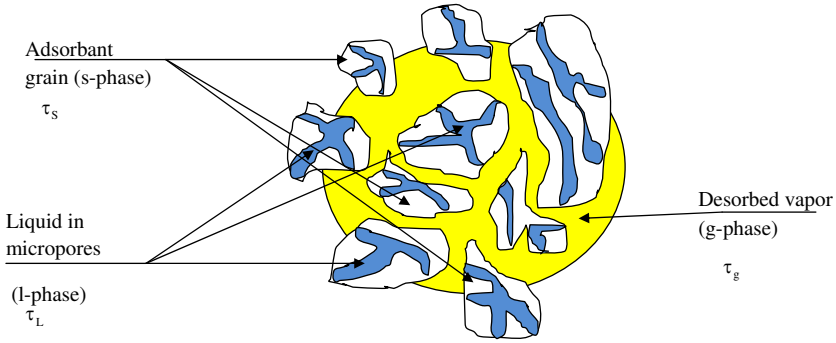

FIG. 2: A skeleton of a representative elementary volume of the porous bed

Energy conservation equation

$$(\rho C_p)_{\text{eff}} \frac{\partial T}{\partial t} + \rho_g C_{Pg} \overrightarrow{v}_g \overrightarrow{\text{grad}T} = \dot{m} \Delta H_{vap} + \text{div}\left(\lambda_{\text{eff}} \overrightarrow{\text{grad}T}\right) \quad (3)$$

The effective heat capacity and the effective thermal conductivity of the porous media are respectively given by

$$(\rho C_p)_{\text{eff}} = \left[(1-\varepsilon_b)\,\rho_s\,(C_{Ps} + XC_{Pl}) + \varepsilon_b \rho_g C_{Pg}\right]$$

and

$$\lambda_{\text{eff}} = \varepsilon_b \lambda_g + (1-\varepsilon_b)\,\lambda_s,$$

where λ_g and λ_s denote the gas thermal conductivity and the solid thermal conductivity, respectively, and ε_b is the bed porosity.

Desorption kinetic

$$\dot{m} = (1-\varepsilon_b)\,\rho_s \frac{\partial X}{\partial t} \quad (4)$$

where *X* is the moisture content.

2.3 Model with Three Phases (MOD3P)

In this model we have adopted the same assumptions as in the last model (i.e., with two phases), except for the definition of a new porosity (the grain porosity) besides the bed porosity, ε_b. In this model two different porosities are considered, since the liquid itself is assumed to form a separate phase.

On the basis of these assumptions, the problem is governed by macroscopic governing Eqs. (1)–(3), where the effective heat capacity and the effective thermal conductivity are now written as follows:

$$(\rho C_p)_{\text{eff}} = (\varepsilon_S \rho_S C p_S + \varepsilon_L \rho_L C p_L + \varepsilon_g \rho_g C p_g)$$

$$\lambda_{\text{eff}} = (\varepsilon_S \lambda_S + \varepsilon_L \lambda_L + \varepsilon_g \lambda_g)\,.$$

After development (Annex A), the effective heat capacity can be written as follows:

$$(\rho C_p)_{\text{eff}} = (1-\varepsilon_b)\,(1-\varepsilon_m)\,\rho_S\,(C p_S + XC p_L) + \varepsilon_b \rho_g C p_g.$$

Then the effective thermal conductivity expression becomes

$$\lambda_{\text{eff}} = (1-\varepsilon_b)\,(1-\varepsilon_m)\,\lambda_S + (1-\varepsilon_b)\,\varepsilon_m \lambda_L + \varepsilon_b \lambda_g.$$

Desorption kinetic

From the continuity equation, it results that

$$\frac{\partial\,(\varepsilon_L \rho_L)}{\partial t} = \dot{m}.$$

After development (Annex B) the kinetic desorption is given by

$$\dot{m} = (1-\varepsilon_b)\,(1-\varepsilon_m)\,\rho_S \frac{\partial X}{\partial t}. \quad (5)$$

Moisture Content (Dubinin Equation)

The moisture content is determined by the Dubinin's equation:

$$X = X_0 \exp\left[-D\left[T \log\left(\frac{P_s\,(T)}{P_s\,(T_c)}\right)\right]^2\right] \quad (6)$$

where $X_0 = 0.269$ kg of water/kg of zeolite and $D = 1.802 \times 10^{-7}\ \text{K}^{-2}$ are two coefficients determined experimentally (Mhimid, 1998).

In the present study, $\log\left[P_s\,(T)\right]$ is given by the following relation (Mhimid, 1998):

$$\log\left[P_s\,(T)\right] = a_1 - \frac{a_2}{T}, \quad (7)$$

where a_1 = 20.9 and a_2 = 5225.5 K. Thus, the Dubinin equation giving X becomes

$$X = X_0 \exp\left[-DB^2\left(\frac{T}{T_c}-1\right)^2\right]. \quad (8)$$

2.4 Initial and Boundary Conditions

The temperature, pressure, and liquid content in the adsorber are initially supposed to be constant:

$$T(0,y,z)=T_i;\quad P(0,y,z)=P_i;\quad X(0,y,z)=X_i \quad (9)$$

where T_i, P_i, and X_i are, respectively, the initial temperature, the initial pressure, and the initial moisture content present in the medium. At the inlet face (i.e., at y = 0), the hydrodynamic boundary condition is written as

$$P(t,0,z) = P_c \quad (10a)$$

The faces ($y = L$), (z = 0), and ($z = H$) are impermeable to mass transfer, and then

$$\frac{\partial P}{\partial y}(t,L,z) = 0; \quad v_y(t,L,z) = 0 \quad (10b)$$

$$\frac{\partial P}{\partial z}(t,y,0) = 0; \quad v_z(t,y,0) = 0 \quad (10c)$$

$$\frac{\partial P}{\partial z}(t,y,H) = 0; \quad v_z(t,y,H) = 0. \quad (10d)$$

At the entrance region (i.e., at y = 0), the thermal boundary condition is written as

$$\lambda_{\text{eff}}\frac{\partial T}{\partial y}(t,0,z) = h_0(T-T_c). \quad (11a)$$

The adsorber is heated by a hot gas from all faces (Fig. 1). A heat-transfer coefficient h_m is introduced and the thermal boundary conditions at z = 0, $z = H$, and $y = L$ are given by

$$\lambda_{\text{eff}}\frac{\partial T}{\partial z}(t,y,H) = h_m(T_0-T) \quad (11b)$$

$$-\lambda_{\text{eff}}\frac{\partial T}{\partial y}(t,L,z) = h_m(T_0-T) \quad (11c)$$

$$\lambda_{\text{eff}}\frac{\partial T}{\partial z}(t,y,0) = h_m(T_0-T), \quad (11d)$$

where h_m is an average heat-transfer coefficient given by the following expression:

$$h_m = 2h_{(y=L)}.$$

h_y is the local heat-transfer coefficient in the case of a laminar thermal boundary layer (Kays and Crawford, 1993) given by

$$\text{Nu}_y = 0.332\,\text{Pr}^{1/3}\,\text{Re}_y^{1/2}.$$

Due to the definition of local Nusselt number, $\text{Nu}_y = (h_y y)/\lambda_f$, it follows that

$$h_y = 0.332\,\frac{\lambda_f}{y}\,\text{Pr}^{3/2}\,\text{Re}_y^{1/2}, \quad (12)$$

where Pr is the Prandtl number, Re_y is the local Reynolds number, and λ_f is the fluid thermal conductivity.

3. NUMERICAL PROCEDURE

The system of differential equations governing coupled heat and mass transfers during desorption is solved numerically by the classical finite volumes method (Patankar, 1980). We have used an implicit scheme for temporal derivative terms, the upwind scheme for the convective terms, and a centered scheme for the diffusive terms. The obtained numerical code is iterative. The numerical iterations were advanced in time until the actual error for all variables is lower than 10^{-6}.

To determine the value of the minimal size of the mesh for which the numerical code becomes independent of the space steps, we carried out a series of numerical simulations with different mesh sizes starting with a mesh with 26×10 grids. It was observed that the code becomes stable and the computed values of the reduced average moisture content and the reduced average temperature are almost the same with 26×26 grids. Indeed, for mesh of dimensions 52×26, 26×52, and 5×52, results are similar. In the same way, we have carried out different tests on the sensibility of the numerical results to time step. It was shown that Δt=1 s is a trade-off between numerical accuracy, stability, and computational time.

A uniform spatial grid of 26×26 and uniform time step Δt = 1 s were then used in all the calculations performed here. The present code has been validated with the closest available works and good agreement was shown (see, for instance, Zegnani et al., 2009).

4. RESULTS AND DISCUSSION

The plane adsorber used in this study is of length L = 50 cm, width l = 50 cm, and height H = 4 cm. During the adsorption phase, the adsorber is connected to the evaporator where the pressure is 6 mbar and the temperature is

273 K. However, during desorption phase, the adsorber is connected to the condenser with a pressure of 70 mbar and the temperature is 313 K. The adsorber is heated, during desorption, by a flowing hot air at a temperature $T_0 = 180°C$ and cooled, during adsorption, by a flowing cold air at a temperature $T_0 = 20°C$. The thermophysical properties used in all the numerical simulations performed with the three-phase model (MOD3P) are listed in Table 1.

To clearly appreciate the effects of the influencing parameters on fluid flow, heat, and mass-transfer characteristics, we have defined the average reduced temperature and the average reduced moisture content, respectively, as follows:

$$\overline{T}^* = \frac{1}{LH}\int_0^L\int_0^H \frac{T - T_i}{T_0 - T_i} dydz;$$
$$\overline{X}^* = \frac{1}{\omega}\int_\omega \left(\frac{X}{X_i}\right) d\omega \tag{13}$$

4.1 General Description

The numerical results obtained with the model using three phases (MOD3P) and those using only two phases (MOD2P) are presented as curves given the spatial distributions of temperature (Fig. 3) and the time–space evolutions of moisture content (Fig. 4) for different time steps (t =60 s, t = 3600 s, t = 7200 s, t =10,800 s).

It can be seen from Fig. 3 that as time goes on; the overheating propagates inside the medium. From Fig. 4 it can be observed that the front of desorption phenomena moves inside the medium and separates the granular bed in two different regions (dried region and wet region). Evaporation is essentially localized in the zone in which the gradient of moisture content is higher. It can also be seen that the region close to the wall is rapidly dried. As time progresses, the front of evaporation approaches the outlet of the medium and the humid region becomes smaller. By the end of the desorption, the temperature tends asymptotically to the heating temperature and the moisture content tends to its equilibrium values in the whole of the medium. In addition, the mass rate is diminished. After a period of time, the remaining quantity of moisture content in the adsorber becomes too small and the evaporation phenomenon is stopped.

TABLE 1: Thermophysical property values used in numerical simulations performed with the three-phase model (MOD3P)

Zeolite	$C_{ps} = 836$ J kg^{-1} K^{-1}, $\lambda_s = 0.2$ W m^{-1} K^{-1}, $d_P = 2.5 \times 10^{-3}$ m, $\varepsilon_b = 0.34$, $\varepsilon_m = 0.32$
Water	$C_{Pl} = 4180$ J kg^{-1} K^{-1}; $\Delta H_{vap} = 3 \times 10^6$ J K^{-1}; $\lambda_L = 0.6$ W m^{-1} K^{-1}
Vapor of water	$C_{Pg} = 1840$ J kg^{-1} K^{-1}; $\lambda_L = 0.024$ W m^{-1} K^{-1}

4.2 A Comparison Study

In order to examine how accurate the new modeling approach based on three different phases is, we performed a comparison between the temperature profiles obtained with the two models (i.e., MOD2P and MOD3P). As shown in Fig. 5, the difference between these curves is important at the lateral faces, because the heating temperature is higher than the initial medium temperature. In addition, this difference increases as time goes on. In the front of the desorption phenomenon, this difference becomes important. It is about 25 K after 1 hour. As times passes, this difference decreases progressively. At the end of desorption it is about 5 K.

In the same way we compared the moisture content calculated by the two models (Fig. 6). Here also we noted a difference between these two curves. This difference reaches 0.03 kg water/kg zeolite after 1 hour. At the end of desorption, it does not exceed 0.01 kg water/kg zeolite.

Heat- and mass-transfer rates predicted by MOD3P are faster than those obtained with MOD2P. This is can be explained by the difference in the thermophysical properties such as $[\lambda_{\text{eff}}]$ and $[(\rho C_P)_{\text{eff}}]$ used in these two models (Figs. 7 and 8). The difference in the effective thermal conductivity value used in the two models is small (about 0.169 Wm^{-1} K^{-1}). However, the difference in the effective heat capacity value used in the two models is large (between 376.964 and 574.713 kJ m^{-3} K^{-1}).

4.3 Comparison with Experimental Data

We have made comparisons between numerical results obtained with the two models (MOD2P, and MOD3P) versus available related experimental data (Marmottant et al., 1992). To perform this comparison, we have considered a plane solar collector 4 cm in thickness filled with 19 kg of zeolite grains. The upper surface of the collector heated by solar energy is 0.87 m^2. In this case, the

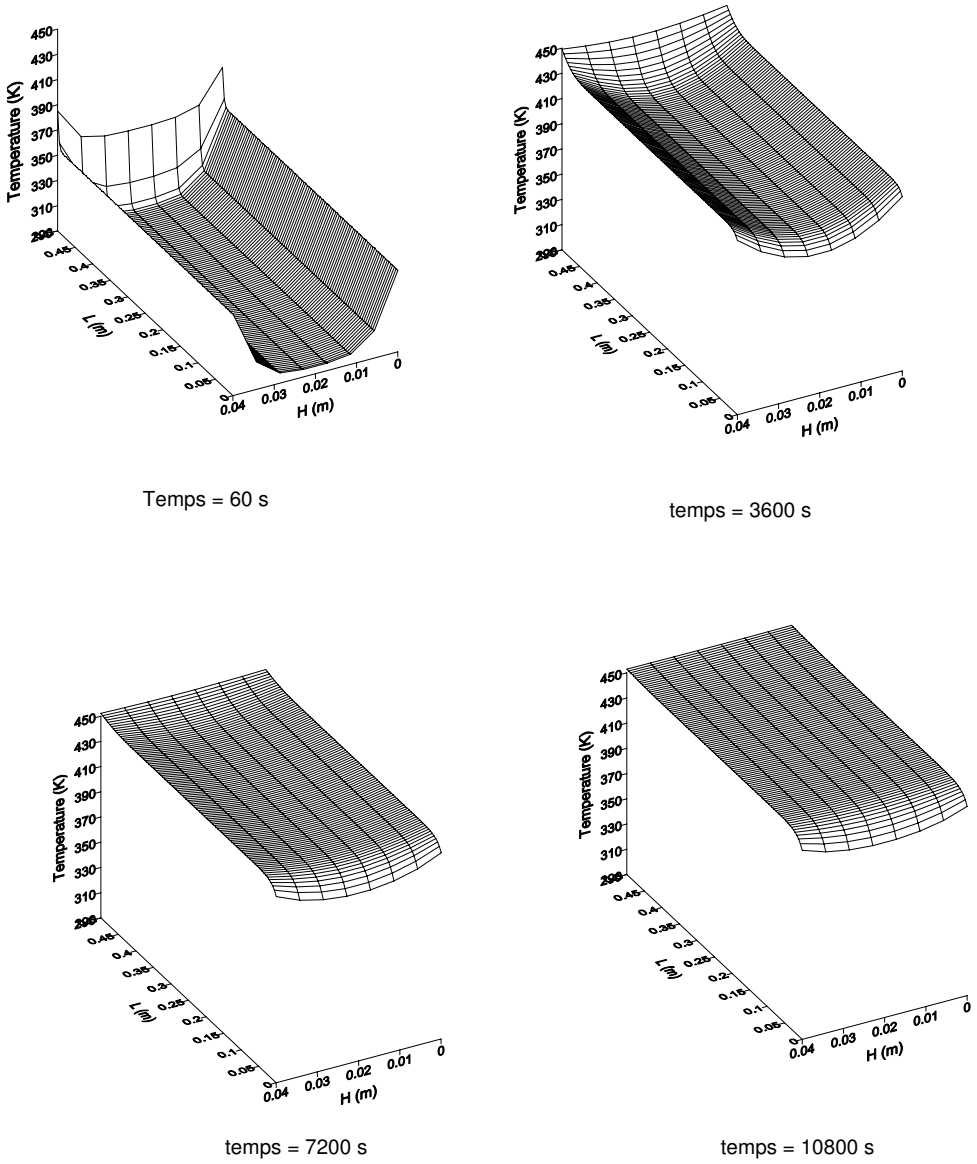

FIG. 3: Time–space evolution of temperature field obtained by MOD3P

temperature T_0 is variable. The temperature of the condenser is T_C = 313 K, and the pressure during desorption is P_C = 70 mbs. The temperature is measured at the midpoint of the upper and lower surface areas of the collector. Numerical and experimental temperature variations with time are plotted in Fig. 9. Numerical and experimental values of the moisture content as a function of time are drawn in Fig. 10. It can be concluded from theses figures that the numerical results obtained by MOD3P are more representative and accurate, as they fit the experimental values better.

4.4 Parametric Study

It is well known that bed porosity as well as grain porosity depend strongly on the size of zeolite grain changed. In this section we study the sensitivity of heat and mass transfers to theses two porosities. Figures 11 and 12, re-

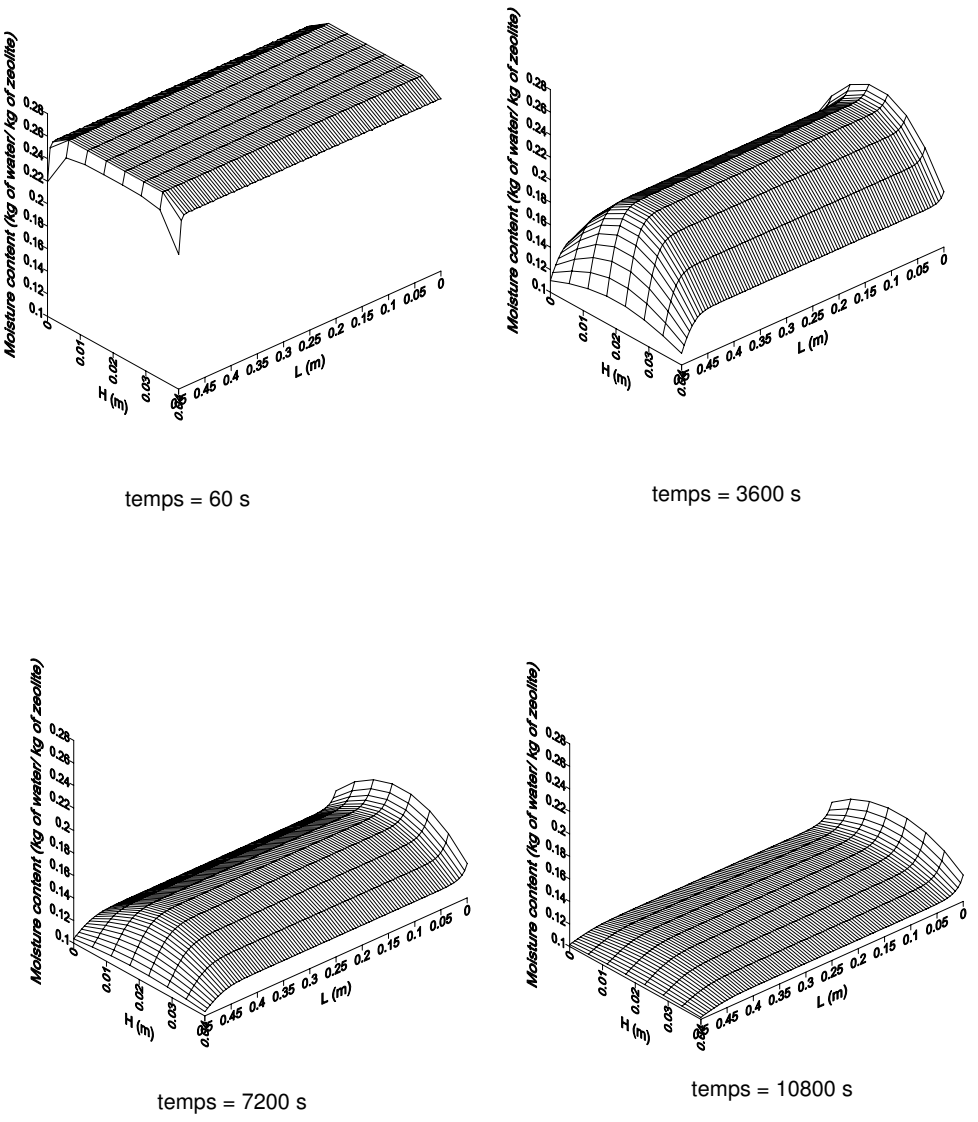

FIG. 4: Time–space evolution of the moisture content obtained by MOD3P

spectively, show the time evolutions of the reduced average temperature and the reduced average moisture content for different values of the bed porosity ε_b and the grain porosity ε_m. As it is seen later, ε_b has less influence on heat- and mass-transfer rates than ε_m.

It can be concluded from Table 2 that increasing ε_m to a certain value around 0.37 has no significant effect on the sorption phenomena. Moreover, decreasing ε_m leads to a decrease in the temporal sorption kinetic. This behavior can be explained by the fact that due to the total volume of liquid contained in the total volume of pores, the mass rate of desorbed water (respectively adsorbed water) decreases.

Table 3 and Fig. 11 show clearly that ε_b has a strong influence on the acceleration of the temporal sorption phenomena. This is evident because varying the volume between the grains of zeolite enhances the vapor velocity.

5. CONCLUDING REMARKS

The problem of two-dimensional transient heat and mass transfer during desorption of water by a plane adsorber of

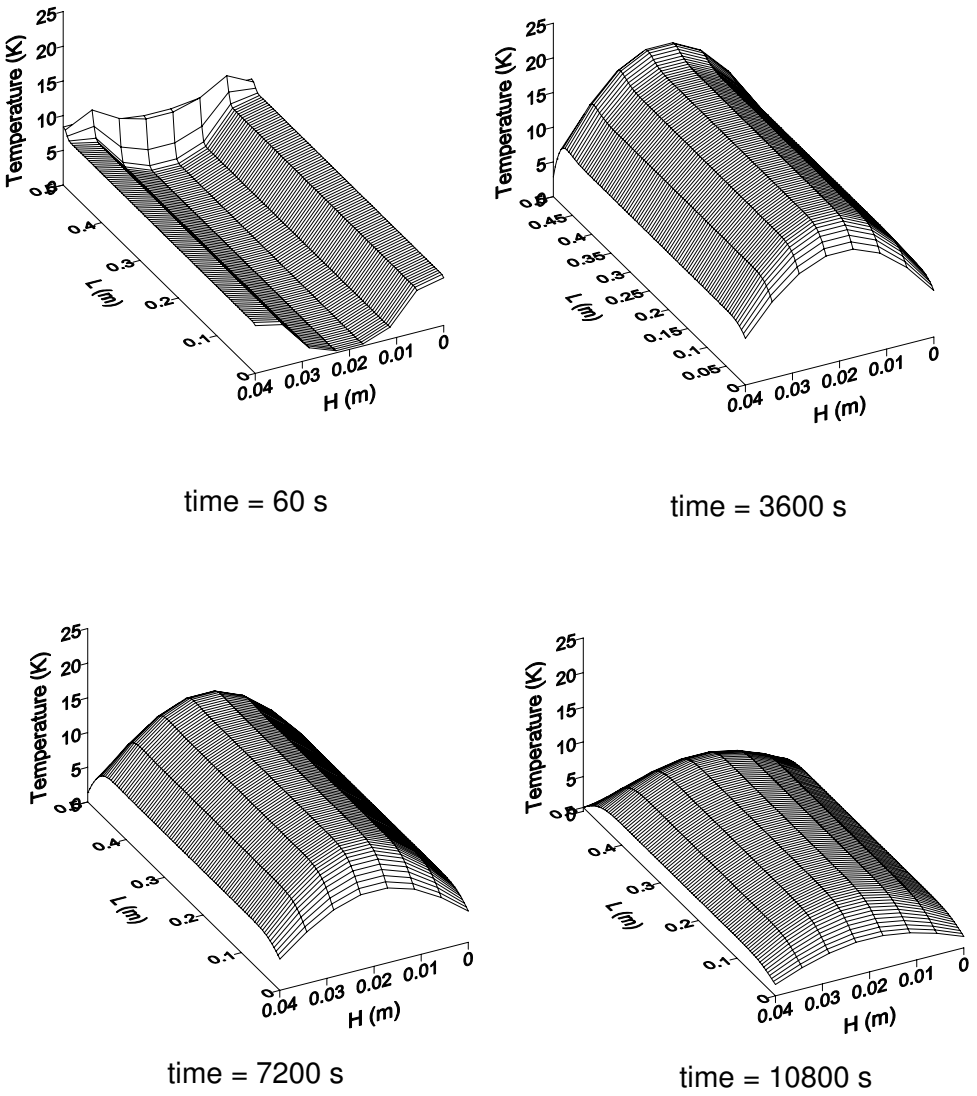

FIG. 5: Time–space evolution of the temperature difference obtained by the two models (MOD2P and MOD3P)

zeolite 13X was the focus of the present investigation. A new modeling approach based on considering the porous bed formed with three different phases was developed and validated with published experimental results. The main results obtained from the numerical solutions can be summarized as follows:

1. The new mathematical model for heat and mass transfer (MOD3P) obtained is more convenient to predict more accurately and rigorously heat and mass transfer in the adsorber than the simple classic model based on two different phases (MOD2P).
2. Increasing the grain porosity leads to serious acceleration of sorption phenomenon. In addition, increasing this parameter up to around 0.37 has no significant effect.
3. Heat- and mass-transfer rates are strongly subordinate to the bed porosity.

Annex A

In the new modeling approach (MOD3P), ε_S, ε_L, and ε_g are, respectively, the solid, liquid, and gas fractions satisfying $\varepsilon_S + \varepsilon_L + \varepsilon_g = 1$. These different fractions are unknown and should be expressed as functions of known

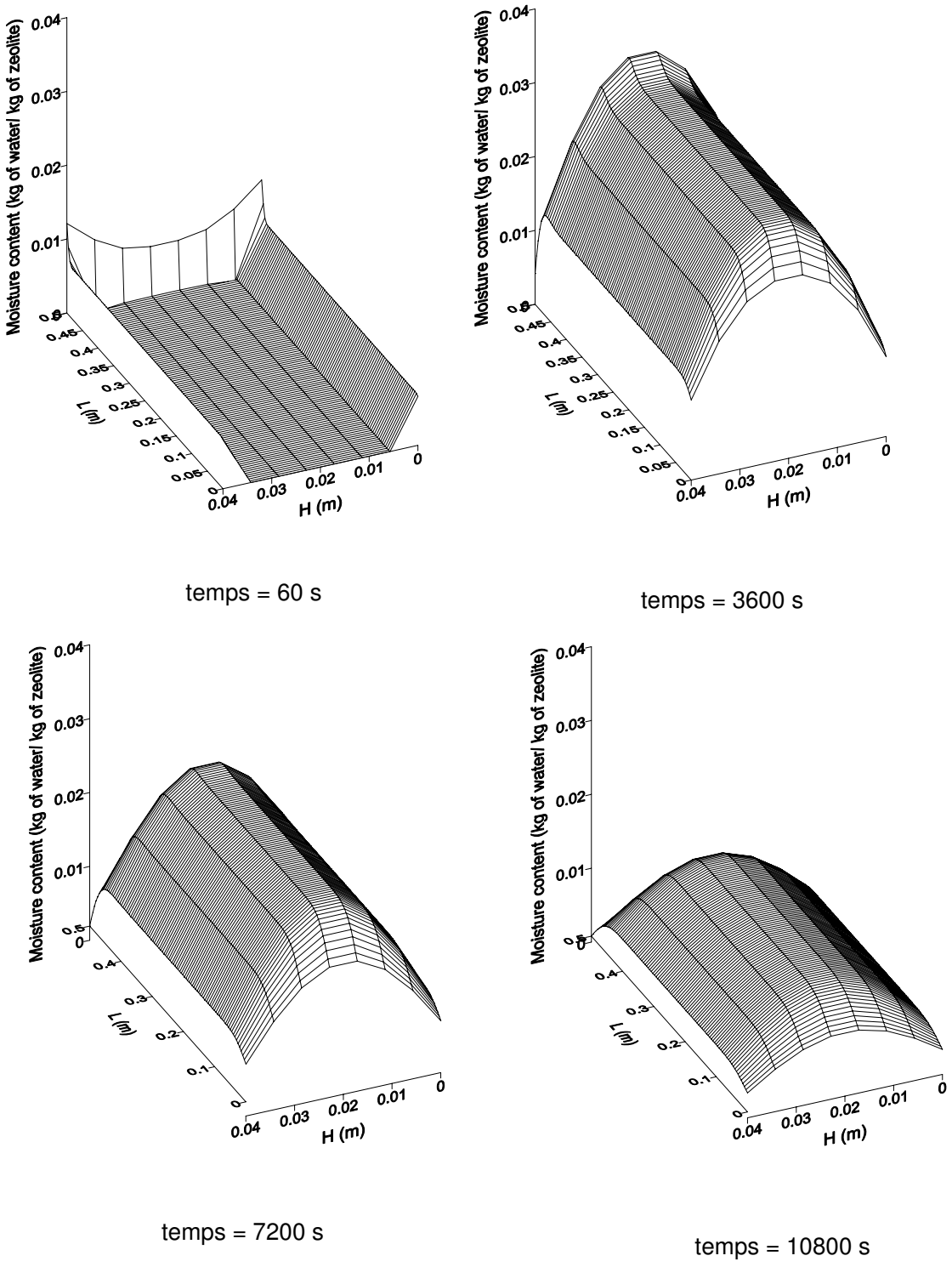

FIG. 6: Time–space evolutions of the moisture content difference obtained by the two models (MOD2P and MOD3P)

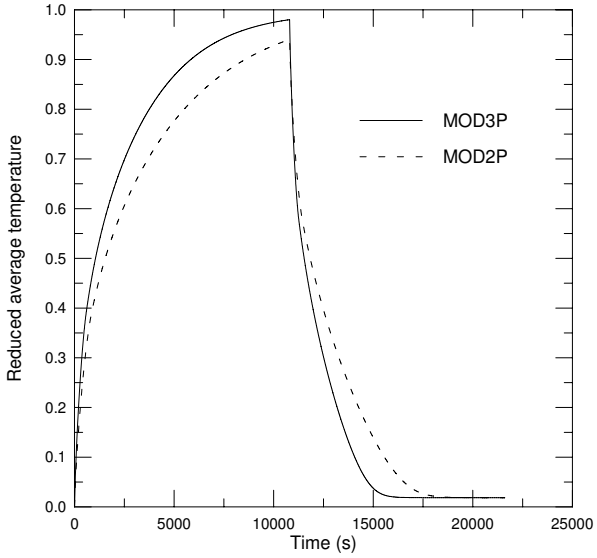

FIG. 7: Temporal evolutions of the reduced average temperature obtained by the two models (MOD2P and MOD3P)

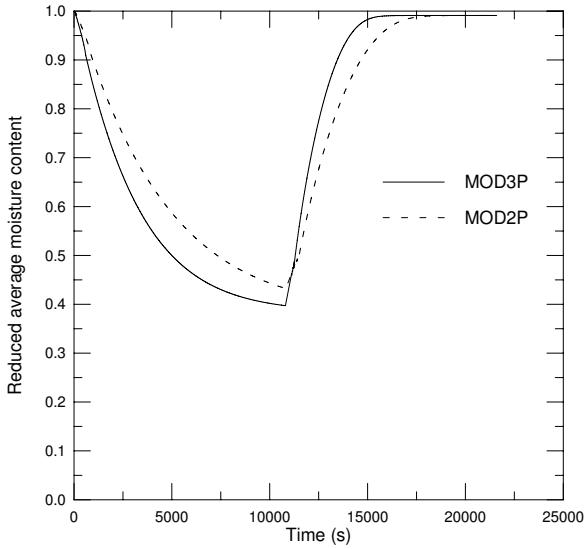

FIG. 8: Temporal evolutions of the reduced average values of the moisture content obtained by the two models (MOD2P and MOD3P)

physical parameters such as the bed porosity ε_b and the grain porosity ε_m.

Since the vapor is located in the total volume between the solid grains, then the gas fraction can be assumed to the equivalent to the bed porosity. Consequently, we have

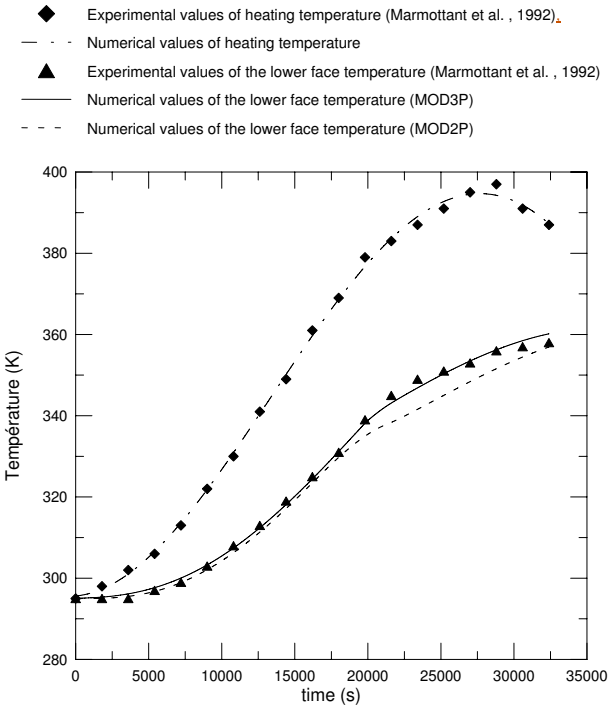

FIG. 9: Comparison between numerical results of temperature field obtained by the two models versus available experimental data

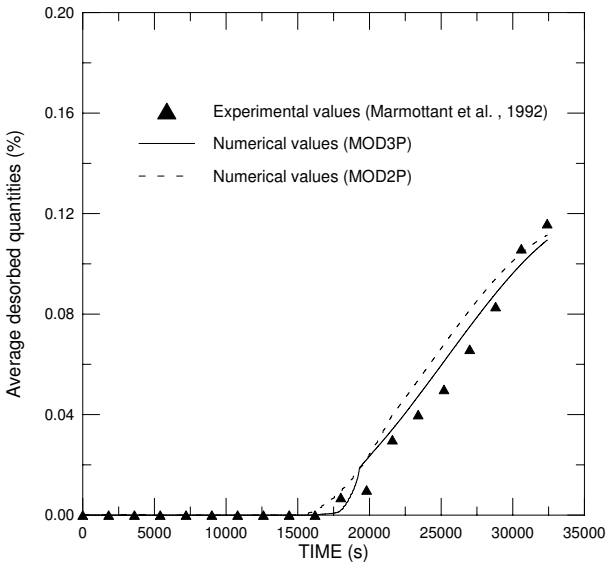

FIG. 10: Comparison between numerical results of moisture content obtained by the two models versus available experimental data

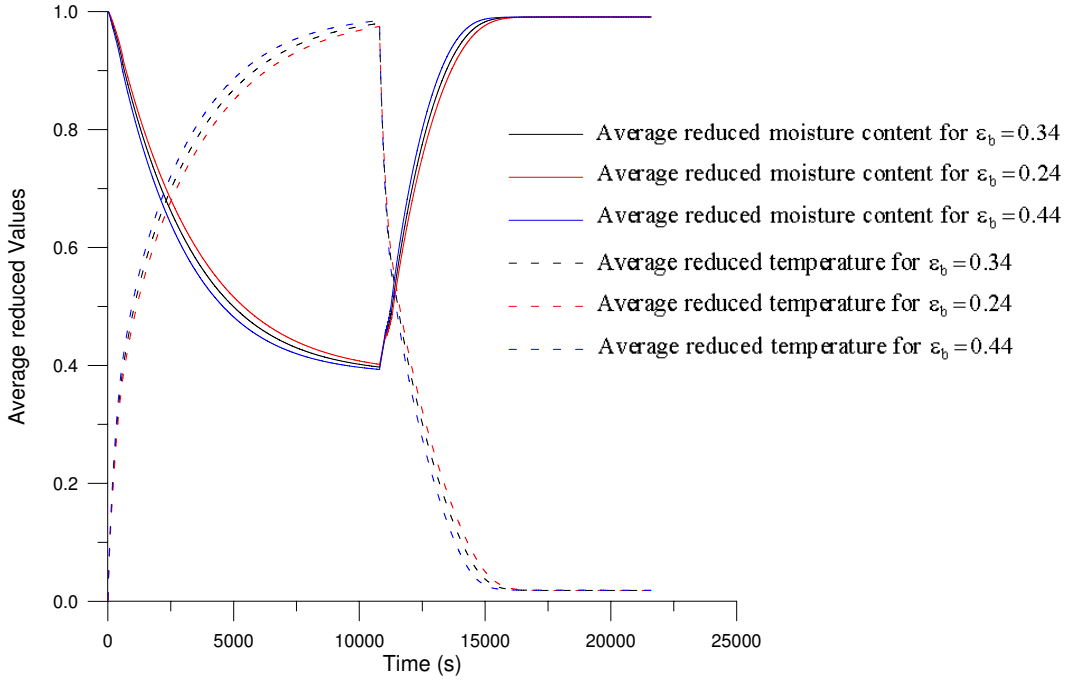

FIG. 11: Influence of the bed porosity on the reduced average moisture content and the reduced average temperature

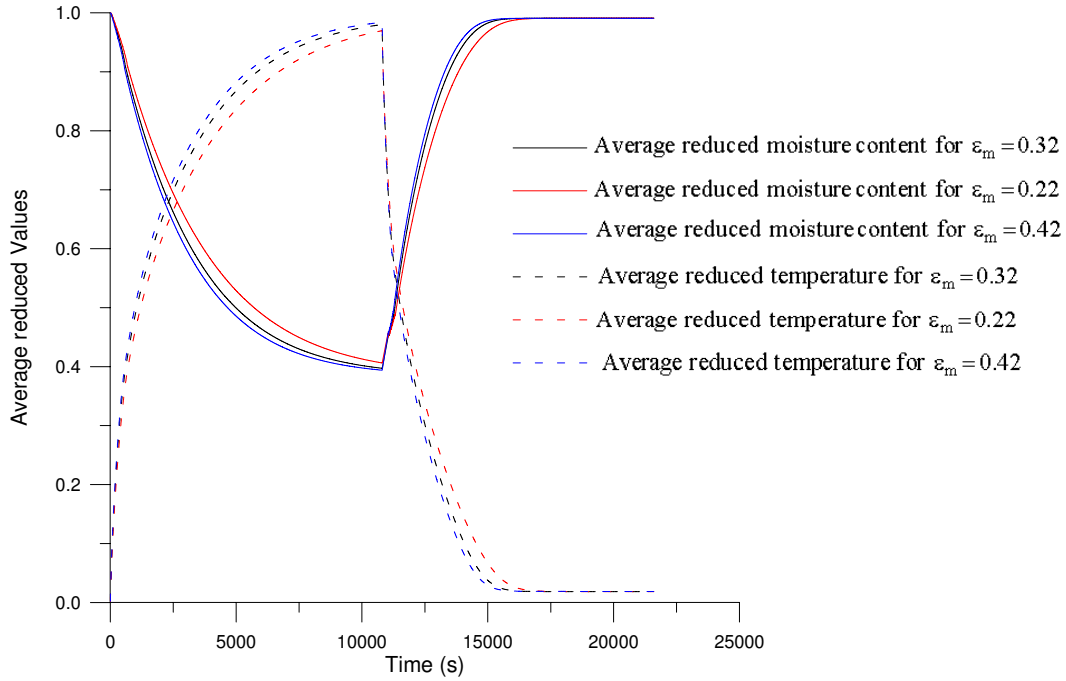

FIG. 12: Influence of grain porosity on the reduced average moisture content and the reduced average temperature

TABLE 2: Time variation of absolute difference in sorption kinetic for different values of ε_m and a real value of $\varepsilon_m = 0.32$

ε_m	0.22	0.27	0.37	0.42
t = 6000 s	5.56%	2.78%	2.76%	2.46%
t = 14,000 s	3.21%	1.59%	1.50%	1.31%

TABLE 3: Time variation of absolute difference in sorption kinetic for different values of $\varepsilon_b = 0.34$

ε_b	0.24	0.29	0.39	0.44
t = 6000 s	3.08%	1.54%	1.53%	3.06%
t = 14,000 s	1.61%	0.78%	0.81%	1.65%

$$\varepsilon_g = \frac{\tau_g}{\tau_T} = \varepsilon_b,$$

where τ_g is the gas volume and τ_T is the total volume.

The grain porosity ε_m is defined as the volume of the micropores contained in the grains. Then we can write

$$\varepsilon_m = \frac{\tau_p}{\tau_{gr}}$$

where τ_p denotes the volume of micropores, and τ_{gr} is the volume of grains. The liquid is assumed to be contained in the micropores. Then the grain porosity ε_m is expressed as

$$\varepsilon_m = \frac{\tau_L}{\tau_S + \tau_L}.$$

This porosity can also be written differently, introducing the total volume τ_T as follows:

$$\varepsilon_m = \frac{\tau_L/\tau_T}{\tau_S/\tau_T + \tau_L/\tau_T},$$

where τ_L is the liquid volume and τ_S is the solid volume. Using the expressions of the solid fractions ε_S and the liquid fraction ε_L as $\varepsilon_S = \tau_S/\tau_T$ and $\varepsilon_L = \tau_L/\tau_T$, then the grain porosity ε_m can be expressed as

$$\varepsilon_m = \frac{\varepsilon_L}{\varepsilon_S + \varepsilon_L}.$$

Consequently, the fractions of liquid, solid, and gas, ε_L, ε_S, and ε_g, are written as functions of the bed porosity ε_b and grain porosity ε_m as follows:

$$\varepsilon_L = (1 - \varepsilon_b)\ \varepsilon_m$$

$$\varepsilon_S = (1 - \varepsilon_b)\,(1 - \varepsilon_m)$$

$$\varepsilon_g = \varepsilon_b.$$

Annex B

The moisture content is defined by

$$X = \frac{m_L}{m_S} = \frac{\tau_L}{\tau_S}\,\frac{\rho_L}{\rho_S}.$$

Dividing this equation by the total volume τ_T leads to

$$X = \frac{\varepsilon_L}{\varepsilon_S}\frac{\rho_L}{\rho_S}.$$

Then, it follows that

$$X\,\varepsilon_S\rho_S = \varepsilon_L\rho_L.$$

Consequently, the mass conservation equation becomes

$$\frac{\partial\,(X\varepsilon_S\rho_S)}{\partial t} = \dot{m}.$$

As ε_S and ρ_S are assumed constant, the mass rate can be expressed as follows:

$$\dot{m} = \varepsilon_S\rho_S\frac{\partial X}{\partial t}.$$

REFERENCES

Angelini, S., Yuen, W. W., and Theofanous, T. G., Premixing related behavior of steam explosions, *Nucl. Eng. Des.*, vol. **155**, pp. 115–157, 1995.

Auriault, J. L. and Adler, P. M., Taylor dispersion in porous media analysis by multiple scale expansions, *Adv. Water Res.*, vol. **18**, no. 4, pp. 217–226, 1995.

Badruddin, I. A., Zainal, Z. A., Aswatha Narayana, P. A., and Seethramu, K. N., Thermal non-equilibrium modeling of heat transfer through vertical annulus embedded with porous medium, *Int. J. Heat Mass Transfer*, vol. **49**, pp. 4955–4965, 2006.

Berthoud, G. and Valette, M., Development of a multidimensional model for the premixing phase of a fuel–coolant interaction, *Nucl. Eng. Des.*, vol. **149**, pp. 409–418, 1994.

Demir, H., Mobedi, M., and Ülkü, S., Effects of porosity on heat and mass transfer in a granular adsorbent bed, *Int. Commun. Heat Mass Transfer*, vol. **36**, pp. 372–377, 2009.

Duval, F., Fichot, F., and Quintard, M., A local thermal non-equilibrium model for two-phase flows with phase-change in porous media, *Int. J. Heat Mass Transfer*, vol. **47**, pp. 613–639, 2004.

El Fadar, A., Mimet, A., Azzabakh, A., Pérez-Garcia, M., and Castaing, J., Study of a new solar adsorption refrigerator powered by a parabolic trough collector, *Appl. Thermal Eng.*, vol. **29**, no. 5–6, pp. 1267–1270, 2009.

Hu, P., Yao, J.-J., and Chen, Z.-S., Analysis for composite zeolite/foam aluminum–water mass recovery adsorption refrigeration system driven by engine exhaust heat, *Energy Convers. Manage.*, vol. **50**, pp. 255–261, 2009.

Ingham, D. B. and Pop, I. (Eds.), *Transport Phenomena in Porous Media*, vol. II, Pergamon, Oxford, 1998.

Kays, W. M. and Crawford, M. E., *Convective Heat and Mass Transfer*, 3rd ed., McGraw-Hill International Edition, 1993.

Liu, Y. and Leong, K. C., The effect of operating conditions on the performance of zeolite/water adsorption cooling systems, *Appl. Thermal Eng*., vol. **25**, pp. 1403–1418, 2005.

Maggio, G., Ferni, A., and Restuccia, G., A dynamic model of heat and mass transfer in double-bed adsorption machines with internal heat recovery, *Int. J. Refrig*., pp. 1–12, 2004.

Marletta, L., Maggio, G., Ferni, A., Ingrasciotta, M., and Restuccia, G., A nonuniform temperature nonuniform pressure dynamic model of heat and mass transfer in compact adsorbent bed, *Int. J. Heat Mass Transfer*, vol. **45**, pp. 3321–3330, 2002.

Marmottant, B., Mhimid, A., Elgolli, S., and Grenier, P. H., Installation de réfrigération solaire á adsorption: Expérimentation et modélisation, *Rev. Gén. Therm.*, vol. **362**, pp. 97–105, 1992.

Mhimid, A., Theoretical study of heat and mass transfer in a zeolite bed during water desorption: Validity of local thermal equilibrium assumption, *Int. J. Heat Mass Transfer*, vol. **41**, pp. 2967–2977, 1998.

Mhimid, A., Jemni, A., and Ben Nasrallah, S., Etude théorique des transferts couplés de chaleur et de masse lors de la désorption du couple zéolithe-eau, *Rev. Gén. Therm.*, vol. **36**, pp. 697–706, 1997.

Nield, D. A. and Bejan, A., *Convection in Porous Media*, 2nd ed., Springer-Verlag, New York, 1999.

Patankar, S. V., *Numerical Heat Transfer and Fluid Flow*, Mc Graw Hill Publishing Company, 1980.

Pop, I. and Ingham, D. B., *Convective Heat Transfer: Mathematical and Computational Modeling of Viscous Fluids and Porous Media*, Pergamon, Oxford, 2001.

Vafai, K., *Handbook of Porous Media*, Marcel Dekker, New York, 2000.

Whitaker, S., Simultaneous heat, mass and momentum transfer in porous media, A theory of drying, *Adv. Heat Transfer*, vol. **13**, pp. 119–203, 1977.

Wu, W.-D., Zhang, H., and Sun, D.-W., Mathematical simulation and experimental study of a modified zeolite 13X–water adsorption refrigeration module, *Appl. Thermal Eng*., vol. **29**, pp. 645–651, 2009.

Zegnani, A., Mhimid, A., and Slimi, K., Study of heat and mass transfer during desorption in a plane adsorber: Anisotropy effects, *J. Porous Media*, vol. **12**, pp. 169–182, 2009.

TECHNICAL NOTES

Journal of Porous Media 13(12), 1103–1109 (2010)

IMPLICATIONS OF EVOLUTIONARY EQUATIONS IN ELASTICITY OF POROUS MATERIALS

M. Marin

Department of Mathematics, University of Brasov, Romania, E-mail: m.marin@unitbv.ro

Original Manuscript Submitted: 8/1/2008; Final Draft Received: 7/13/2009

In this study we prove the existence and uniqueness of solutions for the mixed initial-boundary value problems in the context of the elasticity of micropolar porous bodies through an equation of evolution. In the same manner, the continuous dependence of the solutions upon initial data and supply terms is also proved.

KEY WORDS: *evolutionary equations, porous materials, micropolar body, AMS classification: 35M12, 43A60, 74H20, 74L10*

1. INTRODUCTION

In the opinion of many researchers, the theory of bodies with voids is quite sufficient for a large number of solid mechanics applications. The origin of the theories of bodies with voids dates back to Goodman and Cowin (1972). In their paper we introduce an additional degree of freedom in order to develop a continuum theory for flowing granular materials. Previously, Nunziato and Cowin (1983) established the theory of elastic materials with voids, Iesan (1986) established the general equations in the context of the theory of the thermo-elasticity of materials with voids, and Marin (1995, 1997, 2009) obtained some reasonable extensions of the previous results regarding materials with voids.

The present study is dedicated to the behavior of the solids in which the matrix material is elastic and the interstices are voids of material. The intended applications of these theories are to geological materials, like rocks and solids, and to manufactured porous materials.

The plan of this paper is as follow. First, the basic equations and conditions of the mixed boundary value problem within the context of the theory of porous materials are given. Then, a nonhomogeneous and anisotropic elastic material is considered and the initial-boundary value problem is transformed in an abstract temporally homogeneous evolutionary equation in Hilbert space. By using the results from the theory of semigroups of linear operators, the existence, uniqueness, and continuous dependence results are derived. The proof is given for the first boundary value problem, but the results are the same in the case when the boundary conditions are replaced with those from the second problem and, also, with those from the third problem.

2. BASIC EQUATIONS AND CONDITIONS

For convenience, the notations and terminology chosen are almost identical to those given previously (Marin, 1995, 1997). Consider that our body occupies—at time $t = 0$—a properly regular region B of Euclidian three-dimensional spaceR^3. Assume that domain B is bounded by the piece-wise smooth surface ∂B. We refer to the motion of the continuum to a fixed system of rectangular Cartesian axes, $Ox_i,\ i = 1, 2, 3$ and adopt the Cartesian tensor notation. The points in B are denoted as x_i (or x). The variable t is time and we have $t \in [0, t_0]$. We employ the usual convention of summation over repeated subscripts while that the subscripts preceded by a comma denote the partial differentiation with respect to the respective spatial argument.

We also use a superposed dot to denote the partial differentiation with respect to time variable t. Latin indices are understood to range over the integers $(1, 2, 3)$.

The behavior of a micropolar body with voids is characterized by the following kinematic variables:

1091–028X/10/$35.00

$$u_i = u_i(x,t), \quad \phi_i = \phi_i(x,t), \quad \sigma = \sigma(x,t),$$
$$(x,t) \in \bar{B}_0 \times [0,t_0] \tag{1}$$

If we assume that the body is free of initial and couple stresses and has zero intrinsic equilibrated body forces, then we can write the internal energy density in the form

$$\rho_0 e = \frac{1}{2}A_{ijmn}\varepsilon_{ij}\varepsilon_{mn} + B_{ijmn}\varepsilon_{ij}\mu_{mn} + \frac{1}{2}C_{ijmn}\mu_{ij} \times \mu_{mn} + \frac{1}{2}\xi\sigma^2 + \frac{1}{2}A_{ij}\sigma_{,i}\sigma_{,j} + P_{ij}\varepsilon_{ij}\sigma + R_{ij}\mu_{ij}\sigma + Q_{ijk}\varepsilon_{ij}\sigma_{,k} + S_{ijk}\mu_{ij}\sigma_{,k} + d_i\sigma\sigma_{,i} \tag{2}$$

Where the constitutive coefficients $A_{ijmn}, B_{ijmn}, ..., d_i$ are prescribed functions and they obey the following symmetry relations:

$$A_{ijmn} = A_{jimn} = A_{mnij}, \quad C_{ijmn} = C_{mnij}$$
$$A_{ij} = A_{ji}, \quad P_{ij} = P_{ji}, \quad Q_{ijm} = Q_{jim} \tag{3}$$

Taking into account the internal energy density in the form [Eq. (2)] and symmetries [Eq. (3)], we obtain the basic equations of the elasticity of micropolar bodies with voids as follows:

- The equations of motion

$$t_{ij,j} + \rho_0 F_i = \rho_0 \ddot{u}_i$$
$$m_{ij,j} + \varepsilon_{ijk}t_{jk} + \rho_0 G_i = I_{ij}\ddot{\phi}_j \tag{4}$$

- The balance of the equilibrated forces

$$h_{i,i} + g + \rho_0 L = \rho_0 k\ddot{\sigma} \tag{5}$$

- The constitutive equations

$$t_{ij} = A_{ijmn}\varepsilon_{mn} + B_{ijmn}\mu_{mn} + P_{ij}\sigma + Q_{ijk}\sigma_{,k}$$
$$m_{ij} = B_{ijmn}\varepsilon_{mn} + C_{ijmn}\mu_{mn} + R_{ij}\sigma + S_{ijk}\sigma_{,k}$$
$$h_i = D_{mni}\varepsilon_{mn} + E_{mni}\mu_{mn} + d_i\sigma + A_{ij}\sigma_{,j}$$
$$g = -P_{ij}\varepsilon_{ij} - R_{ij}\mu_{ij} - d_i\sigma_{,i} - \xi\sigma \tag{6}$$

- The geometrical equations

$$\varepsilon_{ij} = u_{j,i} + \varepsilon_{ijk}\phi_k$$
$$\mu_{ij} = \phi_{j,i}$$
$$\sigma = \nu - \nu_0 \tag{7}$$

In Eqs. (4)–(7), we have used the following notations: ρ_0 is the constant mass density; u_i is the component of the displacement field; φ_i is the component of the microrotation vector; ν is the volume distribution function, which in the reference state is ν_0; σ is a measure of the volume change of the bulk material; F_i is the component of the body forces; G_i is the component of the body couple; L is the extrinsic equilibrated body force; g is the intrinsic equilibrated force; t_{ij} is the component of the stress tensor; m_{ij} is the component of the couple stress tensor; h_i is the component of the equilibrated stress; k is the equilibrated inertia; I_{ij} is the coefficient of inertia; $\varepsilon_{ij}, \mu_{ij}$ are the kinematic characteristics of the strain; and ε_{ijk} is the alternating symbol;

Here, we outline the volume change of the bulk material results from void compaction or dilatation. Previously, the physical significances of the functions L, h, and k have been presented by Goodman and Cowin (1972) and Nunziato and Cowin (1983).

To the system of field Eqs. (4)–(7), we now add the boundary conditions in the following homogeneous form:

$$u_i(x,t) = 0, \quad \phi_i(x,t) = 0, \quad \sigma(x,t) = 0,$$
$$(x,t) \in \partial B \times [0,t_0] \tag{8}$$

and with the following initial conditions:

$$u_i(x,0) = a_i(x), \quad \dot{u}_i(x,0) = b_i(x), \quad \phi_i(x,0) = c_i(x)$$
$$\dot{\phi}_i(x,0) = d_i(x), \quad \sigma(x,0) = \sigma^0(x), \quad \dot{\sigma}(x,0) = \sigma^1(x),$$
$$\forall (x) \in B \tag{9}$$

where a_i, b_i, c_i, d_i, σ^0, and σ^1 are prescribed functions.

Substituting the constitutive Eqs. (6) and the geometric Eqs. (7) into Eqs. (4) and (5), we obtain the following system of coupled equations:

$$\rho_0\ddot{u}_i = [A_{ijmn}(u_{n,m} + \varepsilon_{nmk}\phi_k) + B_{ijmn}\phi_{n,m} + P_{ij}\sigma + Q_{ijk}\sigma_{,k}]_{,j} + \rho_0 F_i$$
$$I_{ij}\ddot{\phi}_j = [B_{ijmn}(u_{n,m} + \varepsilon_{nmk}\phi_k) + C_{ijmn}\phi_{n,m} + R_{ij}\sigma + S_{ijk}\sigma_{,k}]_{,j} + \varepsilon_{ijk}[A_{jkmn}(u_{n,m} + \varepsilon_{nms}\phi_s) + B_{jkmn}\phi_{n,m} + P_{jk}\sigma + Q_{jkr}\sigma_{,r}] + \rho_0 G_i$$
$$\rho_0\kappa\ddot{\sigma} = [Q_{mni}(u_{n,m} + \varepsilon_{nms}\varphi_s) + S_{mnI}\phi_{n,m} + d_i\sigma + A_{ij} \times \sigma_{,j}]_{,i} - P_{ij}(u_{j,i} + \varepsilon_{ijk}\phi_k) - R_{ij}\phi_{j,i} - \xi\sigma - d_i\sigma_{,i} + \rho_0 L \tag{10}$$

Next, we shall examine the existence and uniqueness of the solution and, also, the continuous dependence of the solution upon initial data, and we supply the terms for the initial-boundary value problem defined by Eqs. (10), boundary conditions (8), and the initial conditions (9).

3. MAIN RESULTS

In all what follows we shall use the following assumptions on the material properties:

- Assumption (i)

$$\rho_0 > 0,\ I_{ij} > 0,\ \kappa > 0$$

- Assumption (ii)

$$A_{ijmn}\xi_{ij}\xi_{mn} + 2B_{ijmn}\xi_{ij}\eta_{mn} + C_{ijmn}\eta_{ij}\eta_{mn} + 2P_{ij}\xi_{ij}\sigma + 2R_{ij}\eta_{ij}\sigma + 2Q_{ijs}\xi_{ij}\kappa_s + 2S_{ijs}\eta_{ij}\kappa_s + 2d_i\kappa_i\sigma + \xi\sigma^2 + A_{ij}\kappa_i\kappa_j \geq \alpha_0(\xi_{ij}\xi_{ij} + \eta_{ij}\eta_{ij} + \kappa_i\kappa_i + \sigma^2), \quad \alpha_0 > 0$$

for all arbitrary ξ_{ij}, η_{ij}, κ_i, and σ.

Assumptions (i) and (ii) are in agreement with the usual restrictions imposed in the mechanics of solids in order to obtain the existence and uniqueness of the solution. For instance, assumption (ii) assures that the internal energy density is a positive definite.

We shall use the following vectorial notations:

$$\mathbf{u} = (u_i), \quad \mathbf{v} = (v_i), \quad \phi = (\phi_i), \quad \psi = (\psi_i), \quad i = 1, 2, 3$$

And define space X by

$$X = \left\{ \frac{(\mathbf{u}, \mathbf{v}, \phi, \psi, \alpha)}{\mathbf{u} \in \mathbf{H}_0^1(B)}, \quad \mathbf{v} \in \mathbf{H}^0(B), \quad \phi \in \mathbf{H}_0^1(B), \quad \psi \in \mathbf{H}^0(B), \quad \sigma \in H_0^1(B), \quad \alpha \in H^0(B) \right\} \tag{11}$$

where $H_0^1(B)$ and $H^0(B)$ are the familiar Sobolev spaces (see Pazy, 1983). The following notations have been used:

$$\mathbf{H}_0^1(B) = \left[H_0^1(B)\right]^3, \ \mathbf{H}^0(B) = \left[H^0(B)\right]^3$$

We want to transform our initial-boundary value problem, given by Eqs. (10) and conditions (8) and (9) into a temporally homogeneous abstract equation in Hilbert space X defined in Eq. (11). Thus, we define the operators

$$A_i\mathbf{W} = v_i$$

$$B_i\mathbf{W} = \frac{1}{\rho_0}[A_{ijmn}(u_{n,m} + \varepsilon_{nmk}\phi_k) + B_{ijmn}\phi_{n,m} + P_{ij}\sigma + Q_{ijk}\sigma_{,k}]_{,j}$$

$$C_i\mathbf{W} = \psi_i$$

$$D_i\mathbf{W} = \frac{1}{I_{ij}}[B_{ijmn}(u_{n,m} + \varepsilon_{nmk}\phi_k) + C_{ijmn}\phi_{n,m} + R_{ij}\sigma + S_{ijk}\sigma_{,k}]_{,j} + \varepsilon_{nmk}[A_{jkmn}(u_{n,m} + \varepsilon_{nms}\phi_s) + B_{jkmn}\phi_{n,m} + P_{jk}\sigma + Q_{jkr}\sigma_{,r}]$$

$$E\mathbf{W} = \alpha$$

$$F\mathbf{W} = \frac{1}{\rho_0\kappa}\Big\{[Q_{mni}(u_{n,m} + \varepsilon_{nms}\phi_s) + S_{mni}\phi_{n,m} + d_i\sigma + A_{ij}\sigma_{,j}]_{,i} - P_{ij}(u_{j,i} + \varepsilon_{ijk}\varphi_k) - R_{ij}\phi_{j,i} - \xi\sigma - d_i\sigma_{,i}\Big\} \tag{12}$$

Let $\mathcal{L}$ be the following operator:

$$\mathcal{L} = (\mathbf{AW}, \mathbf{BW}, \mathbf{CW}, \mathbf{DW}, E\mathbf{W}, F\mathbf{W}) \tag{13}$$

where $\mathbf{A} = (A_i)$, $\mathbf{B} = (B_i)$, $\mathbf{C} = (C_i)$, and $\mathbf{D} = (D_i)$, $i = 1, 2, 3$. The domain of the operator $\mathcal{L}$ is

$$D = D(\mathcal{L}) = \left\{ \frac{\mathbf{W} \in X}{\mathcal{L}\mathbf{W} \in \mathrm{X}}, \quad \mathbf{v} = 0, \quad \psi = 0, \quad \alpha = 0 \quad \text{on} \quad \partial B \right\} \tag{14}$$

The closure of $D(\mathcal{L})$ is obviously space X, and hence, $D(\mathcal{L})$ is dense in X. Also, it is easy to see that the domain $D(\mathcal{L})$ is not empty because it at least contains $[C_0^\infty(B)]^7$. Thus, we can reduce the initial-boundary value problems (10), (8), and (9) to the temporally equation on Hilbert space X

$$\frac{d\mathbf{W}}{dt} = \mathcal{L}\mathbf{W} + \mathcal{F}(t), \quad 0 \leq t \leq t_0 \tag{15}$$

with the initial condition

$$\mathbf{W}(0) = \mathbf{W}_0 \tag{16}$$

where

$$\mathcal{F}(t) = \left(\mathbf{0}, \mathbf{F}, \mathbf{0}, \mathbf{G}, \mathbf{0}, \frac{1}{\kappa}L\right), \quad \mathbf{W}_0 = (\mathbf{a}, \mathbf{b}, \mathbf{c}, \mathbf{d}, \sigma^0, \sigma^1)$$

$$\mathbf{F} = (\rho_0 F_i), \quad \mathbf{G} = (\rho_0 G_i), \quad \mathbf{a} = (a_i), \quad \mathbf{b} = (b_i), \quad \mathbf{c} = (c_i), \quad \mathbf{d} = (d_i)$$

Let X^* be the Hilbert space equipped with the norm induced by the inner product

$$< \mathbf{W}, \mathbf{W} >_* = \int_B [\rho_0\nu_i\bar{\nu}_i + I_{ij}\psi_i\bar{\psi}_i + \rho_0\kappa\alpha\bar{\alpha} + A_{ijmn} \times \varepsilon_{ij}\bar{\varepsilon}_{mn} + C_{ijmn}\mu_{ij}\bar{\mu}_{mn} + B_{ijmn}(\varepsilon_{ij}\bar{\mu}_{mn} + \bar{\varepsilon}_{ij}\mu_{mn}) + P_{ij}(\varepsilon_{ij}\bar{\sigma} + \bar{\varepsilon}_{ij}\sigma) + R_{ij}(\mu_{ij}\bar{\sigma} + \bar{\mu}_{ij}\sigma) + Q_{ijk}(\varepsilon_{ij}\bar{\sigma}_{,k} + \bar{\varepsilon}_{ij}\sigma_{,k}) + S_{ijk}(\mu_{ij}\bar{\sigma}_{,k} + \bar{\mu}_{ij}\sigma_{,k}) + d_i(\sigma\bar{\sigma}_{,i} + \bar{\sigma}\sigma_{,i}) + A_{ij}\sigma_{,i}\bar{\sigma}_{,j} + \xi\sigma\bar{\sigma}]\, dV \tag{17}$$

By taking into account hypotheses (i) and (ii) imposed on the material properties, we obtain

$$|\mathbf{W}|_*^2 =< \mathbf{W}, \mathbf{W} >_* = \int_B [\rho_0 \nu_i \nu_i + I_{ij}\psi_i\psi_i + \rho_0 \kappa \alpha^2 + A_{ijmn}\varepsilon_{ij}\varepsilon_{mn} + 2B_{ijmn}\varepsilon_{ij}\mu_{mn} + C_{ijmn}\mu_{ij}\mu_{mn} + 2P_{ij} \times \varepsilon_{ij}\sigma + 2R_{ij}\mu_{ij}\sigma + 2Q_{ijk}\varepsilon_{ij}\sigma_{,k} + 2S_{ijk}\mu_{ij}\sigma_{,k} + 2d_i \times \sigma\sigma_{,i} + A_{ij}\sigma_{,i}\sigma_{,j} + \xi\sigma^2]\, dV \geq \int_B [\rho_0 \nu_i \nu_i + I_{ij}\psi_i\psi_j + \rho_0 \kappa \alpha^2 + \alpha_0(\varepsilon_{ij}\varepsilon_{ij} + \mu_{ij}\mu_{ij} + \sigma^2 + \sigma_{,i}\sigma_{,i})] \times dV \geq c_1 \, |\mathbf{W}|_X^2 \tag{18}$$

On the other hand, using the first Korn inequality and Eq. (17), we deduce the inequality

$$|\mathbf{W}|_*^2 \leq c_2 \, |\mathbf{W}|_X^2$$

From this inequality and taking into account Eq. (18), we obtain

$$c_1 \, |\mathbf{W}|_X^2 \leq |\mathbf{W}|_*^2 \leq c_2 \, |\mathbf{W}|_X^2$$

hence, the norm $|.|_*$ is equivalent to the original norm in Hilbert space X.

3.1 Lemma 1

The operator $\mathcal{L}$ is dissipative, that is

$$\langle \mathcal{L}\mathbf{W},\ \mathbf{W} \rangle_* \ \leq\ 0, \quad \text{for all} \quad \mathbf{W} \in D(\mathcal{L})$$

3.2 Proof

According to relations (12), we have

$$< \mathcal{L}\mathbf{W},\ \mathbf{W} >_* = \int_B \Big\{ \nu_i [A_{ijmn}(u_{n,m} + \varepsilon_{mnk}\phi_k) + B_{ijmn} \times \phi_{m,n} + P_{ij}\sigma + Q_{ijk}\sigma_{,k}]_{,j} + \psi_i [B_{ijmn}(u_{n,m} + \varepsilon_{nmk}\phi_k) + C_{ijmn}\phi_{n,m} + R_{ij}\sigma + S_{ijk}\sigma_{,k}]_{,k} + \psi_i \varepsilon_{ijk} [A_{jkmn} \times (u_{n,m} + \varepsilon_{nms}\phi_s) + B_{jkmn}\phi_{n,m} + P_{jk}\sigma + Q_{jkr}\sigma_{,r}] + \alpha \times [Q_{mni}(u_{m,n} + \varepsilon_{nms}\phi_s + S_{mni}\phi_{n,m} + d_i\sigma + A_{ij}\sigma_{,j}]_{,i} - \alpha [P_{ij}(u_{j,i} + \varepsilon_{ijk}\phi_k) + R_{ij}\phi_{j,i} + \xi\sigma + d_i\sigma_{,i}] + A_{ijmn} \times (u_{n,m} + \varepsilon_{nmk}\phi_k)(v_{j,i} + \varepsilon_{jis}\psi_s) + C_{ijmn}\psi_{n,m}\phi_{j,i} + B_{ijmn} \times [(u_{j,i} + \varepsilon_{jis}\phi_s)\psi_{n,m} + (\nu_{n,m} + \varepsilon_{nms}\psi_s)\phi_{j,i}] + P_{ij} \times [(u_{j,i} + \varepsilon_{ijs}\phi_s)\alpha + (\nu_{j,k} + \varepsilon_{ijs}\psi_s)\sigma] + R_{ij}(\phi_{j,i}\alpha + \psi_{j,i}\sigma) + Q_{ijk}[(u_{j,i} + \varepsilon_{jis}\phi_s)\alpha_{,k} + (\nu_{j,i} + \varepsilon_{jis}\psi_s)] + S_{ijk}(\phi_{j,i}\alpha_{,k} + \psi_{j,i}\sigma_{,k}) + d_i(\sigma\alpha_{,i} + \alpha\sigma_{,i}) + \xi\sigma\alpha + A_{ij}\sigma_{,i}\alpha_{,i} \Big\}\, dV$$

Making use of the Green-Gauss formula and boundary condition (8), we obtain the desired result.

3.3 Lemma 2

The operator $\mathcal{L}$ satisfies the range condition, that is

$$R(\lambda I - \mathcal{L}) = X, \quad \lambda > 0 \tag{19}$$

3.4 Proof

Assume that $\tilde{\mathbf{W}} = \left(\tilde{\mathbf{u}},\ \tilde{\mathbf{v}},\ \tilde{\varphi},\ \tilde{\psi},\ \tilde{\sigma},\ \tilde{\alpha}\right) \in X$. Then, we have to show that for all $\tilde{\mathbf{W}} \in X$, the equation

$$\lambda\mathbf{W} - \mathcal{L}\mathbf{W} = \tilde{\mathbf{W}} \tag{20}$$

has at least a solution $\mathbf{W}$ in $D(\mathcal{L})$. By eliminating the functions v_i, ψ_i, and α from Eq. (20), we obtain the following system of equations in the variables u_i, ϕ_i, and σ:

$$L_i\omega \equiv \lambda^2 u_i - \frac{1}{\rho_0}[A_{ijmn}(u_{n,m} + \varepsilon_{nmk}\phi_k) + B_{ijmn}\phi_{n,m} + P_{ij}\sigma + Q_{ijk}\sigma_{,k}]_{,j} = g_i$$

$$L_{i+3}\omega \equiv \lambda^2\phi_i - \frac{1}{I_{ij}}[B_{ijmn}(u_{n,m} + \varepsilon_{nms}\phi_s) + C_{ijmn} \times \phi_{n,m} + R_{ij}\sigma + S_{ijk}\sigma_{,k}]_{,j} + \varepsilon_{ijk}[A_{jkmn}(u_{n,m} + \varepsilon_{nms} \times \phi_s) + B_{jkmn}\phi_{n,m} + P_{jk}\sigma + Q_{jkr}\sigma_{,r}] = g_{i+3}$$

$$L_7\omega \equiv \lambda^2\sigma - \frac{1}{\rho_0\kappa}[Q_{mni}(u_{n,m} + \varepsilon_{nms}\phi_s) + S_{mni}\phi_{n,m} + d_i\sigma + A_{ij}\sigma_{,j}]_{,i} + \frac{1}{\rho_0\kappa}[P_{ij}(u_{j,i} + \varepsilon_{ijs}\phi_s) + R_{ij}\phi_{j,i} + \xi\sigma - d_i\sigma_{,i}] = g_7 \tag{21}$$

where

$$\begin{aligned} &\omega = (u,\ \phi,\ \sigma),\ g_i = \lambda\tilde{u}_i + \tilde{v}_i,\ i = 1,2,3 \\ &g_{i+3} = \lambda\tilde{\phi}_i + \tilde{\psi}_i,\ i = 1,2,3,\ \ g_7 = \lambda\tilde{\sigma} + \tilde{\alpha} \end{aligned} \tag{22}$$

We will denote by $\langle .,. \rangle$ the conveniently weighted $[L_2(B)]^7$ inner product and we consider the bilinear form

$$\begin{aligned} &Q\left[\omega, \bar{\omega}\right] = \langle L\omega, \bar{\omega} \rangle = \langle (L_i\omega, L_i + 3\omega, L_7\omega)\,, \\ &(\bar{u}_i, \bar{\varphi}_i, \bar{\sigma}) \rangle = \int_B \bar{u}_i L_i\omega + I_{ij}\bar{\psi}_j L_{i+3}\omega + \rho_0\kappa\bar{\sigma}L_7\omega] \\ &\times dV \end{aligned} \tag{23}$$

Using the Green–Gauss formula and boundary conditions (8), we obtain the following:

$$Q[\omega, \omega] = \int_B [\rho_0\lambda^2 u_i u_i + I_{ij}\lambda^2\varphi_i\varphi_j + \rho_0\kappa\lambda^2\sigma^2]\, dV + \int_B [A_{ijmn}(u_{n,m} + \varepsilon_{nmk}\varphi_k)(u_{j,i} + \varepsilon_{jis}\varphi_s) + C_{ijmn} \times \varphi_{n,m}\varphi_{j,i} + 2B_{ijmn}(u_{j,i} + \varepsilon_{jis}\phi_s)\phi_{n,m} + 2P_{ij}(u_{j,i} + \varepsilon_{jis}\phi_s)\sigma + 2R_{ij}\phi_{j,i}\sigma + 2d_i\sigma\sigma_{,i} + A_i\sigma_{,i}\sigma_{,j}]\, dV \tag{24}$$

for any $\omega = (\mathbf{u},\ \varphi,\ \sigma) \in Y$, where $Y \equiv \mathbf{H}_0^1(B) \times \mathbf{H}_0^1(B) \times H_0^1(B)$.

Due to hypotheses (i) and (ii) and the first Korn's inequality, it follows that

$$Q\,[\,\omega,\bar{\omega}] \geq C_1|\omega|_Y^2,\ \text{ for all }\ \omega=(\mathbf{u},\varphi,\sigma)\in Y \quad (25)$$

where C_1 is a positive, conveniently chosen, constant and the norm $|\omega|_Y$ is defined by

$$|\omega|_Y = |(\mathbf{u},\ \phi,\ \sigma)|_Y = |\mathbf{u}|_{\mathbf{H}^1(B)}+|\phi|_{\mathbf{H}^1(B)}+|\sigma|_{H^1(B)}$$

In the usual way, we can prove that

$$Q\ [\omega,\ \omega\,]\ \leq\ C_2|\omega|_Y^2,\ \text{ for all }\ \omega=(\mathbf{u},\ \varphi,\ \sigma)\in Y$$

Hence, bilinear form $Q\,[\omega,\ \omega]$ determines a norm equivalent to the original norm on space Y. Since bilinear form $Q\,[\omega,\ \bar{\omega}]$ is continuous on space $Y\times Y$, we find that there exists a linear bounded transformation T from Y to itself such that

$$Q\,[\omega,\bar{\omega}]=\langle\omega,\ T\bar{\omega}\rangle_Y\,,\ \text{ for any }\ \omega,\ \bar{\omega}\in Y \quad (26)$$

since

$$\langle\omega,\ T\bar{\omega}\rangle_Y = Q\ [\,\omega,\ \bar{\omega}\,]\geq C_1\,|\omega|_Y^2 \quad (27)$$

we deduce that

$$|T\omega|\ \geq\ C_1|\omega|_Y,\ \ \omega\in Y \quad (28)$$

Let $R(T)$ be the range of T. The linear transformation T is 1 to 1. For this, we have to prove that $\omega = 0$ results from $T\omega = 0$. Indeed, if there exists $\omega_0 \in Y$ such that $T\omega_0 = 0$, then Eq. (26) implies that $Q\ [\,\omega_0,\ \omega_0\,] = 0$, and then inequality (27) shows that $\omega_0 = 0$. Therefore, there exists

$$T^{-1} : R(T) \to Y$$

Now, we prove that $R(T)$ is dense in the space Y. We assume the contrary; that is, there exists $\omega_0 \in Y\backslash R(T)$, $\omega_0 \neq 0$ such that $\langle\omega_0,\ T\,\bar{\omega}_0\rangle_Y = 0$. But from Eq. (26) it follows that $Q\ [\,\omega_0,\ \omega_0\,] = 0$. Making use of Eq. (25), we obtain $\omega_0 = 0$. This contradicts the initial assumptions, and therefore, we find that $R(T)$ is dense in Y.

So, we extend T^{-1} to whole space Y, such that $T^{-1} : Y \to Y,\ |T^{-1}|\ \leq\ C_1$.

Let $\mathbf{z}$ be in $R(T)$ and ω be the only function in Y such that $\mathbf{z} = T\omega$.

We define functional κ by

$$\kappa(\mathbf{z})\ =\ \langle\mathbf{g},\omega\rangle$$

Obviously, we have

$$|\kappa(\mathbf{z})|\ \leq\ |\mathbf{g}|_{\mathbf{H}_0^{-1}(B)}\,|\omega|_Y\ \leq\ C^{-1}|\mathbf{g}|_{\mathbf{H}_0^{-1}(B)}\,|\mathbf{z}|_Y$$

and then we deduce that κ is a linear bounded functional defined over $R(T)$ such that

$$|\kappa|\ \leq\ C_1^{-1}|\mathbf{g}|_{\mathbf{H}_0^{-1}(B)}$$

We can extend κ to whole space Y in such a way that extended functional K will have the same norm.

On the other hand, since Y is a Hilbert space, the Riesz–Frechet theorem shows that there exists a unique $\omega \in Y$ such that

$$\begin{array}{l} K\,(\tilde{\omega})\ =\ \langle\omega,\ \tilde{\omega}\rangle_Y\,,\ \forall\ \tilde{\omega}\in Y \\ |\omega|_Y\ =\ |K|\ \leq\ C_1^{-1}|\mathbf{g}|_{\mathrm{H}_0^{-1}(B)} \end{array} \quad (29)$$

If we choose $\tilde{\omega} = T\tilde{\omega}$, then from Eqs. (26) and (29), it follows that $\omega \in Y$ is the unique solution of the equation

$$Q\,[\omega,\tilde{\omega}] = \langle\mathbf{g},\tilde{\omega}\rangle\,,\forall\tilde{\omega}\in Y \quad (30)$$

From the relations $\lambda u_i - \tilde{u}_i\ =\ v_i$, $\lambda\phi_i - \tilde{\phi}_i\ =\ \psi_i$, and $\lambda\sigma - \tilde{\sigma}\ =\ \alpha$, it follows that $\mathbf{v}\ \in\ \mathbf{H}_0^1(B)$, $\psi\ \in\ \mathbf{H}_0^1(B)$, and $\alpha\ \in\ H_0^1(B)$. Therefore, we deduce that $\mathbf{W}\ =\ (\mathbf{u},\ \mathbf{v},\ \phi,\ \psi,\ \sigma,\ \alpha)$ is in $D(\mathcal{L})$ and the proof of Lemma 2 is complete.

3.5 Theorem 1

Operator $\mathcal{L}$ defined by the relation (13) generates a C_0; i.e., a semigroup of contractions on space X.

3.6 Proof

This result follows immediately from the Lumer–Phillips corollary of the Hille–Yosida theorem, (see, for example, Pazy, 1983).

In order to study the existence and the uniqueness of the solution for inhomogeneous Eq. (15), we shall need the following result.

3.7 Theorem 2

Let $\mathcal{L}$ be the infinitesimal generator of a C_0; i.e., contractions semigroup $T(t)$ on space X. If $\mathcal{F}(s)$ is a continuously differentiable function on $[0,\ t_0]$, then initial value problems (15) and (16) have for every $\mathbf{W}_0\ \in\ D(\mathcal{L})$ the unique solution

$$\mathbf{W}(t)=T(t)\mathbf{W}_0+\int_0^t T(t-s)\mathcal{F}(s)ds,\quad t\in[0,t_0] \quad (31)$$

such that

$$\mathbf{W}(t) \in C^1\ ([\,0,\ t_0\,]\ ;\ X)\ \cap\ C^0\ ([\,0,\ t_0\,]\ ;\ D(\mathcal{L}))$$

On the basis of the above theorem, we obtain the following results.

3.8 Theorem 3

Suppose that the elastic coefficients are continuously differentiable functions that satisfy conditions (1) and (ii). Moreover, we assume that

$$\mathbf{F} \in C^1\,([0,t_0];\mathbf{L}_2(B)),\ \mathbf{G} \in C^1([0,t_0];\mathbf{L}_2(B)),$$
$$L \in C^1\,([0,\ t_0]\ ;\ L_2(B))$$

Also, we suppose that $\mathbf{W}_0 = (\mathbf{a},\ \mathbf{b},\ \mathbf{c},\ \mathbf{d}, \sigma^0,\ \sigma^1) \in D(\mathcal{L})$.

Then, there exists a unique solution of the problem given by Eqs. (10), (8), and (9), such that

$$(\mathbf{u}, \dot{\mathbf{u}}, \phi, \dot{\phi}, \sigma, \dot{\sigma}) \in [C^1([0,t_0];X) \cap C^0 \times ([0,t_0];D(L))]^{14}$$

The following theorem establishes the continuous dependence of solution of our initial-boundary value problem upon the initial data and supply terms.

Let $(u_i,\ \phi_i,\ \sigma)$ be the difference of two solutions of the problem defined by Eqs. (10), (8), and (9), corresponding to the difference of the initial data and the difference of body force, body couple, and equilibrated extrinsic force $\mathbf{W}_0 = \big(\mathbf{a},\ \mathbf{b},\ \mathbf{c},\ \mathbf{d},\ \sigma^0,\ \sigma^1\big)$, $(\mathbf{F},\ \mathbf{G},\ \mathbf{L})$, respectively.

3.9 Theorem 4

Suppose that the elastic coefficients are continuously differentiable functions that satisfy conditions (i) and (ii). Moreover, we assume that

$$\mathbf{F},\ \mathbf{G} \in L_1\ ([\,0,\ t_0\,]\ ;\ \mathbf{L}_2(B))\,,\ L \in L_1 \times ([\,0,\ t_0\,]\ ;\ L_2(B))$$

and

$$\mathbf{a} \in \mathbf{H}^1(B),\ \mathbf{b} \in \mathbf{H}^0(B),\ \mathbf{c} \in \mathbf{H}^1(B),\ \mathbf{d} \in \mathbf{H}^0(B),$$
$$\sigma^0 \in H^1(B),\ \sigma^1 \in H^0(B)$$

If $(\mathbf{u},\ \phi,\ \sigma)$ is the difference of two solutions for problems (10), (8), and (9), then there exists a positive constant M such that

$$|\mathbf{u}|_{\mathbf{H}^1(B)} + |\dot{\mathbf{u}}|_{\mathbf{H}^0(B)} + |\phi|_{\mathbf{H}^1(B)} + |\dot{\phi}|_{\mathbf{H}^0(B)} + |\sigma|_{H^1(B)} + |\dot{\sigma}|_{H^0(B)} \le M \Big\{ |\mathbf{a}|_{\mathbf{H}^1(B)} + |\mathbf{b}|_{\mathbf{H}^0(B)} + |\mathbf{c}|_{\mathbf{H}^1(B)} + |\mathbf{d}|_{\mathbf{H}^0(B)} + |\sigma^0|_{H^1(B)} + |\sigma^1|_{H^0(B)} + \int_0^t [|\mathbf{F}(\tau)|_{H_0(B)} + |\mathbf{G}(\tau)|_{\mathbf{H}^0(B)} + |L(\tau)|_{H^0(B)}]\, d\tau \Big\} \tag{32}$$

3.10 Proof

On the basis of the Eqs. (10) and conditions (8) and (9), we can deduce the following identity:

$$\int_B [\rho_0 \dot{u}_i \dot{u}_i + I_{ij}\dot{\phi}_i\dot{\phi}_j + \rho_0 \kappa \dot{\sigma}_2]\, dV + \int_B [A_{ijmn}(u_{n,m} + \varepsilon_{nmk}\phi_k)(u_{j,i} + \varepsilon_{jis}\phi_s) + C_{ijmn}\phi_{n,m}\phi_{j,i} + 2B_{ijmn} \times (u_{j,i} + \varepsilon_{jis}\phi_s)\phi_{n,m} + 2P_{ij}(u_{j,i} + \varepsilon_{jis}\phi_s)\sigma + 2R_{ij} \times \phi_{j,i}\sigma + 2d_i\sigma\sigma_{,i} + A_{ij}\sigma_{,i}\sigma_{,j}]dV = \int_B [\rho_0 \dot{\alpha}_i\dot{\alpha}_i + I_{ij}\dot{c}_i\dot{c}_j + \rho_0\kappa(\dot{\sigma}^0)^2]dV + \int_B [A_{ijmn}(\alpha_{n,m} + \varepsilon_{nmk}c_k)(\alpha_{j,k} + \varepsilon_{jis}c_s) + C_{ijmn}c_{n,m}c_{j,i} + 2B_{ijmn}(\alpha_{j,i} + \varepsilon_{jis}c_s)c_{n,m} + 2P_{ij} \times (\alpha_{j,i} + \varepsilon_{jis}c_s)\sigma^0 + 2R_{ij}c_{j,i}\sigma^0 + 2d_i\sigma^0\sigma^0_{,i} + A_{ij}\sigma^0_{,i} \times \sigma^0_{,j}]\, dV + 2\int_0^t \int_B \rho_0 [F_i u_i + G_i\phi_i + L\sigma]\, dV\, d\tau \tag{33}$$

By using the Schwarz's inequality, hypotheses (i) and (ii), and the first Korn's inequality, from identity (33) we obtain a Gronwall-type inequality that proves desired estimate (32).

4. CONCLUSION

Because of the elegance of the theory of semigroups of linear operators, we can derive the existence, uniqueness, and the continuous dependence of the solution without recourse to supplementary restrictions.

A similar procedure can be used in the case when boundary conditions (8) are replaced by other boundary conditions. The above results are true.

REFERENCES

Fichera, G., Existence theorems in elasticity, *Handbuch der Physik*, vol. VI a-2, Berlin: Springer Verlag, 1972.

Goodman, M. A. and Cowin, S. C., A theory for granular materials, *Arch. Ration. Mech. Anal.*, vol. **44**, pp. 249–266, 1972.

Iesan, D., A theory of thermoelastic materials with voids, *Acta Mech.*, vol. **60**, pp. 67–89, 1986.

Marin, M., Sur l'existence dans la thermoelasticite des milieux micropolaires, *Acad. Sci., Paris, C. R.*, vol. **321**, ser. II.b, pp. 475–480, 1995.

Marin, M., On weak solution in elasticity of dipolar bodies, *J. Comp. Appl. Math.*, vol. **82**, pp. 291–297, 1997.

Marin, M., On the minimum principle for dipolar materials with stretch, *Nonlinear Analysis: Real World Applic.*, vol. **10**, pp. 1572–1578, 2009.

Nunziato, J. W. and Cowin, S. C., Linear elastic materials with voids, *J. Elast.*, vol. **13**, pp. 125–147, 1983.

Pazy, A., *Semigroups of Linear Operators and Applications*, Berlin: Springer, 1983.

Journal of Porous Media 13(12), 1111–1117 (2010)

A NOTE ON THE DARCY–FORCHHEIMER–BRINKMAN EQUATION FOR FULLY DEVELOPED FLOW THROUGH A POROUS CHANNEL BOUNDED BY FLAT PLATES

A. R. Ansari[1,*] *& A. M. Siddiqui*[2]

[1]*Department of Mathematics and Natural Sciences, Gulf University for Science and Technology, Hawally 32093, Kuwait*

[2]*Department of Mathematics, York Campus, Pennsylvania State University, York, PA 17403, USA*

[*]Address all correspondence to A. R. Ansari E-mail: Ansari.a@gust.edu.kw

Original Manuscript Submitted: 5/22/2009; Final Draft Received: 7/7/2009

We consider the fully developed flow through straight porous channels, where the flow entry profiles are Poiseulle–Couette combinations. In particular, we use the Darcy–Forchheimer–Brinkman equation as the model governing the plane parallel flow through the porous medium. In the past, this particular model has been solved using numerical methods due to its nonlinear nature. We present an analytical solution of the problem employing an emerging perturbation technique, which has been proven to be successful in tackling nonlinear problems. We offer various verifications of the solution by comparing to existing, documented results and also mathematically, through reduction to simpler problems.

KEY WORDS: *Darcy–Forchheimer–Brinkman equation, analytical method, Poiseulle entry profile, Couette entry profile*

1. INTRODUCTION

The study of flow through porous media has received considerable attention due to its many faceted practical applications. In irrigation processes, the movement of fertilizers, pollutants, and nutrients into plants are all examples of flow through porous media. The study of the interaction of oil, gas, and water through porous earth layers has become more important because of the increasing demands for energy. It has also found applications in the biological sciences, particularly in biomechanics. One such application is in the human lungs, which are idealized as layers of flocs and other types of porous materials (Hamdan, 1994). The flow of a fluid through a porous medium is essentially a two-phase flow that consists of the flow of a matrix particle phase and a fluid phase. However, the particle phase is usually considered as a solid matrix that is rigid, and hence, assumed to be stationary. Therefore, effectively the flow through the porous matrix boils down to the flow of a single-phase fluid. The importance of such flows is clear from some of the applications mentioned above. Solutions of the problems are of fundamental importance.

In this study, we consider one such model of fully developed flow through a porous medium, between parallel plates, where the governing equation is the well-known Darcy–Forchheimer–Brinkman (DFB) equation. The entry profiles are taken to be Poiseuille, Couette. and Poiseuille–Couette type. It is well known that the DFB equation is nonlinear and usually solved by numerical methods (Awartani and Hamdan, 2005). We note that the problem of forced convection flow in porous medium where the DFB equation has been employed to represent the fluid has been solved analytically as well; however, the approach there involves using velocity profiles that have been attained using singular perturbation methods

1091–028X/10/$35.00

NOMENCLATURE

p	pressure	ρ	fluid density
u	averaged velocity in the x direction	C_d	drag coefficient
v	averaged velocity in the y direction	ζ, χ	binary parameters that take the values 0, 1, respectively
k	permeability		
μ	viscosity	ϑ	μ_{eff}/μ
μ_{eff}	effective viscosity of the fluid in the medium	C	$p_X/(\rho U_\infty)^2$
		R	$\rho U_\infty L/\mu$, the Reynolds number

(Marafie and Vafai, 2001). We present an analytical solution of the problem employing the homotopy perturbation method (HPM) (He, 1999). This technique has been used successfully in solving many nonlinear differential equations in different fields of applied mathematics. In fluid mechanics for instance, Siddiqui et al. (2006a,b, 2008a,b) used this method for solving nonlinear problems involving Newtonian and non-Newtonian fluids. For a comprehensive account of the use of the HPM to successfully solve problems in fluid mechanics, see He (2006a,b). It is worth noting that recently the convergence of the HPM has been addressed and analyzed by Biazar and Ghazvini (2009).

Therefore, in essence, here we basically take an established worthwhile problem (Awartani and Hamdan, 2005), and present an analytical solution to the problem. We offer verification of the solution by reducing it to the simpler Darcy–Lapwood–Brinkman (DLB) model and showing that the solution reduces correctly as well. We also compare the solutions for the three scenarios of entry flows to the numerical solution of Awartani and Hamdan (2005). In addition, we note that Kuznetsov (1998) has solved a similar problem analytically with a Couette entry profile; also, Nield et al. (1996) have solved a similar problem with a Poiseulle entry profile. However, in both cases the velocity profiles are computed using numerical solutions. Furthermore, Pantokratoras (2007a,b) has solved a similar problem with both types of entry profiles, but once again, numerical methods for their solution have been employed. We mention this to point out that the solution computed here is not unique or new, rather the method used is an analytical approximate method that is simple to employ. In addition, the problem we set up consists of very general boundary conditions and offers flexibility to the user of these results.

2. PROBLEM FORMULATION

We start with the basic fact that the flow of a viscous fluid is governed by the continuity and the Navier–Stokes equations that, when the fluid is incompressible and the flow is steady, take the form

$$\nabla \cdot \mathbf{v} = 0 \tag{1}$$

$$\rho\left(\mathbf{v}\cdot\nabla\right)\mathbf{v} = -\nabla p + \mu\nabla^2\mathbf{v} \tag{2}$$

In Eqs. (1) and (2), $\mathbf{v}$ is the velocity vector, μ is the viscosity, ρ is the density, and p is the pressure. As our objective is to consider the flow through a porous structure we need to introduce this. Of course, this in itself is not an easy task; it is very difficult to describe the porous matrix boundaries. This is due to the complexity of the pores and the matrix structures. It is the norm now to analyze such problems with respect to the mathematical description of the macroscopic features of the flow of the fluid, and discounting the microscopic features. The introduction of the volume averaging theorems (Hamdan, 1994) has helped considerably in this regard.

In accordance with the above-mentioned averaging approach, we express the conservation of mass principle as a macroscopic continuity equation, which is similar to Eq. (1). The macroscopic momentum equations, depending on the type of the porous medium and the flow under consideration, can be expressed through the following general equation (Hamdan, 1994):

$$\begin{aligned}&\rho\left\{\chi[\zeta-1]+1\right\}\left(\mathbf{v}\cdot\nabla\right)\mathbf{v} = -\nabla p + \mu_{\text{eff}}\\ &\times\left\{\chi[\vartheta-1]+1\right\}\nabla^2\mathbf{v} - \chi\left\{\frac{\mu}{k}\mathbf{v} + \frac{\rho C_d}{\sqrt{k}}\mathbf{v}|\mathbf{v}|\right\}\end{aligned} \tag{3}$$

where $\mathbf{v}$ is the velocity vector, p is the fluid pressure, ρ is the fluid density, μ is the fluid viscosity, μ_{eff} is the viscosity of the fluid in the porous medium, $\vartheta = \mu_{\text{eff}}/\mu$, k

is the permeability, C_d is the drag coefficient, and ζ and χ are both binary parameters that take the values 0 and 1. Note that when $\chi = 0$ Eq. (3) reduces to Navier–Stokes Eq. (2); when $\chi = 1$ the flow is in the porous medium; of course, the various types of porous media can be specified by the choice of the parameter ζ (Hamdan, 1994).

In the analysis in this paper we consider the flow to be in two dimensions, hence Eq. (3) takes the following component form:

$$\rho\left\{\chi[\zeta-1]+1\right\}(uu_x+vu_y) = -p_x+\mu_{\text{eff}} \times\left\{\chi[\vartheta-1]+1\right\}\nabla^2 u-\chi\left\{\frac{\mu}{k}u+\rho C_d u\sqrt{\frac{u^2+v^2}{k}}\right\} \quad (4)$$

$$\rho\left\{\chi[\zeta-1]+1\right\}(uv_x+vv_y) = -p_y+\mu_{\text{eff}} \times\left\{\chi[\vartheta-1]+1\right\}\nabla^2 v-\chi\left\{\frac{\mu}{k}v+\rho C_d v\sqrt{\frac{u^2+v^2}{k}}\right\} \quad (5)$$

We will consider the flow to be plane, parallel, and fully developed through a straight channel, which means that

$$\begin{aligned} &u = u(y); \quad p = p(x); \\ &u_x = u_{xx} = v = v_x = v_{xx} = p_y = 0 \end{aligned} \quad (6)$$

These relations [Eq. (6)], automatically satisfy continuity Eq. (1) and y-momentum Eq. (5), and reduce x-momentum Eq. (4) to

$$\begin{aligned} &-p_x+\mu_{\text{eff}}\left\{\chi[\vartheta-1]+1\right\}u_{yy}-\chi \\ &\times\left\{\frac{\mu}{k}u+\frac{\rho C_d u|u|}{\sqrt{k}}\right\}=0 \end{aligned} \quad (7)$$

We introduce a characteristic length L and a free-stream characteristic velocity U_∞, which enable us to nondimensionalize Eq. (7) employing the definitions

$$x^* = x/L, \;\; y^* = y/L, \;\; u^* = u/U_\infty, \;\; k^* = k/L^2 \quad (8)$$

Substituting Eq. (8) into Eq. (7), and eliminating the asterisks and rearranging, Eq. (7) takes the following dimensionless form when $\mu = \mu_{\text{eff}}$:

$$\left\{\chi[\vartheta-1]+1\right\}u_{yy} = RC+\chi\left\{\frac{u}{k}+\frac{RC_d}{\sqrt{k}}u^2\right\} \quad (9)$$

where $C = \left[p_X/(\rho U_\infty)^2\right]$ and Reynolds number $R = (\rho U_\infty L/\mu)$.

At this point we get more specific since we are interested in the DFB equation. Taking $\chi = \vartheta = 1$ and $\zeta = 0$, we have

$$u_{yy} = RC+\frac{u}{k}+\frac{RC_d}{\sqrt{k}}u^2 \quad (10)$$

We assume the following boundary conditions

$$u(0) = a, \quad u(1) = b \quad (11)$$

where a and b simply take values of either 0 or 1. These boundary conditions give us a lot of flexibility, allowing us to represent the different entry profiles that are of interest to us. The cases we will explore are:

1. For Poiseuille flow we have $a = b = 0$ and $C \neq 0$.
2. For Couette flow we have $a = 0$ and $b = 1$, with $C = 0$.
3. For Poiseuille–Couette flow we again set $a = 0$ and $b = 1$, with $C \neq 0$.

In the next section we will solve the more general problem keeping the boundary conditions as in Eq. (11).

3. SOLUTION OF THE PROBLEM USING THE HOMOTOPY PERTURBATION METHOD

The HPM approach requires that we start by first defining a homotopy $w(y,q) : \Omega \times [0,1] \to R$ for Eq. (10), which satisfies the equation

$$\begin{aligned} &\frac{\partial^2 w}{\partial y^2}-\kappa^2 w-RC-(1-q)\left[\frac{\partial^2 u_0}{\partial y^2}-\kappa^2 u_0-RC\right] \\ &-qRC_d\kappa w^2 = 0 \end{aligned} \quad (12)$$

where $q \in [0,1]$ is the embedding parameter, u_0 is the initial guess approximation, and $\kappa = 1/\sqrt{k}$ is introduced for notational convenience. Note that when $q = 0$ we have a simple linear problem to solve and as $q \to 1$, the linear equation deforms to the equation we wish to solve.

We assume that the initial guess approximation of Eq. (10) subject to the boundary conditions [Eq. (11)] is

$$u_0(y) = \alpha\cosh(\kappa y)+\beta\sinh(\kappa y)-\frac{RC}{\kappa^2} \quad (13)$$

where

$$\alpha = a+\frac{RC}{\kappa^2} \quad (14)$$

$$\beta = \frac{1}{\sinh\kappa}\left[b-\left(a+\frac{RC}{\kappa^2}\right)\cosh\kappa+\frac{RC}{\kappa^2}\right] \quad (15)$$

Note that the corresponding boundary conditions are

$$w(0) = a, \quad w(1) = b \quad (16)$$

We assume that the solution of Eq. (10) can be expressed as a power series in q, i.e.,

$$u(y,q) = w_0+qw_1+q^2w_2+\cdots \quad (17)$$

where the w_i's are independent of q. Substituting Eq. (17) into Eqs. (12) and (16), and equating powers of q, gives rise to a set of problems that we will now specify and solve in the following subsections.

3.1 The Zeroth-Order Problem

The differential equation of the zeroth-order problem is

$$\frac{\partial^2 w_0}{\partial y^2} - \kappa^2 w_0 - \frac{\partial^2 u_0}{\partial y^2} + \kappa^2 u_0 = 0 \tag{18}$$

under the boundary conditions

$$w_0(0) = a, \quad w_0(1) = b \tag{19}$$

The solution of the zeroth-order problem is

$$w_0(y) = \alpha \cosh(\kappa y) + \beta \sinh(\kappa y) - \frac{RC}{\kappa^2} \tag{20}$$

3.2 The First-Order Problem

The differential equation for the first-order problem is

$$\frac{\partial^2 w_1}{\partial y^2} - \kappa^2 w_1 - RC_d \kappa w_0^2 = 0 \tag{21}$$

under the boundary conditions

$$w_1(0) = 0, \quad w_1(1) = 0 \tag{22}$$

The solution of the first-order boundary value problem is given by

$$\begin{aligned} w_1(y) = \frac{RC_d}{\kappa}\Bigg[& \left\{\frac{\alpha y}{2} + \varphi\right\}\sinh(\kappa y) \\ & + \left\{\frac{\beta y}{2} - \frac{RC}{\kappa^3}\right\}\cosh(\kappa y) + \frac{RC}{\kappa^3}\Bigg] \end{aligned} \tag{23}$$

where

$$\varphi = \frac{1}{\sinh\kappa}\left[\left(\frac{RC}{\kappa^3} - \frac{\beta}{2}\right)\cosh(\kappa) - \frac{\alpha}{2}\sinh\kappa - \frac{RC}{\kappa^3}\right] \tag{24}$$

Although it is possible to go up to the second-order problem and its associated solutions, the solution to the first-order problem is reasonable. Therefore, the homotopy perturbation solution of the problem up to the first order is

$$u(y) = \lim_{q\to 1} u(y,q) = w_0(y) + w_1(y) + \cdots \tag{25}$$

or equivalently

$$\begin{aligned} u(y) = & \left[\frac{RC_d}{\kappa}\left\{\frac{\alpha y}{2} + \varphi\right\} + \beta\right]\sinh(\kappa y) \\ & + \left\{\frac{RC_d}{\kappa}\left(\frac{\beta y}{2} - \frac{RC}{\kappa^3}\right) + \alpha\right\}\cosh(\kappa y) \\ & + \frac{RC}{\kappa^2}\left(\frac{RC_d}{\kappa^2} - 1\right) \end{aligned} \tag{26}$$

where recall that α, β, and φ as above are

$$\alpha = a + \frac{RC}{\kappa^2}$$

$$\beta = \frac{1}{\sinh\kappa}\left[b - \left(a + \frac{RC}{\kappa^2}\right)\cosh\kappa + \frac{RC}{\kappa^2}\right]$$

$$\varphi = \frac{1}{\sinh\kappa}\left[\left(\frac{RC}{\kappa^3} - \frac{\beta}{2}\right)\cosh(\kappa) - \frac{\alpha}{2}\sinh\kappa - \frac{RC}{\kappa^3}\right]$$

4. THE DARCY–LAPWOOD–BRINKMAN EQUATION

Mathematically, the particular form of DFB Eq. (10) is a more general equation in the sense that it includes the microscopic inertial terms, and the DLB equation is a particular case of DFB Eq. (10). This particular case occurs when the drag coefficient $C_d = 0$, reducing Eq. (10) to

$$u_{yy} = RC + \frac{u}{k} \tag{27}$$

which is the DLB equation for the problem under consideration. Consequently, a part of the verification of the solution [Eq. (26)] can be achieved by substituting $C_d = 0$ into Eq. (26), giving us the following general solution for Eq. (27):

$$u(y) = \beta \sinh(\kappa y) + \alpha \cosh(\kappa y) - \frac{RC}{\kappa^2} \tag{28}$$

where we recall that α and β as above are

$$\alpha = a + \frac{RC}{\kappa^2}$$

$$\beta = \frac{1}{\sinh\kappa}\left[b - \left(a + \frac{RC}{\kappa^2}\right)\cosh\kappa + \frac{RC}{\kappa^2}\right]$$

We will complete the verification in the next section by specifying practical situations by defining a and b.

5. RESULTS AND DISCUSSION

The solutions of the two equations mentioned earlier are general, but for practical purposes we introduce three different entry flow profiles. As mentioned above, we will consider Poiseuille, Couette, and Poiseuille–Couette flows. In the next few subsections we consider each of these flow conditions for both Eqs. (10) and (27).

5.1 Poiseuille Entry Profile

In the first instance we consider the DFB equation. Assuming an entry profile of Poiseuille type, we set $a = b = 0$ and $C \neq 0$, giving us the solution

$$u(y) = \frac{RC}{\kappa^2}\left[\left\{\frac{RC_d}{2\kappa}(y-1)+E_1\right\}\sinh(\kappa y) + \left\{\frac{RC_d(1-\cosh\kappa)}{2\kappa\sinh\kappa}y - \frac{RC_d}{\kappa^2}+1\right\}\cosh(\kappa y) + \left(\frac{RC_d}{\kappa^2}-1\right)\right] \quad (29)$$

where E_1 is defined as

$$E_1 = \frac{1-\cosh\kappa}{\sinh\kappa}\left[1-\frac{RC_d}{\kappa}\left(\frac{\cosh\kappa}{2\sinh\kappa}+\frac{1}{\kappa}\right)\right]$$

Similarly, for DLB Eq. (27), for an entry profile of Poiseuille type, we substitute $a = b = 0$ and $C \neq 0$ into Eq. (28) and we get

$$u(y) = \frac{RC}{\kappa^2}\left[\cosh(\kappa y)+\frac{(1-\cosh\kappa)}{\sinh\kappa}\sinh(\kappa y)-1\right] \quad (30)$$

which can be re-written as

$$u(y) = -RCk + RCk\left[e^{y/\sqrt{k}} + \frac{e^{y/\sqrt{k}} - e^{-y/\sqrt{k}} - e^{(1+y)/\sqrt{k}} + e^{(1-y)/\sqrt{k}}}{e^{1/\sqrt{k}} - e^{-1/\sqrt{k}}}\right] \quad (31)$$

This, in fact, is the solution of the DLB equation for a Poiseuille entry profile, which also matches the solution given by Awartani and Hamdan (2005).

In Fig. 1 we see the velocity profiles for the DLB and DFB models for a Poiseuille entry profile. We clearly see that the inclusion of the microscopic inertia through the DFB model causes a slowing down of the flow, which is the same result obtained by Awartani and Hamdan (2005).

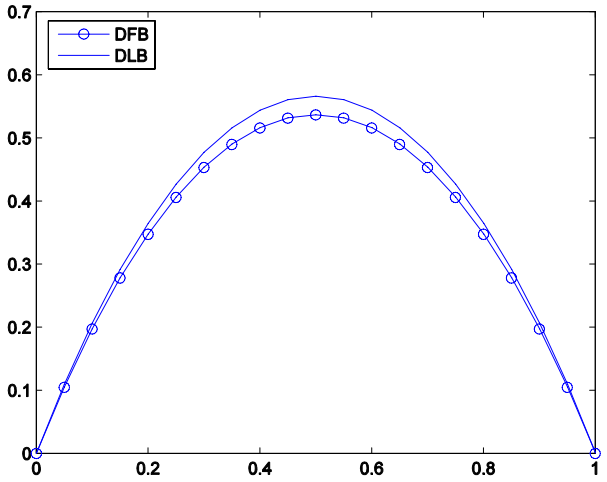

FIG. 1: This graph represents a Poiseuille-type entry profile. Variation of velocity u versus y for both the Darcy–Lapwood–Brinkman (DLB) and Darcy–Forchheimer–Brinkman (DFB) models. For computing these graphs we have set $C = -5$, $R = 1$, and $k = 1$. In addition, for the DFB model $C_d = 0.55$ and for the DLB model $C_d = 0$.

These graphs also offer a verification for the solutions obtained here. The advantage gained in the analytical solution is that we can see the expressions that are the contributing elements representing the microscopic inertia. One can clearly notice these as terms that have drag coefficient C_d multiplying them in Eq. (29).

5.2 Poiseuille–Couette Entry Profile

Once again, starting with the DFB equation, assuming an entry profile of Poiseuille–Couette type, we set $a = 0$, $b = 1$, and $C \neq 0$ giving us the solution

$$u(y) = \left[\frac{RC}{\kappa^2}\left\{\frac{RC_d}{2\kappa}(y-1)+E_1\right\}+\frac{1}{\sinh\kappa} \times \left(1-\frac{RC_d\cosh\kappa}{2\kappa\sinh\kappa}\right)\right]\sinh(\kappa y) + \left[\frac{RC}{\kappa^2} \times \left\{\frac{RC_d(1-\cosh\kappa)}{2\kappa\sinh\kappa}y - \frac{RC_d}{\kappa^2}+1\right\}+\frac{RC_d}{2\kappa\sinh\kappa}y\right] \times \cosh(\kappa y) + \frac{RC}{\kappa^2}\left(\frac{RC_d}{\kappa^2}-1\right) \quad (32)$$

As one would expect, the analytical solution obtained in the previous section of DFB Eq. (10) should reduce to

the solution of the DLB Eq. (27). If we substitute $a = 0$, $b = 1$, $a = 0$, $b = 1$, $C \neq 0$, and $C_d = 0$ into Eq. (26) we get

$$u(y) = \frac{\sinh(\kappa y)}{\sinh \kappa} + \frac{RC}{\kappa^2}\left[\cosh(\kappa y) + \frac{(1-\cosh \kappa)}{\sinh \kappa} \times \sinh(\kappa y) - 1\right] \tag{33}$$

which can be re-written as

$$u(y) = RCk\left[\frac{e^{y/\sqrt{k}} - e^{-y/\sqrt{k}}}{e^{1/\sqrt{k}} - e^{-1/\sqrt{k}}}\left(1 + \frac{1}{RCk} - e^{1/\sqrt{k}}\right) + e^{y/\sqrt{k}} - 1\right] \tag{34}$$

which matches the result obtained by Awartani and Hamdan (2005), as expected. It is also worth noting that the DLB equation is a linear differential equation and simple to solve, and that the solution, indeed, is correct. In Fig. 2 we present the graphs of the solutions for the two models. Once again, we notice the slower profile of the DFB model, due to the presence of the microscopic inertia. The graph closely matches the results obtained by Awartani and Hamdan (2005).

5.3 Couette Entry Profile

We begin again with the DFB equation and simply substitute $C = 0$ into Eq. (32), giving us

$$u(y) = \left[\frac{1}{\sinh \kappa}\left(1 - \frac{RC_d \cosh \kappa}{2\kappa \sinh \kappa}\right)\right]\sinh(\kappa y) + \left[\frac{RC_d}{2\kappa \sinh \kappa} y\right]\cosh(\kappa y) \tag{35}$$

We substitute $C_d = 0$ into Eq. (35), giving us

$$u(y) = \frac{\sinh(\kappa y)}{\sinh \kappa} = \frac{e^{y/\sqrt{k}} - e^{-y/\sqrt{k}}}{e^{1/\sqrt{k}} - e^{-1/\sqrt{k}}} \tag{36}$$

which is the expected solution if we solve DLB Eq. (27) with $C = 0$. This further verifies the solutions presented in the preceding sections.

In Fig. 3 we present the graphs of the solutions for the two models, this time for a Couette entry profile. Once again we notice the slower profile of the DFB model, due to the presence of the microscopic inertia. The graph closely matches the results obtained by Awartani and Hamdan (2005).

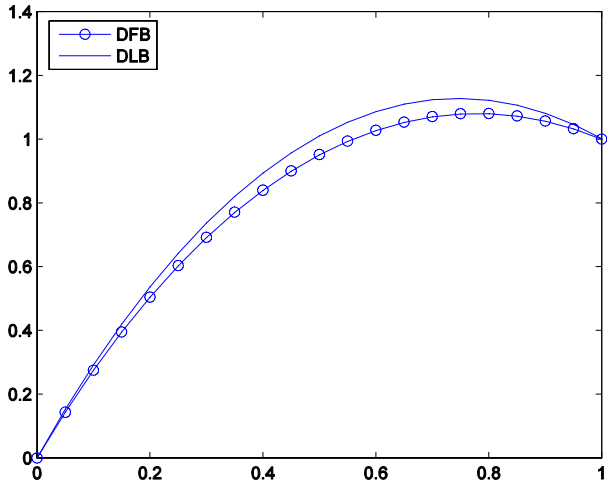

FIG. 2: This graph represents a Poiseuille–Couette-type entry profile. Variation of velocity u versus y for both the Darcy–Lapwood–Brinkman (DLB) and Darcy–Forchheimer–Brinkman (DFB) models. For computing these graphs we have set $C = 1$, $R = 1$, and $k = 1$. In addition, for the DFB model $C_d = 0.55$ and for the DLB model $C_d = 0$.

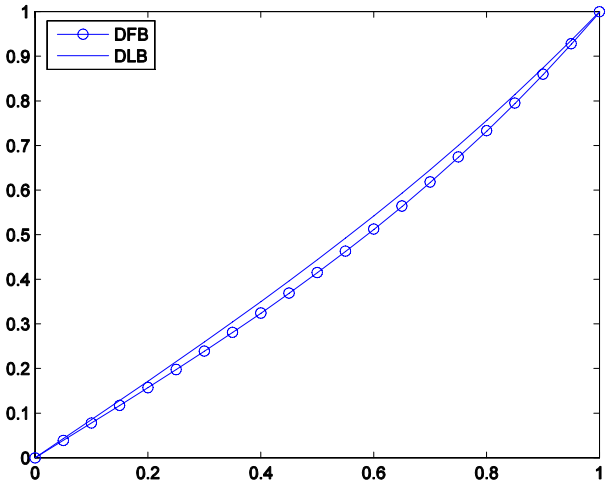

FIG. 3: This graph represents a Couette-type entry profile. Variation of velocity u versus y for both the Darcy–Lapwood–Brinkman (DLB) and Darcy–Forchheimer–Brinkman (DFB) models. For computing these graphs we have set $C = 1$, $R = 1$, and $k = 1$. In addition, for the DFB model $C_d = 0.55$ and for the DLB model $C_d = 0$.

6. CONCLUSIONS

The main objective of this study was to present an analytical solution of the particular form of the DFB model, representing the developed flow through a porous channel between parallel plates. The problem has been well documented by Awartani and Hamdan (2005); in fact, we follow the analysis of their work and use it as a bench mark for the analytical solution presented here. We have considered three types of entry profiles driving the flow, namely, Poiseuille, Couette, and Poiseuille–Couette type. In addition, we have considered the problem with generalized boundary conditions and presented the solution with respect to these boundary conditions. The solution simply requires the input of the appropriate parameters to produce solutions to different problems. We have demonstrated this through the subsections above in the section on Results and Analysis. Although we do not really present the solution to a new problem, we do present the analytical solution of the problem. This solution shows, for instance, not only the overall effect of the microptic inertia, but it additionally shows the term(s) (since more terms in the solution can be taken) that contribute to the dynamics of the problem. We also demonstrates the advantages of an analytical solution. As verification, we have shown the solution of the DLB model for the same problem; the model can be obtained from the DFB model by simply setting the drag coefficient to zero. As such, for the solution obtained by doing the same with our solution, we expect the correct solution of the DLB model, which is an easier linear solvable differential equation; and this, in fact, was shown and verified our solution. In addition, we have offered further verification of the solution by comparing it to the solution obtained by Awartani and Hamdan (2005), and all scenarios show a match.

REFERENCES

Awartani, M. M. and Hamdan, M. H., Fully developed flow through a porous channel bounded by flat plates, *Appl. Math. Comput.*, vol. **169**, pp. 749–757, 2005.

Biazar, J. and Ghazvini, H., Convergence of the homotopy perturbation method for partial differential equations, *Nonlinear Anal.: Real World Appl.*, vol. **10**, pp. 2633–2640, 2009.

Hamdan, M. H., Single-phase flow through porous channels, a review of flow models and channel entry conditions, *Appl. Math. Comput.*, vol. **62**, pp. 203–222, 1994.

He, J. H., Homotopy perturbation technique, *Comput. Methods Appl. Mech. Eng.*, vol. **178**, pp. 257–262, 1999.

He, J. H., Some asymptotic methods for strongly nonlinear equations, *Int. J. Mod. Phys. B*, vol. **20**, no. 10, pp. 1141–1199, 2006a.

He, J. H., New interpretation of homotopy perturbation method, *Int. J. Mod. Phys. B*, vol. **20**, no. 18, pp. 2561–2568, 2006b.

Kuznetsov, A. V., Analytical investigation of heat transfer in Couette flow through a porous medium utilizing the Brinkman–Forchheimer-extended Darcy model, *Acta Mech.*, vol. **129**, pp. 13–24, 1998.

Marafie, A. and Vafai, K., Analysis of Non-Darcian effects on temperature differentials in porous media, *Int. J. Heat Mass Transfer*, vol. **44**, pp. 4401–4411, 2001.

Nield, D. A., Junqueira, S.L.M., and Lage, J.L., Forced convection in a fluid-saturated porous-medium channel with isothermal or isoflux boundaries, *J. Fluid Mech.*, vol. **322**, pp. 201–214, 1996.

Pantokratoras, A., Fully developed forced convection of three fluids with variable thermophysical properties flowing through a porous medium channel heated asymmetrically with large temperature differences, *J. Porous Media*, vol. **10**, pp. 409–419, 2007a.

Pantokratoras, A., Fully developed Couette flow of three fluids with variable thermophysical properties flowing through a porous medium channel heated asymmetrically with large temperature differences, *ASME J. Heat Transfer*, vol. **129**, pp. 1742–1747, 2007b.

Siddiqui, A. M., Ahmed, M., and Ghori, Q. K., Couette and Poiseuille flow for non-Newtonian fluids, *Int. J. Nonlinear Sci. Numer. Simul.*, vol. **7**, no. 1, pp. 15–26, 2006a.

Siddiqui, A. M., Mahmood, R., and Ghori, Q. K., Thin film flow of a fourth grade fluid down a vertical cylinder by He's homotopy Perturbation method, *Phys. Lett. A*, vol. **352**, pp. 404–410, 2006b.

Siddiqui, A. M., Mahmood, R., and Ghori, Q. K., Homotopy perturbation method for thin film flow of a third grade fluid down an inclined plane, *Chaos, Solitons & Fractals*, vol. **35**, no. 1, pp. 140–147, 2008a.

Siddiqui, A. M., Irum, S., and Ansari, A. R., Unsteady squeezing flow of a viscous MHD fluid between parallel plates, a solution using the homotopy perturbation, *Math. Modell. Anal.*, vol. **13**, no. 4, pp. 565–576, 2008b.

JOURNAL OF POROUS MEDIA

VOLUME 13 CONTENTS

NUMBER 1

NUMBER 2

NUMBER 3

NUMBER 4

NUMBER 5

NUMBER 6

NUMBER 7

NUMBER 8

NUMBER 9

NUMBER 10

NUMBER 11

NUMBER 12

JOURNAL OF POROUS MEDIA

AUTHOR INDEX FOR VOLUME 13

Page Range of Issues

Issue 1: 1–96; Issue 2: 97–193; Issue 3: 195–294; Issue 4: 295–399
Issue 5: 395–495; Issue 6: 497–590; Issue 7: 591–669; Issue 8: 671–763
Issue 9: 765–854; Issue 10: 855–949; Issue 11: 951–1037; Issue 12: 1039–1125

JOURNAL OF POROUS MEDIA

SUBJECT INDEX FOR VOLUME 13

Page Range of Issues

Issue 1: 1–96; Issue 2: 97–193; Issue 3: 195–294; Issue 4: 295–399
Issue 5: 395–495; Issue 6: 497–590; Issue 7: 591–669; Issue 8: 671–763
Issue 9: 765–854; Issue 10: 855–949; Issue 11: 951–1037; Issue 12: 1039–1125

Reviewers for Volume 13

The Editorial Board of the *Journal of Porous Media* would like to thank the following reviewers for their reviews and their help in establishing a high-quality review process. We add particular thanks to MANY reviewers who did multiple reviews.

Abbasbandy, S.
Abbassi, A.
Abd Elazem, N.Y.
Abd-El Aziz M. Salem
Abdel-Rehim, Z.S.
Abdou, M.M.M.
Ahmad, I.
Alazmi, B.
Al-Bazali, T.
Albouchi, F.
Ali, N.
Al-Khlaifat, A.
Anderson, D.M.
Arabnia, H.R.
Arce, P.
Ari-Gur, P.
Ayvaz, M.T.
Bahloul, A.
Balhoff, M.
Bansod, V.J.
Basagaoglu, H.
Belghith, A.
Bellini da Cunha Neto, J.A.
Ben Nasrallah, S.
Benhamidouche, N.
Bennacer, R.
Bera, P.
Bhattacharyya, S.
Bijeljic, B.
Bishnoi, J.
Biswas, A.
Biswas, G.
Blums, E.
Bokhari, A.H.
Bujurke, N.M.
Bull, J.L.
Buschek, T.
Bokhari, A.H.
Breitkopf, C.
Bujurke, N.M.
Cerbino, R.
Chamkha, A.J.
Chandra, P.
Chen, C.I.
Cherif, B.
Cihat Baytas, A.
Civan, F.
Correia de Sequeira, C.A.
Cortis, A.
Costa, V.A.F.
Coutelieris, F.A.
Damseh, R.
Das, S.K.
Datti, P.S.
De Cesaro Olivesky, R.
Deka, R.K.
Delgado, J.M.P.Q.
Deng, S.
Deping, H.
DiCarlo, D.
Domairry, G.
du Plessis, P.
Dumitru, V.
Duursma, G.
Duwairi, H.
Echekki, T.
El-Amin, M.F.
Eldabe, N.T.
Elgazery, N.S.
El-Kabeir, S.M.M.
El-Sayed, M.F.
Esmaeilzadeh, F.
Ezzat, M.A.
Fetecau, C.
Frizon, F.
Furberg, R.
Ganji, D.D.
Ghesmat, K.
Gollahalli, S.R.
Guba, P.
Haddad, O.M.
Haji-Sheikh, A.
Hayat, T.
Hilfer, R.
Hossain, A.
Huang, H.
Huang, P.-C.
Hussain, M.
Jaroniec, M.
Jha, B.K.
Kara, A.H.
Karahan, H.
Katiyar, V.K.
Kaviany, M.
Keramaris, E.
Khalique, C.M.
Khan, M.
Kimura, S.
Laloui, L.
Li, C.W.
Li, S.
Liao, S.
Liu, C.
Liu, H.-H.
Liu, W.
Magyari, E.
Mahmud, S.
Mahomed, F.M.
Malashetty, M.S.
Marcondes, F.
Marcoux, M.
Marin, M.
Martins, A.
Mazumdar, M.K.
Mehta, M.N.
Miguel, A.F.
Mishra, M.
Misirlioglu, A.
Moatimid, G.M.
Moitsheki, R.
Molenkamp, F.
Momoniat, E.
Morland, L.W.
Morsi, Y.S.
Narasimhan, A.
Nield, D.A.
Nobari, M.R.H.
Pantokratoras, A.
Partap, G.
Philippi, P.C.
Plecas, I
Porter, M.
Postelnicu, A.
Qi, H.-T.
Qu, W.
Rainer, H.
Ramos, N.M.M.
Rashad, A.M.
Rathish Kumar, B.V.
Rees, D.A.S.
Saez, A.E.